

UCLA

UCLA Electronic Theses and Dissertations

Title

Solution-Processed Low-Cost Approaches for High-Efficiency Organic Light Emitting Diodes Substrates

Permalink

<https://escholarship.org/uc/item/2qz790bm>

Author

Tong, Kwing Shing Michael

Publication Date

2018

Peer reviewed|Thesis/dissertation

UNIVERSITY OF CALIFORNIA

Los Angeles

Solution-Processed Low-Cost Approaches for High-Efficiency

Organic Light Emitting Diodes Substrates

A dissertation submitted in partial satisfaction of the

requirements for the degree of

Doctor of Philosophy in Materials Science and Engineering

by

Kwing Shing Michael Tong

2018

© Copyright by

Kwing Shing Michael Tong

2018

ABSTRACT OF THE DISSERTATION

Solution-Processed Low-Cost Approach for High-Efficiency

Organic Light Emitting Diodes Substrates

by

Kwing Shing Michael Tong

Doctor of Philosophy in Materials Science and Engineering

University of California, Los Angeles, 2018

Professor Qibing Pei, Chair

An affordable and high-performing solution for organic light emitting diode (OLED) substrates has been sought after in the global lighting market with demand in mechanical flexibility, color tunability, high efficiency, and high throughput, low-cost manufacturing. One potential solution that has gained an increasing amount of attention is through the development and implementation of silver nanowire electrodes. This work makes several key contributions towards enabling the use of silver nanowires (AgNWs) through the development of solution-processed low-cost approaches to fabricate flexible substrates using polymers and nanoparticles to obtain improvements in optical outcoupling enhancement and color quality. First, a novel method for patterning silver nanowires was developed to screen-print features with up to 50 μm resolution at $\sim 40,000 \text{ S cm}^{-1}$ conductivity. The printed patterns were used to fabricate OLED substrates with a sheet resistance of 5 ohm sq^{-1} at 89% transmittance, and the fabricated OLEDs showed a 1.6X efficiency enhancement in comparison to OLEDs fabricated on the ITO/glass reference electrodes. Second, an integrated nanocomposite substrate of AgNW anode, a high

index polymer layer for microcavity tuning, and a light scattering layer consist of barium strontium titanate nanoparticles and methacrylate polymer matrix for light outcoupling was developed through optimization of the layer thicknesses and particle concentrations to obtain WOLED devices that yielded a power efficacy (PE) of 107 lm W^{-1} and an external quantum efficiency (EQE) of 49% at $1,000 \text{ cd m}^{-2}$, which corresponds to an enhancement factor of ~ 2.76 in comparison to the control devices fabricated on ITO/glass substrates. Lastly, color rendering OLED substrates were fabricated with a color conversion layer consists of FBtF dye to improve the CRI of the WOLED to 83 while maintaining device performance of 85.83 cd A^{-1} current efficiency, 82.96 lm W^{-1} power efficacy, and 48.6% EQE. The process development of the substrate architectures in this study has demonstrated the advantageous of AgNW-polymer nanocomposite electrodes in efficiency enhancement and mechanical compliance through low-cost solution-based fabrication methods and have paved the way for potential adaptation in large-scale manufacturing of this technology for commercial lighting applications.

The dissertation of Kwing Shing Michael Tong is approved.

Ximin He

Dwight Christopher Streit

Benjamin Joel Schwartz

Qibing Pei, Committee Chair

University of California, Los Angeles

2018

Dedicated to my beloved family

for their love and support

Table of Contents

List of Figures.....	x
List of Tables.....	xix
Acknowledgements.....	xx
Vita.....	xxii
1. Introduction.....	1
1.1 Fabrication of AgNW Electrodes.....	5
1.1.1 Basic AgNW Electrodes.....	5
1.1.2 Flexible AgNW Electrodes.....	7
1.1.3 Stretchable AgNW Electrodes.....	8
1.2 Lighting Applications Based on AgNW Electrodes.....	12
1.2.1 Working Principles of an OLED and the Advantages of AgNW Electrodes.....	13
1.2.2 Flexible Light Emitting Devices.....	16
1.2.3 Stretchable Light Emitting Devices.....	23

1.2.4	Integrated Systems for Lighting using AgNWs.....	26
1.3	Motivation and Research Scope of this Dissertation.....	30
2.	Water Based Silver Nanowire Screen-Printing Ink.....	34
2.1	Introduction.....	34
2.2	Experimental Section.....	37
2.2.1	Materials.....	37
2.2.2	Preparation of Screen-Printing AgNW Ink.....	38
2.2.3	Screen-Printing and Post Treatment.....	38
2.2.4	Fabrication of Stretchable Composite Conductors.....	39
2.2.5	Fabrication of Fully-Printed TFT Array.....	39
2.2.6	Fabrication of Screen-Printed Metal Grid.....	40
2.2.7	Characterization Methods.....	41
2.3	Results and Discussion.....	42
2.3.1	Rheological Behavior of the AgNW Screen-Printing Ink.....	42
2.3.2	Electrical Properties and Stretchability of the Screen-Printed AgNWs.....	52
2.3.3	Device Performance of the Fully Printed TFT Array.....	59
2.3.4	Device Performance of OLEDs on a Highly Transparent Flexible Substrate.....	63

2.4 Conclusion.....	69
3. Efficient Light Extraction of OLEDs on Fully Solution-Processed Flexible Substrate... 71	
3.1 Introduction.....	71
3.2 Experimental Section.....	73
3.2.1 Materials.....	73
3.2.2 Nanocomposite Substrate Fabrication.....	74
3.2.3 Fabrication of WOLED.....	74
3.2.4 Characterization Methods.....	75
3.3 Results and Discussion.....	75
3.3.1 Mechanism of Light Extraction.....	75
3.3.2 Fabrication Process and Characterization of Substrate.....	77
3.3.3 WOLED Performance with Different Light Scattering Particle Concentration... 79	
3.3.4 Microcavity Effect of the High Refractive Index Polymer Layer.....	84
3.4 Conclusion.....	89
4 Color Rendering of WOLED through Dopants within the OLED Substrate..... 90	
4.1 Introduction.....	90
4.2 Experimental Section.....	95

4.2.1	Materials.....	95
4.2.2	Synthesis of FBtF.....	95
4.2.3	Nanocomposite Substrate Fabrication.....	97
4.2.4	Fabrication of WOLED.....	98
4.2.4	Characterization Methods.....	99
4.3	Results and Discussion.....	99
4.3.1	Mechanism of the Color Conversion Layer.....	99
4.3.2	Fabrication Process and Characterization of Substrate.....	101
4.3.3	Device Performance of WOLED with Color Conversion Layer.....	103
4.4	Conclusion.....	105
5	Summary and Outlook.....	107
5.1	Concluding Remarks.....	107
5.2	Future Outlook.....	110
	Reference.....	113

List of Figures

- Figure 1.1.** a) Transmittance as a function of wavelength for AgNW-acrylate electrodes at various sheet resistances. b) AFM topographical image of a freestanding AgNW-PUA composite electrode with a sheet resistance of 10 ohm/sq..... 6
- Figure 1.2.** a) Photograph of a GO-AgNW/PET composite bent to 4 mm radius. b) Relative resistance change of the GO-AgNW/PET composite during repeated bending to 4 mm radius. c) Photograph of a GO-AgNW electrode printed on paper substrate being sharply folded. d) Relative resistance change of GO-AgNW electrode printed on paper substrate during repeated folding..... 8
- Figure 1.3.** a) Change in sheet resistance of AgNW/AA-TBA composite with increasing strain. b) Change in sheet resistance of AgNW/AA-TBA composite during 10 cycles of stretching between 0 and 50% strain at a constant rate of 0.005 Hz..... 10
- Figure 1.4.** a) Change in sheet resistance of AgNW/PU composite with increasing strain. b) Change in sheet resistance of AgNW/AA-TBA composite during a cycle of stretching between 0 and 60% strain at different stretching rates..... 11

Figure 1.5. a) SEM image of SO-soldered AgNW electrode with red arrow indicating areas with fused junctions. b) Change in resistance of GO-AgNW/PUA composite with increasing strain when stretched at 1 mm/s..... 12

Figure 1.6. Cross sectional schematic of WPLEDs on ITO/glass (left) and AgNW/polymer (right), illustrating the refractive index mismatch between layers of the WPLED stack and the optical mechanism leading to waveguide, substrate, and air modes..... 15

Figure 1.7. Performance characteristics of PLECs on SWCNT/PET electrodes before and after bending to 2.5 mm radius. a) Current-Voltage-Luminance (J-V-L) characteristic. b) Current Efficiency-Luminance (CE-L) characteristics. 17

Figure 1.8. Performance characteristics of PLECs on ITO/glass, AgNW/PUA, and SWCNT-AgNW/PUA composites. a) Current-Voltage (J-V) characteristic. b) Luminance-Voltage- (L-V) characteristic. c) Current Efficiency-Luminance (CE-L) characteristics. d) Current Efficiency-Luminance (CE-L) characteristics before and after 10 cycles of bending to a 5.0 mm radius. 18

Figure 1.9. Performance characteristics of PLEDs on ITO/glass and AgNW/shape-memory acrylate composites. a) Current Efficiency-Current Density (CE-J) characteristics. b) Current Efficiency-Current (CE-J) characteristics before and after 10 cycles of concave and convex bending to a 2.5 mm radius..... 19

Figure 1.10. Performance characteristics of WPLEDs on ITO/glass and AgNW/polymer composites. a) Current-Voltage-Luminance (J-V-L) characteristic. b) Current

Efficiency- Luminance (CE-L) characteristic. Inset shows Power Efficiency- Luminance (PE-L) characteristic.....20

Figure 1.11. Performance characteristics of WPLEDs various substrates. a) Schematic of an OLED with nanocomposite substrate and the optical mechanisms leading to outcoupling of the substrate and waveguide modes. b) Current Efficiency-Luminance (CE-L) characteristic. c) Power Efficiency-Luminance (PE-L) characteristic..... 21

Figure 1.12. Mechanical deformation of PLECs on AgNW/PUA composites. a) PLECs stretched from 0 to 120% strains under a 14 V bias. b) PLECs wrapped around the edge of 400 μm-thick cardboard under a 12 V bias..... 24

Figure 1.13. Mechanical deformation of PLECs on GO-AgNW/PUA composites. a) PLECs stretched from 0 to 130% strains under a 13 V bias. b-d) Device characteristics after stretching cycles between 0 and 40% strains. 25

Figure 1.14. Demonstration of the healing capability of the touch screen. a) Before cutting. b) After cutting along the red dash line. c) After healing at 80 °C for 30 s with a hair dryer.. 27

Figure 1.15. Output ($I_{\text{OLED}}-V_{\text{DD}}$) characteristics of the OLED controlled by a stretchable SWCNT-AgNW TFT. The TFT is stretched along channel length direction by (a) 0%, (b) 20% and (c) 30% strains, with varying V_{G} from 0 to -5.0 V in 1V increments. Transfer ($I_{\text{OLED}}-V_{\text{G}}$) characteristics at V_{DD} of - 4.0V under 0% (d), 20% (e) and 30% (f) strains.....28

Figure 1.16. Luminance of an OLED driven by a stretchable TFT under various V_{G} at strains of 0, 20, and 30% when V_{DD} is -4.0 V..... 29

Figure 2.1. a) Molecular structures of (hydroxypropyl)methyl cellulose and Zonyl FC-300, and photograph of the as-prepared AgNW Ink-M. b) Viscosity as a function of shear rate for the AgNW inks. c) Rheological behavior of the inks during screen printing. d-e) Oscillatory rheological test for AgNW Ink-M: Variation of G' and G'' with shear stress, and G''/G' ratio as a function of shear stress.....43

Figure 2.2. Various AgNW lines screen printed from AgNW Ink-H. Pores are clearly seen in the printed lines. 44

Figure 2.3. Top-view SEM images of screen-printed AgNW patterns..... 47

Figure 2.4. a) Cross-sectional illustration of screen printing process. b) Optical image of screen printed AgNW patterns on flexible PET substrate. c) SEM image of the edge of the screen-printed AgNW line after post-treatment. d) SEM image showing the dense AgNW network structure in the screen-printed AgNW line.....48

Figure 2.5. a) Optical images and optical microscopic images of AgNW lines printed on PET substrates with line widths of 50 μm , 100 μm , 150 μm , 200 μm , and 250 μm . b) Optical microscopic image of AgNW patterns with spacing of 50 μm , 80 μm , 100 μm , and 120 μm . c) Thickness of screen printed AgNW lines as a function of line width. d) Aspect ratio (thickness/width) of the screen-printed AgNW lines with various line widths. All the patterns are printed with AgNW Ink-M at room temperature.....51

Figure 2.6. Cross-sectional SEM images of the screen-printed AgNW patterns with different widths..... 52

Figure 2.7. a) Optical microscopic image of screen-printed AgNW pattern to measure electrical properties. b) Measured resistance at various lengths and widths. c) Calculated sheet resistance. d) Calculated conductivity. At least 5 samples were tested for each line width..... 55

Figure 2.8. AFM image of the conductive surface of AgNW/PUA composite electrodes..... 58

Figure 2.9. (a) Conductivity change of screen-printed AgNW/PUA composite as a function of tensile strain. Inset image shows a printed AgNW pattern. Normalized transient resistance of screen-printed AgNW/PUA composite conductors with line widths of (b) 50 μm , (c) 100 μm , (d) 150 μm , (e) 200 μm , and (f) 250 μm during 1,000 cycles of tensile stretching between 0 and 30% strains. All line lengths are 5 mm, strain rate is 1 mm/s, and stretching direction is along the length direction..... 58

Figure 2.10. a) Optical microscopic image of screen-printed AgNW source/drain electrodes with channel length of 50 μm and channel width of 1,000 μm . b) Schematic illustration of the configuration of a fully printed TFT based on screen-printed AgNW source/drain electrodes. c) Picture of a fully-printed stretchable 10×6 TFT array. d) Picture of a fully-printed stretchable 10×6 TFT array contorted around a finger..... 60

Figure 2.11. Schematic illustration of the fabrication process of the fully-printed and stretchable/wearable TFT array..... 60

Figure 2.12. a) Output (I_D - V_D) characteristics of a typical TFT with V_G from 0 to -5V in 1.0 V step. b) Transfer(I_D - V_G) characteristics of the same device with V_D from -1.0 to -3.0 in 1.0 V step. Inset, I_D - V_G curve at V_D -2.0V on a logarithmic scale. c) Histograms of TFTs

in the 10×6 array showing the statistical distribution of mobility. d) Mobility change of one TFT in the fully printed array during 1,000 repeated cycles of wearing on and peeling off a glass vial with radius of 5 mm.....	62
Figure 2.13. a) Optical image of screen-printed AgNW pattern to measure electrical properties with different line width. b) Measured resistance at various lengths and widths. c) Calculated sheet resistance. d) Calculated conductivity. At least 5 samples were tested for each line width.....	64
Figure 2.14. Top-view SEM images of screen-printed AgNWs.....	65
Figure 2.15. AFM image of the conductive surface of AgNW/SR540+SR499 composite electrodes: a) 160 ohm sq^{-1} AgNW area and b) screen printed AgNW area.....	66
Figure 2.16. a) Photographs of device fabricated on a composite substrate operating at 4 V. Comparison of performance characteristics of WOLED devices with ITO and nanocomposite anodes: b) Current-Voltage-Luminance (J-V-L) characteristics, c) Power efficacy-Luminance-Current Efficiency (PE-L-CE) characteristics, and d) EQE vs Luminance.....	68
Figure 3.1. a) Schematic diagram of an OLED device with nanocomposite substrate and the optical mechanism leading to out-coupling of the substrate and waveguide modes. b) Fabrication process for a freestanding nanocomposite substrate containing silver nanowires embedded in the HIP layer and BST nanoparticles embedded in the light scattering layer. The inset shows an optical image of the nanocomposite substrate. (Diagrams are not to scale).....	77
Figure 3.2. AFM image of the conductive surface of the nanocomposite substrate.....	78

Figure 3.3. a) Schematic energy-level diagram of the two color-complementary hybrid WOLED device. b) Molecular structures of the relevant materials used in the fabrication of the WOLED..... 80

Figure 3.4. Normalized electroluminescence spectra of WOLED with ITO and nanocomposite anodes.....80

Figure 3.5. Shimadzu integrating sphere setup for measuring a) incident light (T1), b) total light transmitted by specimen (T2), c) light scattered by instrument (T3), and d) light scattered by instrument and specimen (T4).....81

Figure 3.6. a) Measured total transmittances (inset is a photograph of the corresponding light scattering layers), b) measured diffuse transmittances, and c) calculated haze of the light scattering layer as functions of BST concentration. d) A correlation between device power efficacy versus BST concentration showing an optimum between total transmittance and haze..... 83

Figure 3.7. a) Measured thickness of the PAI layer as a function of PAI concentration in NMP solutions. The inset shows the molecular structure of PAI. b) Comparison of calculated and experimental values of power efficacy versus PAI thickness showing outcoupling enhancement at PAI thickness correlating to microcavity tuning. Enhancement ratios are based on theoretical results obtained from the Setfos simulation software..... 85

Figure 3.8. Comparison of performance characteristics of WOLED devices with ITO and nanocomposite anodes. a) Current-Voltage-Luminance (J-V-L) characteristics. The inset shows a device fabricated on a nanocomposite substrate operating at 4 V. b) Power

efficacy-Luminance-Current Efficiency (PE-L-CE) characteristics. c) Angular dependence of electroluminescence intensity. d) EQE vs Luminance. (ITO/glass and nanocomposite substrate represents WOLEDs with the device structure of substrate / anode / PEDOT / TAPC / PO-01 / NPB / BePP₂ / CsF / Aluminum)..... 88

Figure 4.1. CIE 1931 Chromaticity Diagram. The outer curved boundary is the spectral (monochromatic) locus with wavelengths shown in nanometers. The solid curve through the middle is the black body locus, with the dots on in representing the black body temperatures shown in the inset box..... 91

Figure 4.2. Power efficiency and CRI performances of the WOLED in this study, compared with values from previously reported publications..... 93

Figure 4.3. a) Schematic diagram illustrating the WOLED device structure with the color conversion layer. b) Schematic energy-level diagram of the three color-complementary hybrid WOLED device..... 100

Figure 4.4. a) Molecular structures of FBtF. b) Photoluminescence spectrum of FBtF in isopropanol..... 100

Figure 4.5. The spectral power distribution of an incandescent bulb (CRI 100) and three-color FI./Ph. hybrid WOLED fabricated on ITO/glass, and photoluminescence spectra of the absorption and emission of FBtF..... 101

Figure 4.6. The fabrication process for a freestanding nanocomposite substrate containing silver nanowires embedded in the BST nanoparticles light scattering layer coated atop the FBtF color conversion layer..... 102

Figure 4.7. a) The spectral power distribution of an incandescent bulb (CRI 100), three color FI./Ph. hybrid WOLED fabricated on ITO/glass, AgNW + FBtF 1 and AgNW +

FBtF 2 nanocomposite substrates. b) WOLED fabricated on AgNW + FBtF 1 operating at 4V. (c) WOLED fabricated on AgNW + FBtF 2 operating at 4V..... 103

Figure 4.8. a) Comparison of performance characteristics of WOLED devices with ITO and nanocomposite anodes. a) Current-Voltage-Luminance (J-V-L) characteristics. b) Power efficacy-Luminance-Current Efficiency (PE-L-CE) characteristics. c) EQE vs Luminance. (ITO/glass and nanocomposite substrate represents WOLEDs with the device structure of substrate / anode / PEDOT / TAPC / Ir(piq)₃ / NPB / PO-01 / NPB / BePP₂ / CsF / Aluminum)..... 104

List of Tables

Table 2.1. Viscosity of various AgNW inks at different shear rates corresponding to different printing process steps.....	44
Table 2.2. Comparison of electrical conductivity of the present work with various previous research and commercial product concerning screen printed inks.....	54
Table 2.3. Comparison of electrical conductivity and stretchability of the present work with various previous research concerning intrinsically stretchable conductors.....	57

Acknowledgements

First and foremost, I would like to express the deepest appreciation to my advisor, Professor Qibing Pei, for his mentorship, encouragement, and support. Without his extensive personal and professional guidance, this dissertation would not have been possible.

I would also like to graciously thank Professor Ximin He, Professor Dwight Streit, and Professor Benjamin Schwartz for serving on my committee, providing guidance and suggestions that are vital for the completion of this dissertation.

I am grateful to all current and past members of the Soft Materials Laboratory Research Group whom I have had the pleasure to work with during this and other related projects. I am especially indebted to Dr. Dustin Chen, Dr. Xiaofeng Liu, Dr. Fangchao Zhao, Dr. Jiang Liu, and Dr. Jiajie Liang for the mentorship, discussions, and collaborations during our memorable time working together.

Furthermore, I would like to thank Dr. Ignacio Martini from UCLA Molecular Instrumentation Center, Dr. Sergey Prikhodko from the Materials Science department, and Dr. Adam Steig from CNSI for help and training on various testing instruments used through the course of my research.

Last but not least, nobody has been more important to me in the pursuit of this degree than the members of my family. I would like to thank my mother, whose unfaltering love are with me always. I would like to also thank my aunts and uncles who have provided me with the help and support over the years. Most importantly, I thank my loving wife, Yenting, who has provided me with a safe haven called home, where I can fall back comfortably in at the end of each day.

Thank you from the bottom of my heart to everyone who have been a part of my journey through my Ph.D. years. Thank you!

Vita

2009 B.S. Biomedical Engineering, University of California, Irvine, Irvine, CA

2010-2012 Associate Scientist, Medtronic, Inc., Northridge, CA

2015 M.S. Materials Science and Engineering, University of California, Los Angeles,
Los Angeles, CA

2017 Intern, Advanced Display Manufacturing, Apple, Inc., Cupertino, CA

Publications

First Author / Co-First Author

[1] **K. Tong** et al., Efficient Light Extraction of Organic Light Emitting Diodes on a Fully Solution-Processed Flexible Substrate, *Advanced Optical Materials*, Vol. 5, Issue 18, 1700307, DOI: 10.1002/adom.201700307 (2017).

[2] J. Liang, J. Oliva, **K. Tong**, et al., Multi-colored Light-emitting Electrochemical Cells Based on Thermally Activated Delayed Fluorescence Host, *Scientific Reports*, Vol. 7, 1524, DOI: 10.1038/s41598-017-01812- 2 (2017).

[3] **K. Tong**, J. Liang, & Q. Pei., Intrinsically-Stretchable, Transparent Thin Film Transistors, ECS Transactions, Vol. 75, Issue 10, 205-212, DOI:10.1149/07510.0205ecst (2016).

[4] J. Liang, **K. Tong**, & Q. Pei, A Water-Based Silver-Nanowire Screen-Print Ink for the Fabrication of Stretchable Conductors and Wearable Thin-Film Transistors, Advanced Materials, Vol. 28, Issue 28, 5986-5996, DOI:10.1002/adma.201600772 (2016).

Other Publications

[5] R. Ma, Z. Zhang, **K. Tong**, D. Huber, R. Kornbluh, Y.S. Ju, & Q. Pei, Highly Efficient Electrocaloric Cooling with Electrostatic Actuation, Science, Vol. 357, Issue 6356, 1130-1134, DOI: 10.1126/science.aan5980 (2017).

[6] J. Liang, **K. Tong**, H. Sun, & Q. Pei, Intrinsically Stretchable Field-effect Transistors, MRS Bulletin, Vol. 42, Issue 2, 131-137, DOI:10.1557/mrs.2016.326 (2017).

[7] D. Chen, F. Zhao, **K. Tong**, et al., Mitigation of Electrical Failure of Silver Nanowires under Current Flow and the Application for Long Lifetime Organic Light-Emitting Diodes, Advanced Electronic Materials, Vol. 2, Issue 8, DOI:10.1002/aelm.201600167 (2016).

[8] D. Chen, J. Liang, C. Liu G. Saldanha, F. Zhao, **K. Tong**, J. Liu, & Q. Pei, Thermally Stable Silver Nanowire-Polyimide Transparent Electrode Based on Atomic Layer Deposition of Zinc Oxide on Silver Nanowires, Advanced Functional Materials, Vol. 25, Issue 48, 7512-7520, DOI:10.1002/adfm.201503236 (2015).

[9] J. Liang, L. Li, **K. Tong**, et al. Silver Nanowire Percolation Network Soldered with Graphene Oxide at Room Temperature and its Application for Fully Stretchable Polymer Light-emitting Diodes, ACS Nano, Vol. 8, Issue 2, 1590-1600, DOI:10.1021/nn405887k (2014).

Chapter 1

Introduction

The discovery of the modern day organic light emitting diodes (OLEDs) dates back to 1987 at Eastman Kodak when Ching W. Tang and Steven Van Slyke first reported using a device with separated hole transporting and electron transporting layers to control recombination and light emission in the middle of the organic layer. This resulted in a reduction of operating voltage and an improvement in efficiency and achieved unprecedented performance with luminance exceeding 1000 cd m^{-2} below 10 V with a quantum efficiency of 1% photon/electron, which led to an era of OLED research and device development.^[1] Over the years, significant effort in developing materials with higher electrical and thermal stabilities, transport properties, color quality, and luminescence quantum yields, in conjunction with enhanced properties in mechanical deformability, low-power consumption, and low temperature fabrication, have propelled OLED technology to the forefront of the flat panel display and replacement lighting markets. In recent years, OLED displays have penetrated the consumer electronics market, with

its adaptation in high-end televisions, mobile phones, and smartwatches. OLEDs for lighting applications are still in their early developmental stages, but the range of potential advantages such as efficiency, mechanical compliance, adaptable form factors, and color tunability have many in the field regarding it as a potential candidate to rival its inorganic counterpart, LEDs, in the foreseeable future.

The rapid development of next-generation wearable electronics in medicine, robotics, and consumer electronics and flexible OLED light panels for high-end markets, has garnered widespread research interest in the development of high performing flexible and/or stretchable transparent conductive electrodes (TCEs). Besides the two primary parameters of TCEs in transparency and conductivity, mechanical compliance is becoming an essential criterion in next-generation TCEs. Mechanical compliance, the material's ability to retain its properties under various applied loadings and strains, allows for two major engineering advantages. In processing, the flexible TCEs allows for the realization of high throughput roll-to-roll processing and adaptability of final devices in complex form factors, such as around architectural pillars and automobile dashboards. Alternatively, the ability to withstand cyclic mechanical deformation allows for appealing design options such as flexible displays and foldable displays on wristbands or handheld devices.

Several materials, including but not limited to conducting polymers, carbon nanotubes, and graphene, are being widely studied for their applicability in next-generation TCEs. Recent studies in conducting polymers, such as PEDOT with conductivity-enhancing dopants, have significantly enhanced the conductivity and stretchability of this class of material, achieving up to 4100 S cm^{-1} under 100% strain.^[2] Although suitable for some optoelectronic applications, its figure of merit at approximately 55 with 10 ohm sq^{-1} sheet resistance at 75% transmittance limits

its competitiveness against the traditional standard set by indium tin oxide (ITO) anode with 10 ohm sq⁻¹ sheet resistance at > 85% transmittance. Carbon nanotubes have also garnered significant interest due to excellent stability and mechanical behavior, but its low conductivity prohibits its sole use as the conductor in most applications. Graphene has excellent stability, mechanical behavior, and extremely high conductivity when doped; however, the difficulty in producing a large volume of high-quality graphene sheets at a competitive cost deters this material from practicality.

As mentioned above, the two primary parameters in the selection of TCEs are high conductivity and transparency, with metrics set and often compared to ITO/glass or ITO/PET electrodes.^[3] Although ITO has an excellent figure of merit, it is inherently brittle, and strains of 1% or larger can cause irreversible crack formation, rendering its suitability for next-generation TCEs that desires a high level of flexibility and/or stretchability.^[4] The search for high performing flexible or stretchable transparent conductive electrodes (TCEs) has been highlighted as a critical barrier to surmount before the realization of high efficiency, high-performance wearable optoelectronic devices. As such, another key attribute, in addition to the aforementioned two parameters, is the ability to exhibit mechanical compliancy by retaining high transparency and conductivity upon mechanical deformation (under various applied loading and strains) of the flexible and stretchable TCEs.

In recent years, silver nanowire (AgNW) TCEs have garnered significant attention for applications in organic light emitting diodes, photovoltaic devices, transparent heaters, thin film transistors, thin film sensors, and electronic circuits and have been demonstrated to exhibit high conductivity, transparency, and mechanical compliance. AgNW TCEs are based on the concept of forming a percolation network of the most conductive 1D nanomaterial while allowing light to

propagate through the pores between the nanowires. Silver nanowires are highly suitable as the materials of choice for flexible anodes due to its ductility, and devices fabricated based on the AgNW TCEs have shown comparable, or in some instances enhanced, performance in comparison to devices fabricated on transparent conductive oxides, which further heightens its standing as a lucrative replacement in future TCEs.

To enhance the flexible and stretchable robustness and reduce the surface roughness of the electrode, AgNW TCEs were fabricated by embedding nanowires within a polymer matrix, with selection criteria in bonding between nanowires and polymer, glass transition temperature, modulus, and transparency. Engineering of the polymer matrix and substrate architectures can be tailored with unique properties for specific applications in optoelectronics using flexible, stretchable, shape memorable, and/or self-healable polymer substrates. In general, the aim of this area of research in our group focuses on the integration of AgNWs and polymer composites to develop TCEs as a viable replacement for ITO substrates, with particular interests in the integration of application-specific functionalities that are not obtainable with current technologies.

This chapter will first highlight the recent innovations in AgNW electrodes from our group and its usage in flexible and stretchable devices, starting with a brief introduction on the transfer process to fabricate polymer composites with embedded AgNWs along with descriptions of additional processing techniques that enhance the mechanical properties and stability of the nanowire composites. Next, the development and performance of devices and integrated systems using these electrodes for lighting applications will be discussed. Lastly, this chapter will conclude with the motivation and research scope behind the work of this dissertation.

1.1 Fabrication of AgNW Electrodes

1.1.1 Basic AgNW Electrodes

The basic AgNW electrodes are fabricated by coating a thin layer of AgNWs from a dispersion of AgNWs in isopropyl alcohol (IPA) and methanol through wet deposition techniques such as dip coating, spin coating, spray coating, or Meyer rod coating onto a smooth release substrate. A polymer precursor solution containing initiators is then overcoated atop the AgNW network, which infiltrates through the pores between the network until reaching the surface of the release substrate. One simple technique to coat the polymer precursor is through the use of the sandwich method, which consists of infiltrating the precursors through capillary action from the edge of two release substrates separated by tape spacers. After UV or thermal polymerization to crosslink the polymer, a freestanding film can be peeled off of the release substrates to obtain a transparent composite with a conductive surface made of the embedded AgNWs.

The overall transparency and conductivity of the composite can be controlled by the thickness of the AgNW layer deposited on and transferred from the release substrate. As shown in **Figure 1.1a**, there is a tradeoff between conductivity and transmittance with thickness. A sheet resistance of $\leq 15 \text{ ohm sq}^{-1}$ is generally preferred for high current devices such as OLEDs to minimize voltage drop across large format devices, and most electrode materials have less than ideal transmittance within this sheet resistance range. At a sheet resistance of $\sim 10 \text{ ohm sq}^{-1}$, the transparency of a AgNW composite is approximately 82%, which is comparable to commercial ITO on glass substrates.^[5,6] Comparatively, the transparencies of TCEs with conductivity-enhanced PEDOT electrodes is a mere 75% at similar sheet resistance, and the TCEs with CNTs would be nearly opaque.^[2]

Furthermore, the transfer process, which embeds the AgNWs within the polymer matrix, results in a conductive surface with a low surface roughness. A release glass substrate with $R_a \leq 0.5 \text{ nm}$ is typically used to provide a smooth interface to form the composite surface. This allows the devices that are fabricated on top of the electrodes to be more efficient by minimizing leakage current and electrical shorts. **Figure 1.1b** shows an atomic force microscopy (AFM) image of a composite substrate with an embedded AgNW electrode in a polyurethane acrylate (PUA) matrix with a sheet resistance of 10 ohm sq^{-1} at 82% transmittance. The average surface roughness (R_a) of the embedded AgNW electrodes are typically $< 2 \text{ nm}$ and could be further decreased when transferred with carbon nanotubes.

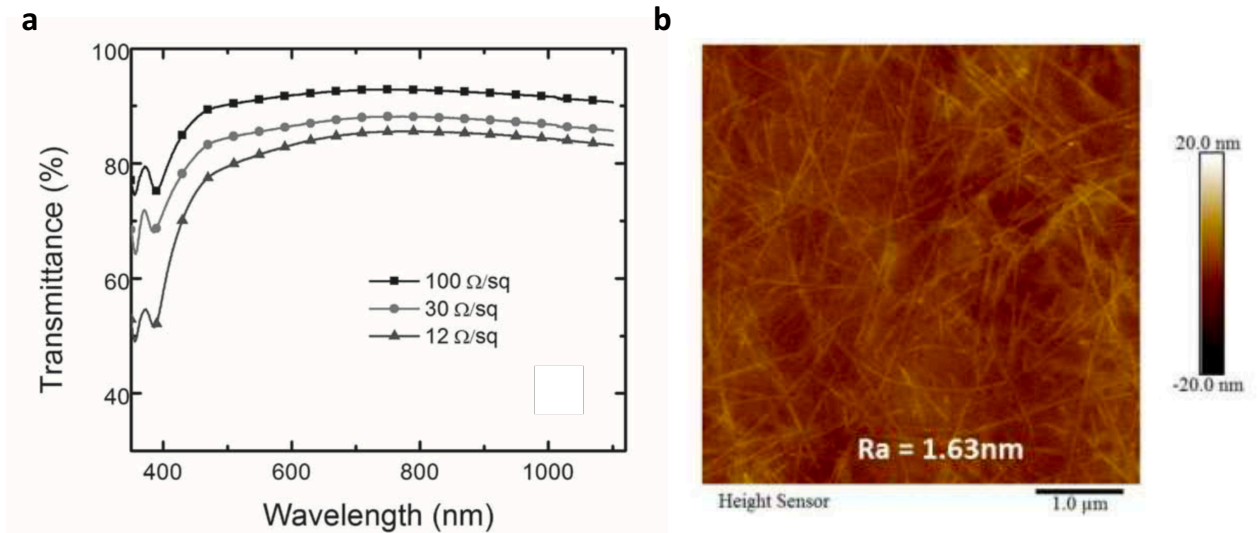


Figure 1.1. a) Transmittance as a function of wavelength for AgNW-acrylate electrodes at various sheet resistances. b) AFM topographical image of a freestanding AgNW-PUA composite electrode with a sheet resistance of 10 ohm/sq .^[6,7]

1.1.2 Flexible AgNW Electrodes

For reasons mentioned above, flexible substrates are desirable for the next generation TCEs and warrants development on this research front to replace conventional TCEs with ITO deposited on rigid glass substrates. Although flexible ITO-based TCEs can be realized by depositing ITO on ultra-thin (100 μm) flexible glass from Schott or Corning, the minimum bend radius of these substrates before risking fracture is 900 mm, which limits its applicability with deformation constraints and suitability for only large format flexible devices. Alternatively, ITO coated on polyethylene terephthalate (PET) substrates has considerably increased flexibility, achieving minimum bend radius of 7 mm; however, fabricating high-quality ITO/PET substrates with high conductivity and transparency comparable to ITO/glass substrates remains a technical challenge.

Another option is to replace ITO with a percolation network of conductive, transparent, yet ductile silver nanowires and replace the rigid glass substrate with transparent, flexible polymer matrices. Silver nanowire embedded in a polymer matrix can be bent down to < 10 mm radius of curvature without causing detrimental cracking of the conductive network. Liang et al. have demonstrated by soldering silver nanowires with graphene oxide, the resulting films can be bent to a radius of 4 mm for over 12,000 cycles with only a 2-3% increase in resistance, and in an extreme case, the AgNW-GO electrodes printed on paper can even sustain 1,000 cycles of folding until forming an inelastic, permanent crease (**Figure 1.2**).^[8,9] The silver nanowire network can withstand high degrees of bending, often restricted only by the flexibility of the surrounding matrix.

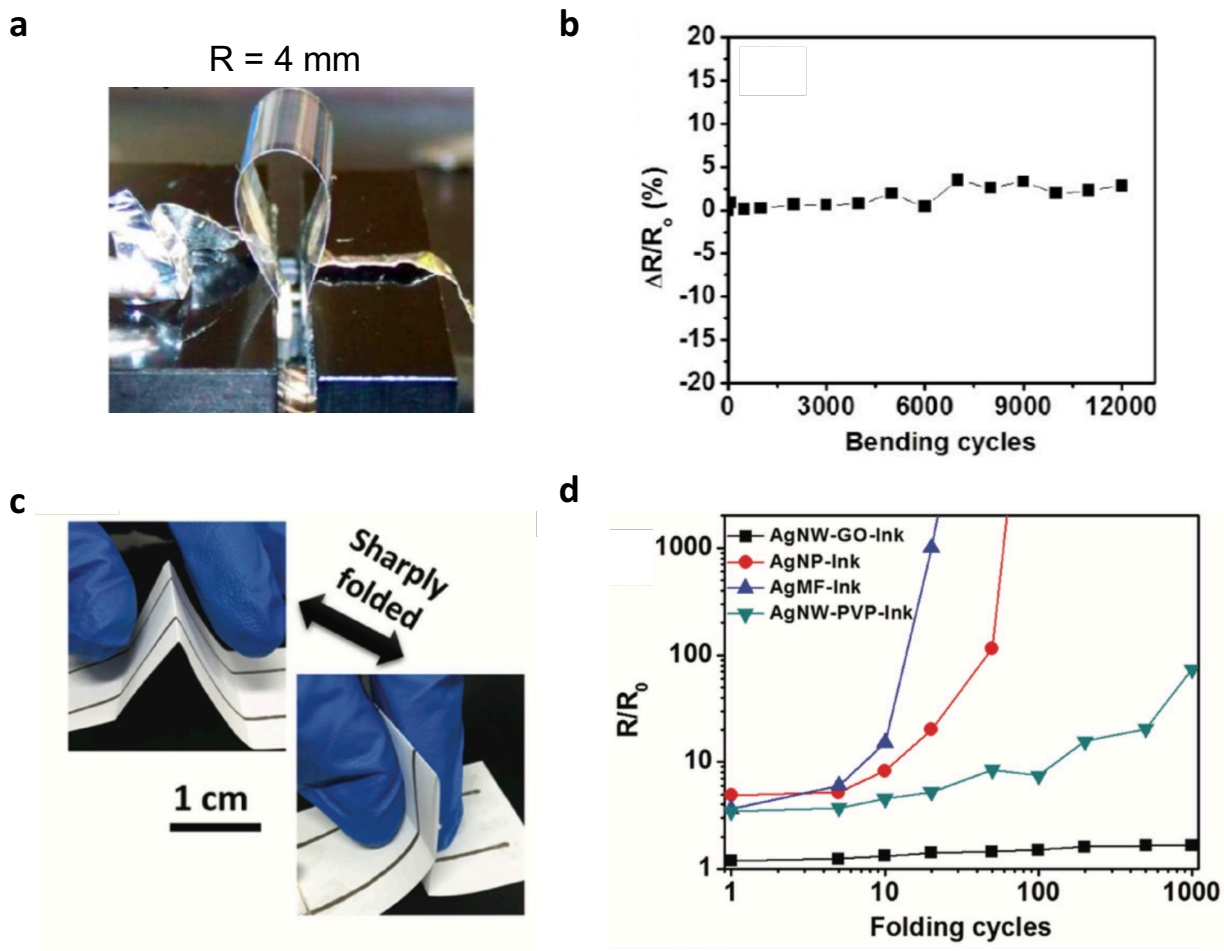


Figure 1.2. a) Photograph of a GO-AgNW/PET composite bent to 4 mm radius. b) Relative resistance change of the GO-AgNW/PET composite during repeated bending to 4 mm radius. c) Photograph of a GO-AgNW electrode printed on paper substrate being sharply folded. d) Relative resistance change of GO-AgNW electrode printed on paper substrate during repeated folding.^[8,9]

1.1.3 Stretchable AgNW Electrodes

The fabrication of high performing stretchable AgNW electrodes is also dependent on the selection of the polymer matrix, with emphasis on the bonding between the nanowires and

polymer and on the stretchability of the composite which is related to the polymer's glass transition temperature and modulus. Ideally, the polymer matrix should be able to withstand repeated stretching cycles at $\geq 70\%$ strain, thus highlighting the importance of selecting an elastomer with a large strain range in its elastic region. For optoelectronic applications, stretchable AgNW electrodes should also have high transparency and low surface roughness ($R_a < 2$ nm) after embedding the nanowires within the polymer matrix, which are primarily affected by the transparency of the polymer, the wettability of the polymer precursor on the AgNWs, and the shrinkage volume of the polymer upon polymerization.

By embedding AgNWs in a copolymer of ter-butyl acrylate (TBA) and acrylic acid (AA), Yun et al. have demonstrated the benign hydrogen bonding effect to form stretchable electrodes.^[10] TBA was chosen in this study for its excellent elasticity and shape memory properties; however, its poor bonding with the nanowires due to its hydrophobicity limits its applicability to form a stretchable composite with AgNWs. To mitigate this issue, the addition of AA enhances the bonding between the copolymer matrix and the nanowires via the hydrogen bonding between the carboxylic acid functional group of the AA and the pyrrolidone functional group of the polyvinylpyrrolidone (PVP) polymer, that is coated on the AgNW surface during the polyol nanowire synthesis, resulting in a reduction in resistance change with increasing strain (**Figure 1.3a**) and with strain-relaxation cycles between 0 and 50% peak strain (**Figure 1.3b**). These AgNW composites with an initial sheet resistance of 10 ohm sq^{-1} were shown to remain conductive with sheet resistance of 10^2 - 10^3 ohm sq^{-1} at strains as high as 140%.^[10] Furthermore, a weight percentage of 5% AA was observed to improve the overall stretchability of the electrode and was found to exhibit 98%, 95%, and 90% resistance recovery after one stretch-relaxation cycle at 30%, 70%, and 90% strain.^[10]

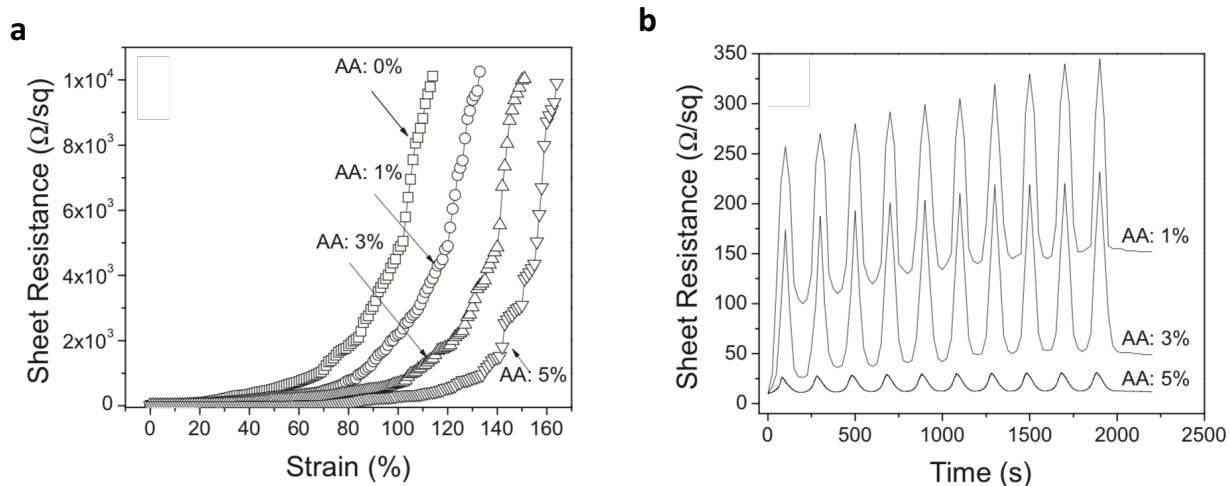


Figure 1.3. a) Change in sheet resistance of AgNW/AA-TBA composite with increasing strain. b) Change in sheet resistance of AgNW/AA-TBA composite during 10 cycles of stretching between 0 and 50% strain at a constant rate of 0.005 Hz.^[10]

By using a polyurethane (PU)-based rubber as the polymer matrix, Hu et al. have shown the contributory effects of the -N(H)- groups to bonds significantly well with the nanowire surfaces which completely transferred the nanowires by minimizing the formation of voids between the nanowires and the matrix. This bonding also enhanced the overall stretchability of the electrode, resulting with a minimal change in resistance of 5.4, 8.0, and 11.9 times at 60% strain for films with initial sheet resistances of 8.0, 16.1, and 24.2 ohm sq^{-1} , respectively (**Figure 1.4a**).^[11] Furthermore, the rubbery elasticity of the PU and the bonding force between the polymer backbone and the nanowires allow the electrodes to obtain full reversibility after a stretch-relaxation cycle at 60% strain and recovered the initial resistance value after being relaxed to 0% strain (**Figure 1.4b**).^[11]

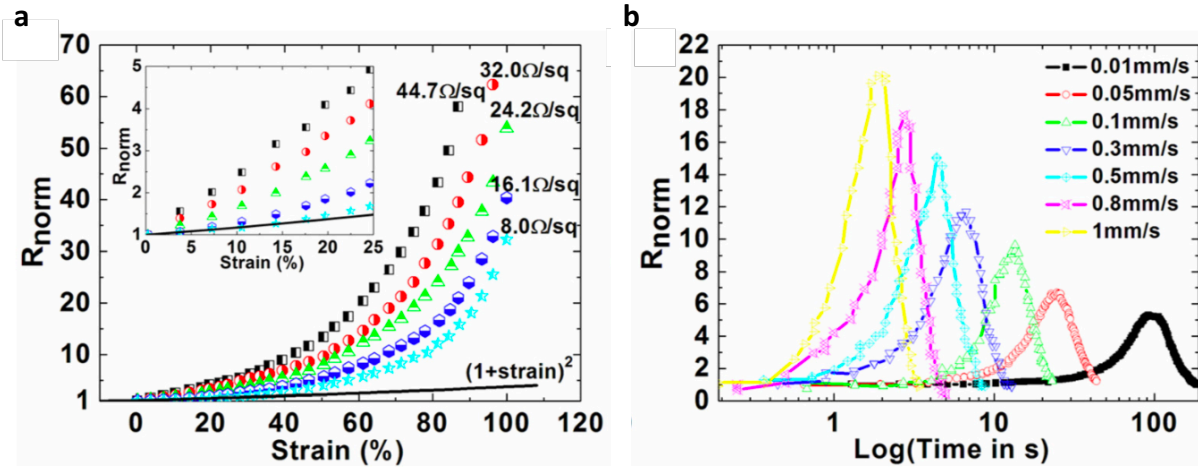


Figure 1.4. a) Change in sheet resistance of AgNW/PU composite with increasing strain. b) Change in sheet resistance of AgNW/AA-TBA composite during a cycle of stretching between 0 and 60% strain at different stretching rates.^[11]

Besides bonding from the functional groups of the polymer matrix, the AgNWs themselves can also be processed to obtain enhanced stretchability. Liang et al. soldered silver nanowire networks through soaking AgNWs coated on release substrates in a 1 mg/mL graphene oxide (GO) in distilled water/isopropyl alcohol solution prior to embedding the nanowires within a polyurethane polymer matrix.^[8] As evident in the SEM image in **Figure 1.5a**, the GO layers condensed at the nanowire junction and prevented inter-nanowire sliding at the junctions. During uniaxial stretching, the deformation of the nanowire network behaves like a fishnet as the nanowire-nanowire contacts remains stationary to minimize resistance change, resulting in a reduction in the increased resistance from 5.4, 9.8, and 17.2-fold (control devices without GO) to 2.3, 5.3, and 10.6-fold at strains of 40, 60 and 80% (**Figure 1.5b**).^[8]

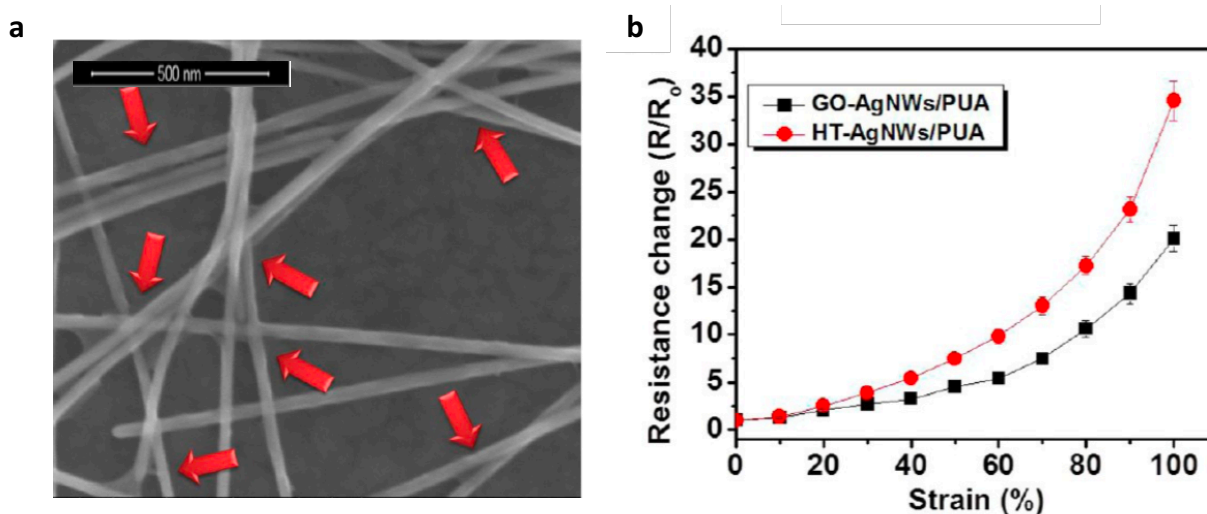


Figure 1.5. a) SEM image of SO-soldered AgNW electrode with red arrow indicating areas with fused junctions. b) Change in resistance of GO-AgNW/PUA composite with increasing strain when stretched at 1 mm/s.^[8]

1.2 Lighting Applications based on AgNW Electrodes

Silver nanowires based TCEs could be used in a wide range of applications, ranging from touchscreens, biosensors, photovoltaics, thin film transistors, transparent heaters, to light emitting devices. Besides functioning simply as a TCE with the aforementioned advantages in good transparency, conductivity, and mechanical compliance, AgNW TCEs have exhibited additional benefit in optoelectronic applications which will be the focus of discussion in the next subsection which introduces the basic working principle of an OLED and the mechanisms behind the advantageous optical effect behind using AgNWs as an ITO replacement. Past developments from our group in the fabrication of flexible and stretchable light emitting devices using AgNW TCEs along with their attained performance will then be discussed. This section

will conclude with a discussion on the integrated systems using self-healable AgNW TCEs and AgNW thin film transistors that provide unique functions to power light emitting devices.

1.2.1 Working Principle of an OLED and the Advantages of AgNW Electrodes

Organic light emitting devices (OLEDs) are attractive in display and solid state lighting applications due to their high power efficiency, unique aesthetics (< 0.3 mm thickness, flexible form factors), broad and tunable spectra, Lambertian emission profiles, and potentially high reliability.^[12-14] Significant progress has been made in the development of materials and device architectures making OLEDs a potential candidate to replace current display and lighting technologies. Development of small molecule organic compounds and polymers have enabled tunable OLEDs with emission in a wide range of wavelengths from deep blue to red. Phosphorescent systems and hybrid fluorescent/phosphorescent systems have been demonstrated to exhibit nearly 100% internal quantum efficiency.^[15-18] To achieve high performing OLEDs in efficiency and lifetime, complex structures with 48+ deposition layers have even been introduced.^[12]

Although the device architectures have become more complex to achieve the desired performance, the structure of a modern-day OLED still consists of the following fundamental structure of substrate / anode / hole transporting layer / emissive layer / electron transporting layer / cathode. Under a forward bias, electrons and holes are injected through the cathode and anode, respectively, and pass through the electron/hole transporting layers which have thicknesses and charge carrier transport properties tailored to promote exciton formation in the emissive layer. The energy of the exciton can be released as a form of a photon, which travels

through the subsequent layers (emissive layer, hole transport layer, anode, and substrate for a bottom emitting device) to be emitted as light from the device.

Developments of OLED material and architecture have achieved $\sim 100\%$ internal quantum efficiency, meaning nearly 100 photons are generated within the device for 100 electron-hole pairs that are injected into the device. However, several factors commonly referred to as the substrate mode, waveguide mode, and the surface plasmon polariton (SPP) mode, limit only a fraction of the generated photons to escape from the device. In general, the direction of light emission within the emissive layer, primarily due to the randomness of the molecular orientation, are anisotropic, and total internal reflection occurs when the incidence angle of the photon is above the critical angle at the layer interfaces. Because of the differences in refractive indices between air ($n = 1$), glass/plastic substrates ($n \approx 1.5$), organic layers ($n \approx 1.7-1.8$), and indium tin oxide (ITO) ($n \approx 1.9$), 20~30% of the generated light is trapped in the substrate (substrate mode), and another 20-30% is trapped in the organic/ITO layers (waveguide mode).^[13,17,19,20] In addition, radiative energy transfer can occur from the decaying dipoles formed by coupling with the thin metallic layer of the cathode forming an optical mode (SPP mode) that propagates as surface waves along the metal-organic interface^[13,21]

To minimize photon lost within the device, light scattering effects from embedded low-index grids, light scattering nanoparticles, and microlens have been demonstrated to enhance the outcoupling of light from the waveguide and substrate modes.^[17,22,23] Coincidentally, AgNW networks are innately light scattering as evident by the difference in diffusive transmittance and total transmittance, leading to an average of 6.8% haze (haze = diffuse transmittance / total transmittance) over the visible spectrum.^[24] Haziness due to scattering could be problematic when used in touchscreens or electrodes for display applications when pixel resolution is a

design criterion but could be advantageous for other applications where scattering is preferred. Better absorption of light in solar cells due to AgNW scattering have been demonstrated to achieve higher solar cell efficiencies,^[25] and enhanced outcoupling with AgNW electrodes in OLED lighting application has also been proven to increase the power efficiency by 60% when compared to reference devices fabricated on ITO/glass substrates.^[26] Besides light scattering, AgNW electrodes reduces the internal waveguide mode since the index mismatch between the organic layers (emissive layers) and the polymer substrate is less than that between the ITO and the glass/polymer substrate, allowing enhanced outcoupling as light rays with wider angles can be extracted from the devices (Figure 1.6).^[27]

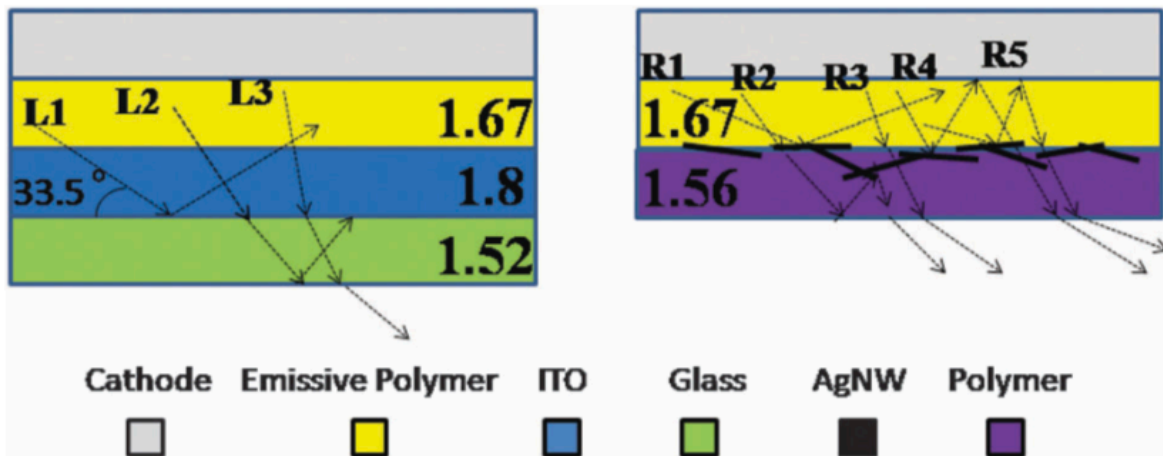


Figure 1.6. Cross sectional schematic of WPLEDs on ITO/glass (left) and AgNW/polymer (right), illustrating the refractive index mismatch between layers of the WPLED stack and the optical mechanism leading to waveguide, substrate, and air modes.^[27]

1.2.2 Flexible Light Emitting Devices

The mechanical properties of the organic molecules in polymer light-emitting electrochemical cells (PLECs), polymer light emitting diodes (PLEDs), and organic light emitting diodes (OLEDs) suggest that light emitting devices can be made that are more flexible than their inorganic counterpart, provided appropriate materials can be found to replace the brittle ITO electrode and the rigid glass substrate. By using spray coated single wall carbon nanotubes (SWCNT) on PET as the anode and substrate, Yu et al. fabricated fully solution processed PLECs, which had performance matrices with turn-on voltage at 3.8 V, a maximum intensity of 1400 cd m⁻² at 10 V, and a maximum efficiency of 2.2 cd A⁻¹ at 480 cd m⁻².^[28] The device characteristic curves are shown in **Figure 1.7**. Typically, surface coated SWCNT electrodes have a detrimentally high sheet resistance of 500 ohm sq⁻¹ at 85% transmittance and surface roughness of > 15 nm, rendering unusable in conventional PLEDs and OLEDs. By utilizing PLECs with ionic conductors and an emissive layer that is more than 10 times thicker than conventional PLEDs/OLEDs, the shortcomings of the SWCNT electrodes were masked allowing for the demonstration of a blue emission device with flexibility down to a radius of curvature of < 2.5 mm without significant change in light emission intensity and uniformity (Figure 1.7).^[28] In comparison, the flexibility of PLEDs fabricated on ITO is limited to a radius of curvature of 7 mm before device failure occurs due to cracking of the brittle ITO layer.^[29]

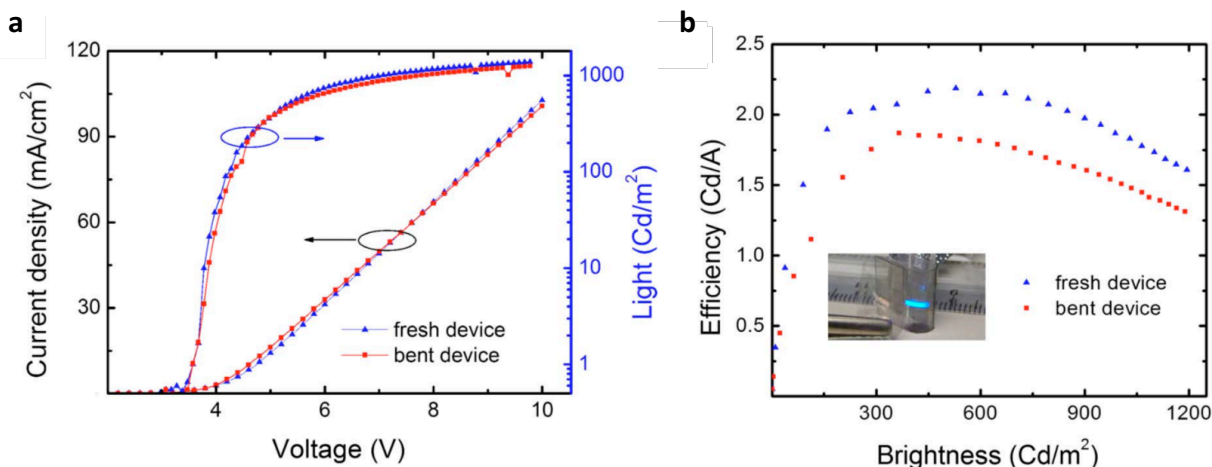


Figure 1.7. Performance characteristics of PLECs on SWCNT/PET electrodes before and after bending to 2.5 mm radius. a) Current-Voltage-Luminance (J-V-L) characteristic. b) Current Efficiency-Luminance (CE-L) characteristics.^[28]

To improve upon the flexible PLEC electrodes, Liang et al. fabricated SWCNT/AgNW electrodes with sheet resistance of 15 ohm sq⁻¹ at transmittance of 81% using Mayer rod coated bilayers of SWCNT and AgNWs that were subsequently embedded in a polymer matrix made of an urethane acrylate, difunctional methacrylate monomer, and tertbutyl acrylate monomer mixture.^[30] As illustrated in the device characteristic curves (**Figure 1.8**), the current density of the device fabricated with the SWCNT/AgNW composite resembles the current density of the devices on ITO/glass electrodes and is higher than the devices on AgNW (only) composite. This enhancement is in part due to the lower resistivity of the AgNW network (in comparison with Yu et al.'s work mentioned above) in conjunction with uniform surface coverage of the SWCNT network that filled the void spaces in between the AgNWs. Furthermore, the light scattering effect, compounded with the removal of the high index ITO layer, allowed an increase in out-

coupling efficiency. As a result, the efficiency of the PLECs on these SWCNT/AgNW composite substrates was shown to exceed that of the PLECs on the reference ITO/glass substrates (**Figure 1.8c**).^[30] As the PLECs were fabricated on the flexible SWCNT/AgNW composite substrates, the devices were able to sustain 10 cycles of bending down to 5.0 mm radius of curvature with only slight degradation in current efficiency (**Figure 1.8d**).^[30]

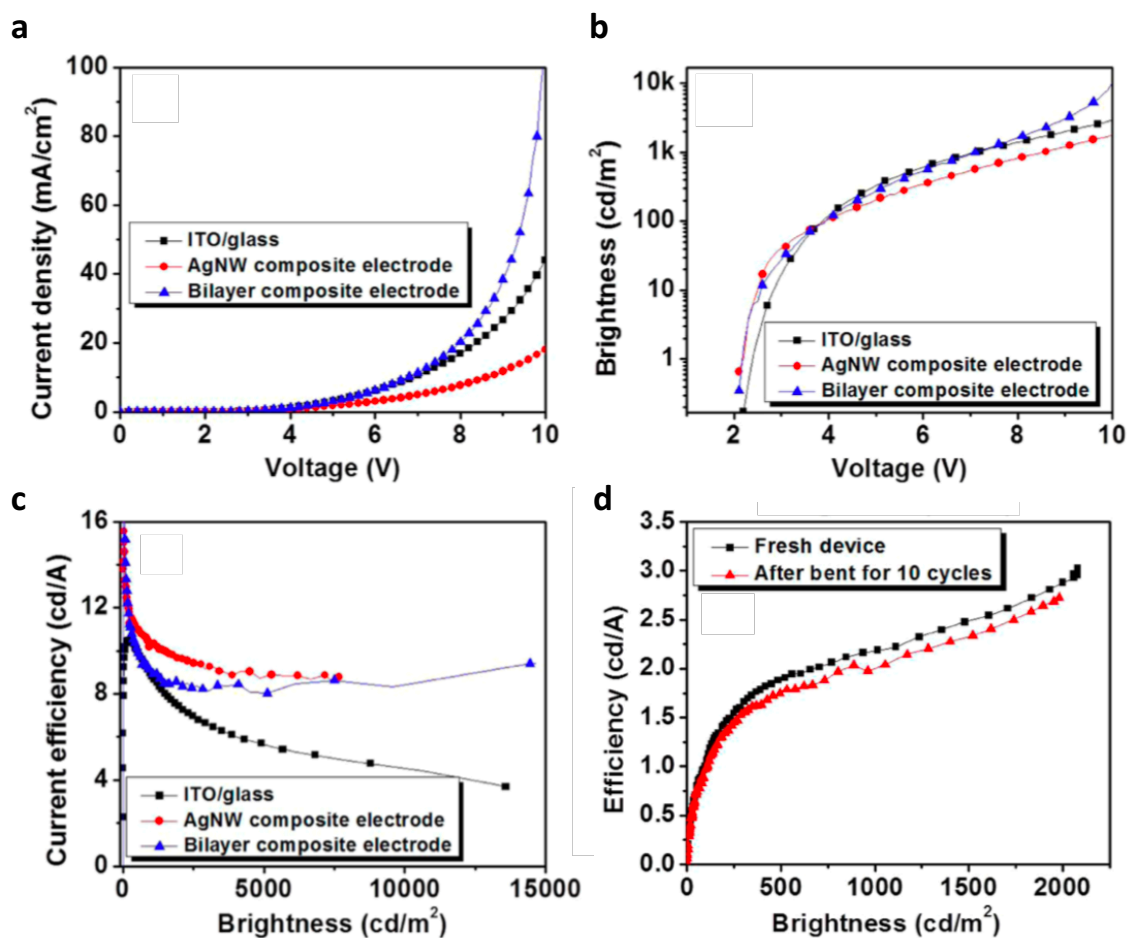


Figure 1.8. Performance characteristics of PLECs on ITO/glass, AgNW/PUA, and SWCNT-AgNW/PUA composites. a) Current-Voltage (J-V) characteristic. b) Luminance-Voltage- (L-V) characteristic. c) Current Efficiency-Luminance (CE-L) characteristics. d) Current Efficiency-Luminance (CE-L) characteristics before and after 10 cycles of bending to a 5.0 mm radius.^[30]

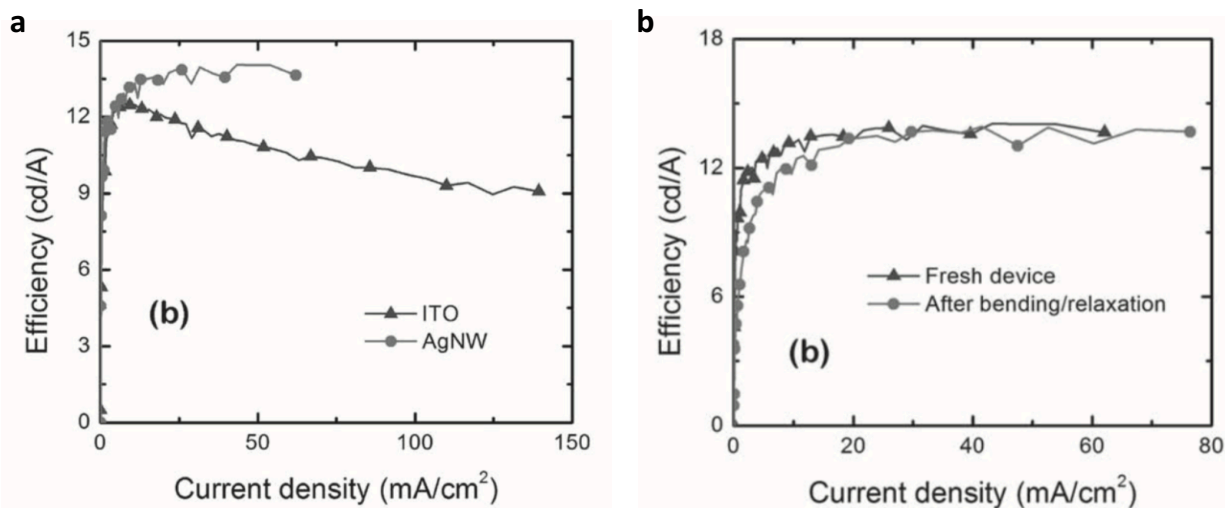


Figure 1.9. Performance characteristics of PLEDs on ITO/glass and AgNW/shape-memory acrylate composites. a) Current Efficiency-Current Density (CE-J) characteristics. b) Current Efficiency-Current (CE-J) characteristics before and after 10 cycles of concave and convex bending to a 2.5 mm radius.^[6]

Besides the aforementioned benefits, the electrodes with the embedded AgNWs exhibit a significantly lower surface roughness than the spray-coated SWCNT electrodes. Yu et al. fabricated AgNW electrodes suitable for the fabrication PLEDs by embedding AgNWs in a shape-memory bifunctional acrylate polymer matrix, achieving surface roughness of less than 5 nm and sheet resistance of 12 ohm sq⁻¹ at 86% transmittance.^[6] The shape memory property of the crosslinked polymer substrate allows the PLEDs to reversibly deform when heated and maintain new shapes when cooled. The PLED on the reference ITO electrodes has a maximum current efficiency of 12.5 cd A⁻¹, which is comparable to reported values for devices with similar device architectures, and the PLEDs on the AgNW substrates achieved a maximum current efficiency of 14.0 cd A⁻¹ (**Figure 1.9a**).^[6] The flexibility of these PLEDs was evident by their ability to withstand concave and convex bending to radius of curvature of 2.5 mm with an

equivalent of 8% tensile strain in the AgNW electrode, while maintaining similar efficiency values at $\sim 12.5 \text{ cd A}^{-1}$ (Figure 1.9b).^[6]

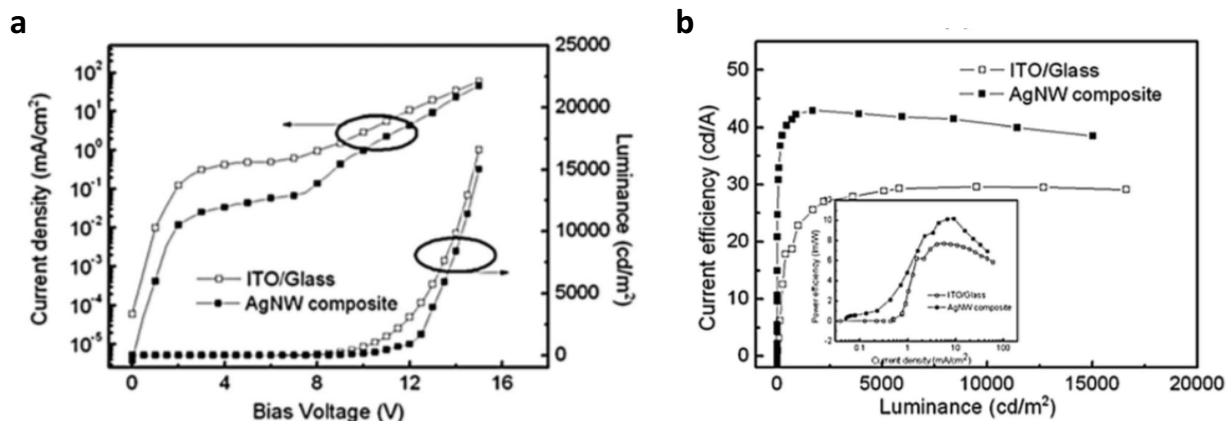


Figure 1.10. Performance characteristics of WPLEDs on ITO/glass and AgNW/polymer composites. a) Current-Voltage-Luminance (J-V-L) characteristic. b) Current Efficiency-Luminance (CE-L) characteristic. Inset shows Power Efficiency-Luminance (PE-L) characteristic.^[27]

When light passes from a material with a higher refractive index to another material with a lower refractive index, the light beam can be trapped within the OLED stack due to total internal reflection at the interface if the incident angle is larger than the critical angle. AgNW polymer substrates have a twofold benefit of extracting more generated light in comparison to devices built on ITO/glass substrates. First, AgNWs embedded in the surface layer of the composite electrodes function as scattering centers, allowing the trapped light beam to change course into a smaller angle, and be extracted from the opposite side of the substrate. Second, ITO in a typical OLED is the material with the highest refractive index. By replacing ITO with AgNW composite electrodes, the index mismatch between the layers is reduced, allowing the generated light from a wider angle to be extracted. Li et al. has reported an enhancement of 41%

to 42.3 cd/A current efficiency from three-complementary color white OLEDs when AgNW-polymer composite was used as the electrode/substrate in replace of ITO/glass (**Figure 1.10**).^[27]

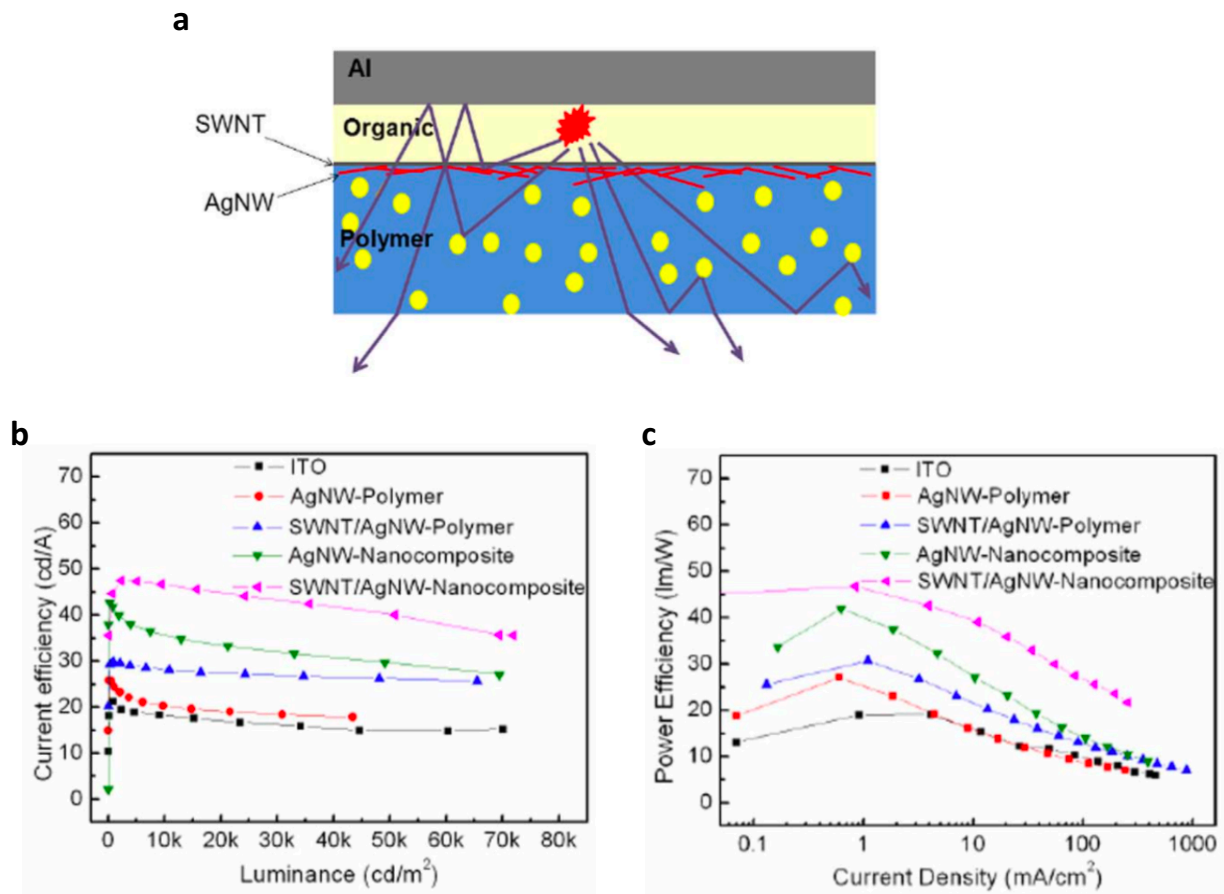


Figure 1.11. Performance characteristics of WPLEDs various substrates. a) Schematic of an OLED with nanocomposite substrate and the optical mechanisms leading to outcoupling of the substrate and waveguide modes. b) Current Efficiency-Luminance (CE-L) characteristic. c) Power Efficiency-Luminance (PE-L) characteristic.^[26]

To further increase efficiency, Li et al. embedded AgNWs and single-walled carbon nanotubes (SWCNT) in a polymer matrix with well-dispersed barium strontium titanate (BST) nanoparticles that act as additional scattering center to enhance light extraction from the

substrate (**Figure 1.11a**).^[26] White PLEDs were fabricated atop these AgNW electrodes with a sandwich structure of substrate / anode / emissive layer / CsF / Al, with the emissive layer being a blend of a white polymer and OXD-7 in a 5:2 wt. ratio. The values of current, power, and external quantum efficiency of the AgNW / SWCNT / polymer with BST devices were 47.5 cd A⁻¹, 46.8 lm W⁻¹, and 30.5%, respectively, representing an average enhancement of 2.2X, 2.5X and 2.2X compared to respective values obtained from devices built on ITO/glass substrates (**Figure 1.11b**).^[26]

The flexible light emitting devices described in this section have proven the advantages of the AgNW or AgNW/SWCNT electrodes over traditional ITO electrodes in increasing light outcoupling efficiency and providing mechanical flexibility. The effect of the photon scattering by the nanowires and the reduced refractive index mismatch between the interlayers by replacing the ITO electrode contributed to a reduction in light trapped within the anode and substrate layers as evident by the reduced edge emission and the numerous reports of enhanced efficiency. The devices fabricated atop the AgNW-based electrodes could withstand bending down to a radius of curvature of 2 mm, in comparison to 7 mm of ITO, without showing a significant reduction in device performance. Polymer matrices with different components were also demonstrated to provide flexibility, shape memory capability, and additional light extraction capability, showing the ease of adaptability of the anode / substrate composites for different functionalities using the AgNW transfer process.

1.2.3 Stretchable Light Emitting Devices

Though the AgNW electrodes have permitted light emitting devices to achieve a degree of flexibility that is imperceptible in traditional transparent conductive electrodes, its capability to withstand large strain without detrimental failure have propelled this material to the forefront among promising candidates for next generation, mechanically compliant TCEs. The mechanical properties of the stretchable AgNW composites are primarily influenced by the mechanical behavior of the matrix material. Unlike the flexible AgNW electrodes, the limitation of the stretchable AgNW electrodes is more profound as the resistance increases with increasing strain. This section will first provide a brief introduction to the fabrication process of the stretchable PLECs fabricated on AgNW electrodes embedded in a stretchable rubbery polymer, followed by a discussion of its light emitting behavior under mechanical strain. Next, stretchable WPLEDs with improved stretchability using electrodes of graphene oxide soldered AgNW embedded in a PUA matrix will be discussed.

Liang et al. embedded AgNWs in a rubbery PUA matrix and fabricated a fully solution processed elastomeric polymer light-emitting electrochemical cell (PLEC), sandwiched between two AgNW-PUA electrodes, comprising SuperYellow as a yellow light emitting polymer, ethoxylated trimethylolpropanetriacrylate (ETPTA) as the ionic conductor, polyethylene oxide (PEO) as a second ionic conductor to enhance the stretchability of the ETPTA network, and lithium trifluoromethane sulphonate (LiTf) as the salt.^[5] The thin poly(3,4-ethylenedioxythiophene) : poly(styrene sulphonate) (PEDOT:PSS) layer was coated on the anode to protect the PUA matrix from solvent attack in the subsequent coating of the electroluminescent polymer layer. The resulting PLEC turned on at 6.8 V and reached a peak brightness of 2,200 cd m⁻² at 21 V with calculated external quantum efficiency (EQE) of 4.0%,

comparable to state of the art PLEC based on SuperYellow fabricated on ITO/glass substrate.^[5] The device can be uniaxially stretched to 120% strain before failing to emit light. Due to the high stretchability and conductivity of the AgNW-PUA composite electrodes, the PLEC can be stretched, bent, and folded to conform to curvilinear surfaces. **Figure 1.12** illustrates the device stretched to various strains and wrapped around the edge of a 400 μm thick cardboard while maintaining uniform and bright emission.^[5] The robustness of the stretchable AgNW TCE was demonstrated by the fairly stable current efficiency and brightness of the PLEC after 1,000 continuous stretch-relaxation cycles with strains between 0% and 30%. At 40% or larger strain, the electroluminescent performance of the devices deteriorates rapidly as irreversible damages of the emissive and PEDOT layers were observed.

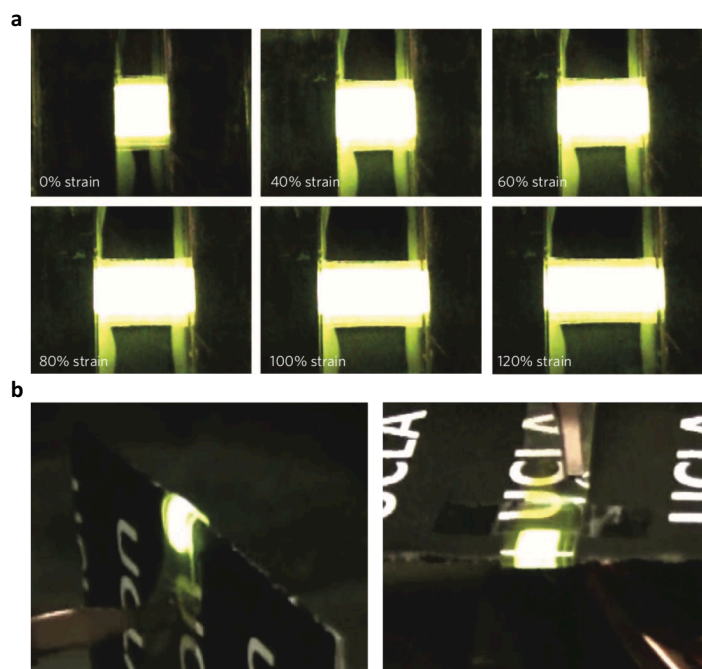


Figure 1.12. Mechanical deformation of PLECs on AgNW/PUA composites. a) PLECs stretched from 0 to 120% strains under a 14 V bias. b) PLECs wrapped around the edge of 400 μm -thick cardboard under a 12 V bias.^[5]

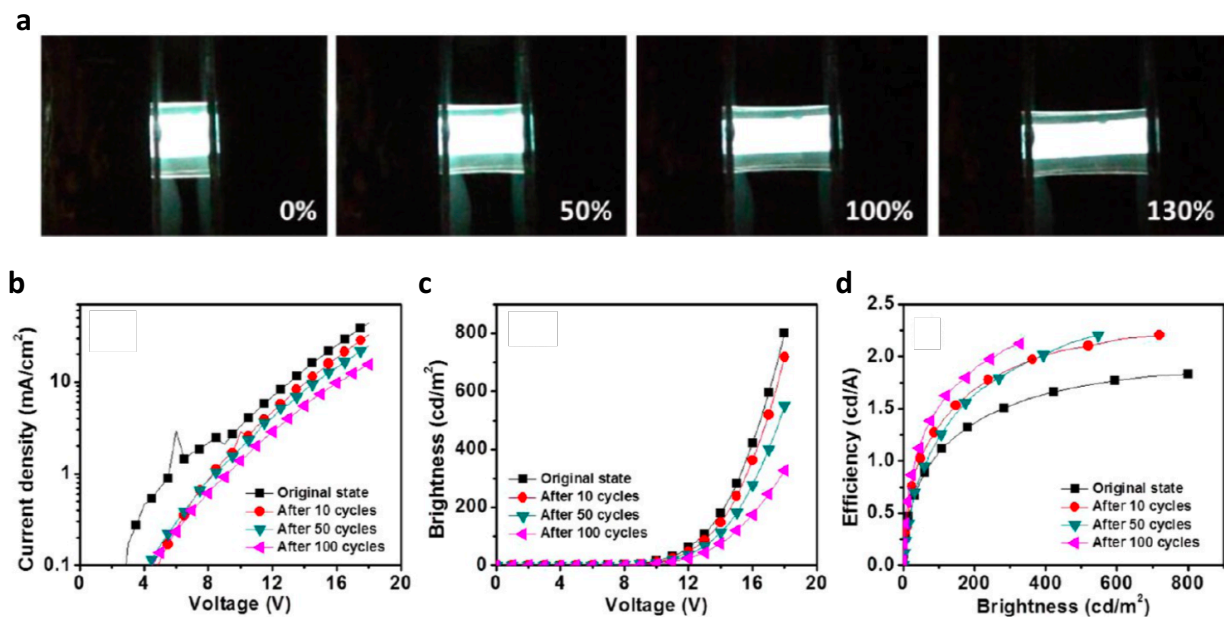


Figure 1.13. Mechanical deformation of PLECs on GO-AgNW/PUA composites. a) PLECs stretched from 0 to 130% strains under a 13 V bias. b-d) Device characteristics after stretching cycles between 0 and 40% strains.^[8]

Liang et al. also fabricated stretchable white polymer light emitting diodes (PLED) using GO-soldered AgNW TCEs embedded in a PUA matrix.^[8] The devices consist of the structure: PUA / GO-AgNW anode / PEDOT:PSS hole transport layer (HTL) / an emissive layer comprising a white light emitting polymer and OXD-7 / polyethyleneimine (PEI) electron transport layer (ETL) / GO-AgNW cathode / PUA. The PLED shows comparable performance to that observed with the stretchable PLEC and operates at a lower voltage. The PLED can survive after 100 continuous stretch-relaxation cycles with strains between 0% and 40% and shows fairly uniform emission when stretched up to 130% linear strain at room temperature, with an increase in current efficiency from an initial value before stretching at 1.5 cd A⁻¹ to 2.1 cd A⁻¹ (**Figure 1.13**).^[8] Changes in charge injection interfaces, thickness of the emissive layer, molecular orientation, charge balance, and reduced leakage current are possible factors that affected the

efficiency of the stretchable PLEDs after being stretched.^[8] Research in stretchable light emitting devices is still in its early stages of development with potential improvements in bonding between the layers and stretchability of the semiconductors; nonetheless, AgNW TCEs discussed in this subsection have introduced new functionalities to traditional light emitting devices and provided a framework for the development of stretchable devices in future applications.

1.2.4 Integrated Systems for Lighting using AgNWs

By modifying the polymer constituents, Li et al. embedded AgNWs in an ultrathin soldering copolymer layer of polyester acrylate and furfuryl methacrylate (P(PA-FM)) that effectively lowers the sheet resistance of the transparent composite electrode and facilitates chemical bonding with the underlying transparent, healable copolymer substrate of furan oligomer and 1,8-bis(maleimido)-1-ethylpropane (P(FR-BME)). The healable copolymer allows recovery of surface conductivity as the damaged electrode could be recovered by heating through Diels-Alder cycloaddition reaction. The AgNW - (P(PA-FM)) - (P(FR-BME)) electrodes with an original resistance of 18 Ω /sq were severed with a 40 μ m deep surface incision, causing the resistance of the film to increase to infinity. After the film was heated at 100 °C for 6 min, the resistance of the electrode recovered down to $21 \pm 1 \Omega$ /sq.^[4]

To evaluate the robustness of the healed films, the recovered films were repeatedly bent to a diameter of 5mm and a total resistance increase of 6.8% was observed after 1,000 cycles.^[4] Capacitive touchscreen sensors made with the AgNW-(P(PA-FM))-(P(FR-BME)) electrodes were fabricated atop a LED display, and **Figure 1.14** illustrates the healable functionality of these devices as a fully operational touch screen was cut along the red dash line to decouple the

electrodes to the left of the cut line, rendering half of the touchscreen to become nonfunctional. Upon heating at 80 °C with a hair dryer for 30 s, the left half of the screen could regain its capacitive sensing function.^[4] The healable characteristic of the composite electrodes allows the light emitting device to operate even after crack formation and paves the foundation to fabricate various devices with the aim of fault-tolerant, longer-lasting electronic devices.

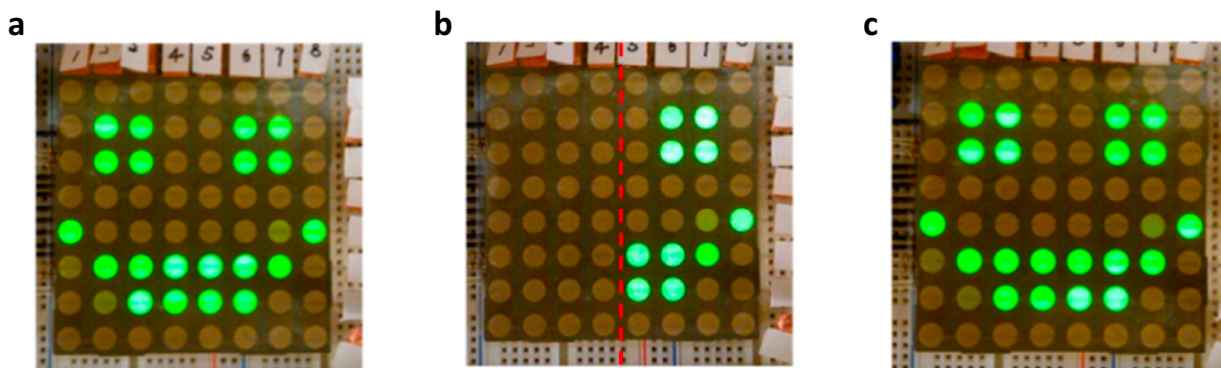


Figure 1.14. Demonstration of the healing capability of the touch screen. a) Before cutting. b) After cutting along the red dash line. c) After healing at 80 °C for 30 s with a hair dryer.^[4]

Stretchable thin film transistor (TFT) arrays, serving as the on-/off- switches, is a critical component to control the pixels of fully stretchable displays. To investigate the applicability of AgNW electrodes in stretchable TFTs, Liang et al. fabricated TFTs with AgNW/PUA electrodes as the source and drain, SWCNT as the semiconducting channel, and polyacrylate-co-polyethylene glycol (PA-co-PEG) as the elastomeric dielectric.^[31] The stretchable TFTs were used to drive white-light OLED by connecting the drain of the TFT to the cathode of the OLED and applying a negative voltage to the anode of the OLED. Before being stretched, a mobility of $30 \text{ cm}^2 \text{ V}^{-1} \text{ s}^{-1}$, on-off ratio of 10^3 - 10^4 , switching current $> 100 \text{ } \mu\text{A}$, and transconductance of $> 50 \text{ } \mu\text{S}$ was obtained. At 50% strain, the mobility decreased to ~ 16.2 due to the decreased

capacitance of the dielectric layer, but the on-off ratio remains relatively constant. The output and transfer characteristics of the OLED control circuit with the stretchable TFT under 0, 20, and 30% strains are presented in **Figure 1.15**. Under 20 and 30% strains, field-effect transistor-like behavior was still observed with a gate voltage (V_G) modulation factor of ~ 1000 , 750, and 650 under strain of 0, 20, and 30%, respectively. With increasing strain of the TFT, the I_{OLED} flow through the OLED decreased from $\sim 80 \mu\text{A}$ at 0% strain to $\sim 50 \mu\text{A}$ at 30% strain.^[31]

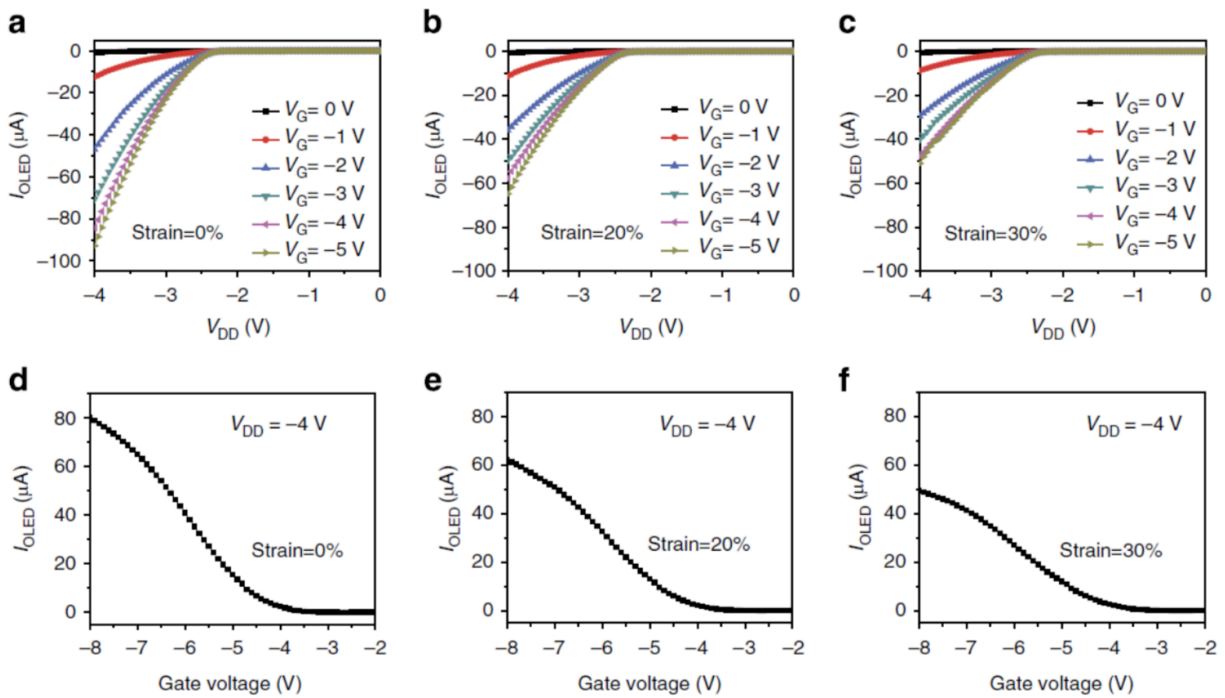


Figure 1.15. Output ($I_{\text{OLED}}-V_{\text{DD}}$) characteristics of the OLED controlled by a stretchable SWCNT-AgNW TFT. The TFT is stretched along channel length direction by (a) 0%, (b) 20% and (c) 30% strains, with varying V_G from 0 to -5.0 V in 1V increments. Transfer ($I_{\text{OLED}}-V_G$) characteristics at V_{DD} of -4.0V under 0% (d), 20% (e) and 30% (f) strains.^[31]

The light-emitting properties of the OLED circuit at different V_G when V_{DD} is -4 V are shown in **Figure 1.16**, which illustrates the brightness of the OLED integrated with TFT under 0, 20, and 30% strain. When the TFT was stretched with 20% strain at $V_G = -8$ V, the brightness decreased from 196 cd m^{-2} to 120 cd m^{-2} , which are still within the functional range of most display applications. Though the brightness of the OLED devices decreased to 63 cd m^{-2} at 30% strain at $V_G = -8$ V, good diode behavior with clear cutoff and diode regions were still observed, highlighting the adaptability of the stretchable TFT. Though the TFTs were not used to drive a stretchable light emitting device, this work demonstrated the proof of concept in fabrication, processing, and characterization of silver nanowires in integrated systems for stretchable display technology, paving the way to a wide range of applications for future flexible, stretchable devices.


















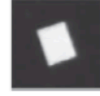



V_G	-2.0 V	-4.0 V	-4.5 V	-5.0 V	-6.0 V	-7.0 V	-8.0 V
TFT under 0% strain	0 cd m^{-2} 	6.9 cd m^{-2} 	50 cd m^{-2} 	84 cd m^{-2} 	112 cd m^{-2} 	183 cd m^{-2} 	196 cd m^{-2} 
TFT under 20% strain	0 cd m^{-2} 	4.5 cd m^{-2} 	33 cd m^{-2} 	51 cd m^{-2} 	98 cd m^{-2} 	110 cd m^{-2} 	120 cd m^{-2} 
TFT under 30% strain	0 cd m^{-2} 	0 cd m^{-2} 	7.5 cd m^{-2} 	33 cd m^{-2} 	48 cd m^{-2} 	57 cd m^{-2} 	63 cd m^{-2} 

Figure 1.16. Luminance of an OLED driven by a stretchable TFT under various V_G at strains of 0, 20, and 30% when V_{DD} is -4.0 V.^[31]

1.3 Motivation and Research Scope of this Dissertation

Since the advent of organic light-emitting diodes (OLEDs), improvements in the electrical and thermal stabilities, transport properties, luminescence quantum yields, mechanical deformability, low-power consumption, ease of fabrication, and color quality have propelled OLED technology to the forefront of the replacement lighting market.^[11] The U.S. Department of Energy has funded ~ \$400 million since December 2000 on solid-state lighting (SSL) projects for the development of energy-efficient LED and OLED products. Due to the high efficiency of LED (~160-170 lm/W) in comparison to incandescent (~15 lm/W) and fluorescent bulbs (~50-100 lm/W), the current usage of LED products has contributed to more than \$2.8 billion in U.S. energy saving. Driven by the magnitude of progress made to date, the Department of Energy continues to drive for continuous developments in solid-state lighting technology. Although OLED technology in lighting applications have yet to make as large of an impact as LED technology as it is still in its early stage of development, the potential for further efficiency improvement and flexible panels have gathered the Department of Energy's investments in the continual support of its core technology research and its product and manufacturing developments.

Efficiency and cost are two of the biggest hurdles to lay the foundation of early market success for widespread adoption of OLED technology. Current OLED light panels manufactured by LG Display and OLEDWorks are marketed with a mere power efficacy of ~60 lm/W. While both companies have announced the release date of their next generation of panels with power efficacy up to ~80-100 lm/W within two years, OLED lighting products are still substantially lower in efficiency than their LED counterpart. Cost is another factor that eludes potential buyers from current OLED products. Some of the more affordable OLED light panel manufactured by a

luminaire company, Acuity Brands, can be purchased at Home Depot for about \$160-300. A similar panel powered by LED technology can be found for less than half the price with more than twice the efficiency and clearly demonstrates the lack of competitiveness that OLED light panels have in the current market.

In order for OLED lighting products to be more appealing to consumers, flexibility, efficiency improvement, and cost reduction has to be achieved. Flexibility will provide new design options for luminaires to develop appealing high-end products, such as automobile taillights and decorative light panels with intricate designs, where the cost would be a smaller marketing factor, and the additional lowering in price by the reduction in materials and fabrication costs will together increase the marketing appeal of OLED products. An economic assessment by Emmott et al. has indicated the materials and fabrication cost of AgNW transparent conductors is less than one-third of the cost of its ITO counterpart, which has the potential to reduce the module costs of the devices per Watt by 17%.^[32] In effort to propel the development of OLED technology, the objective of my research is to focus on the development of integrated strategies to develop a low-cost approaches for the fabrication of flexible OLED substrates with priorities in high optical enhancement and color quality to achieve the goal of providing future design options of OLED panels that requires low energy usage.

Silver nanowires have been demonstrated to display unparalleled properties in transparency, conductivity, and mechanical compliance. Due to their ability to form a percolation network that can be embedded within a polymer matrix to form conductive electrodes with low surface roughness, the AgNW electrodes is suitable for in a wide range of applications from light emitting devices to TFT arrays to capacitive sensors. The versatility of AgNW composite electrodes has been highlighted in this chapter showing their versatility to be tailored for specific

applications by modifying the matrix material, with properties to enhance flexibility, stretchability, healability, and light extraction. Though the fabrication and processing of the basic AgNW transparent conductors have been relatively matured, application specific composite electrodes still require further development to maximize the potential of AgNW composites.

In the examples discussed in this chapter, the AgNW electrodes were coated as a uniform thin film prior to being embedded within a polymer matrix. Although conventional processing methods, such as laser ablation and photolithography etching, could be used for precise patterning of the electrodes, excessive materials are wasted, and undesired byproducts might be left through the removal process. Instead of relying on a relatively expensive removal process, chapter 2 details the development of a screen printing process capable of printing features at 50 μm resolution through the development of a viscoelastic AgNW screen printing ink. By using the screen printing process to pattern electrodes for the fabrication of TFTs and low resistance high transparency OLED substrates, improvements in device performance was observed, providing a solution-processed alternative that opens up opportunities to utilize this type of material in a cost-effective approach.

In addition to the process development in patterning, the scope of this dissertation also includes the incorporation of AgNW networks towards the development of low-cost approaches for the fabrication of flexible, high performing OLED substrates. Though LEDs are currently dominating the replacement lighting market due to its superiority in performance, stability, and cost, OLEDs have attracted increasingly higher levels of attention with its aesthetics, flexibility, color tunability, and potentially high efficiency. Flexible OLEDs offer innovative design options, often desired in niche markets such as airports and luxury hotels. Further reduction in cost and improvement in efficiency will open up larger markets for OLED lighting in automobile, retail,

hospitals, commercial, and residential sectors. The following few chapters further expand on additional developments on the integrated fabrication of the AgNW anode and polymer-based substrate for enhanced light extraction and color tunability through the study of the synergetic effects of silver nanowires, high index polymers, light scattering nanoparticles, and down-conversion phosphors in anode/substrate architectures that influence the emission behavior of OLEDs with the goal of improving the efficiency and color quality to light up a brighter and greener future in the years to come.

Chapter 2

Water Based Silver Nanowire Screen-Printing Ink

2.1 Introduction

Printed electronics have drawn tremendous interest during the past few decades.^[33-44] Printing technologies not only enable high volume and versatile manufacturing with low environmental impact and low cost but also help flexible electronic devices such as displays, actuators, and sensors to penetrate the broad consumer markets.^[33] While flexible printed electronics are increasingly gaining attention in both the scientific and industrial communities, rubbery stretchability in addition to an increase in flexibility is also desired in various stretchable/wearable electronic applications.^[31,45-49] A major material challenge to fabricate stretchable printed electronics is to develop a printing method for creating stretchable conductors or electrodes with suitable electrical properties. Traditional carbon-based materials, such as carbon nanotubes (CNT), and metals, such as silver flakes/nanoparticles, are widely used in formulating printable conductive ink or paste for stretchable conductors.^[45-49] Baik *et al.*

reported highly conductive, printable and stretchable hybrid composites composed of micrometre-sized silver flakes and CNTs decorated with self-assembled silver nanoparticles. Chun *et al.* reported a printed stretchable conductor with a conductivity of $5,710 \text{ S cm}^{-1}$ at 0% strain and 20 S cm^{-1} at 140% strain.^[48] A stretchable silver microelectrode has been patterned by omnidirectional printing of concentrated silver nanoparticle inks in both uniform and high-aspect ratio motifs with minimum widths of approximately $2 \text{ }\mu\text{m}$.^[45] Someya *et al.* introduced printable elastic conductors comprising single-walled carbon nanotubes (SWCNTs)^[46] and silver flakes^[50] that are uniformly dispersed in fluorinated rubber, which could be stretched with large strain. These reported conductors/electrodes were fabricated by solution-based printing methods and were all provided with impressive stretchability characteristics; however, their initial conductivity (conductivity at 0% strain) was much lower than that of typical un-stretchable silver pastes.

Recently, metal nanowires, such as silver nanowires (AgNWs), have attracted significant interest for electronic applications. Due to the high conductivity of silver, AgNW has shown promise in low sheet resistance and high visual transparency essential for transparent electrodes/conductors.^[8,51,52] COMSOL numerical simulation indicates that the AgNW networks have excellent mechanical compliancy due to the large length-to-diameter aspect ratio of AgNWs.^[5,53] Moreover, poly(vinylpyrrolidone) (PVP), which is introduced to control the growth of AgNWs during the nanowire synthesis, can serve as a surfactant and help finely disperse AgNWs in solutions.^[54,55] All these features make AgNW an interesting candidate for printable and stretchable conductor/electrodes in next-generation printed electronics.^[31]

Of the existing printing methods, screen printing (also called stencil printing), which uses emulsion screens, mesh-mount or frameless metal stencils to deposit inks and pastes onto various

substrates, is a widely used technique in printed electronics due to its low capital cost, versatile pattern designs, simple operation, and minimal byproducts.^[33,41–43,56,57] Currently, the printed pattern resolution can achieve as high as 40-50 μm , which can satisfy certain electronic application requirements. Generally, the screen-printed conductive line characteristics are also highly related to the properties and printability of the conductive pastes/inks, which depend on solid loading, particle dispersion, viscosity and rheology behavior, particles specific surface area and density, and so on.^[57] A large number of publications and commercial products utilize spherical and/or flake shape silver particles, and carbon-based fillers, such as graphite, single wall carbon nanotubes (SWCNTs) and graphene, to formulate conductive screen-printing inks for flexible electronics.^[33,42,57–63] Zhou *et al.* reported the first fully screen-printed top-gated TFTs array on flexible substrates using silver-based conductive inks for source, drain and gate electrodes.^[33] Recently, a high-resolution patterning of pristine graphene with decent performance was also produced by screen printing for flexible electronic applications.^[42] Despite great success being achieved in the field of flexible screen-printed electronics, few have succeeded in developing screen-printable inks with high stretchability and conductivity for stretchable/wearable electronic applications.^[47,50]

In this chapter, high-resolution solution-printed patterns of AgNWs both on flexible polyethylene terephthalate (PET) and rigid glass substrates via screen printing approach is reported. A water-based formulation of AgNW ink with rheological behavior that correlates the ink rheological properties with ink compositions was developed to pattern AgNWs down to a minimum feature size of 50 μm for the printed line width and spacing between lines. The initial conductivity of the printed AgNW lines (before stretching) could be achieved up to $4.67 \times 10^4 \text{ S cm}^{-1}$. Stretchable conductors based on screen-printed AgNW patterns inlaid in the surface layer

of polyurethane acrylate (PUA) shows rubbery stretchability while retaining high electrical conductivity of $> 10,000 \text{ S cm}^{-1}$ at 70% strain. Stretchable/wearable thin-film transistor (TFT) arrays were demonstrated based on the screen-printed AgNW/polyurethane acrylate (PUA) composite conductors as stretchable source and drain electrodes. Also, screen-printed AgNWs using a stainless steel stencil was demonstrated to print highly transparent flexible OLED substrates, resulting in further enhancement in light extraction in comparison with an OLED substrate fabricated with a uniform layer of AgNWs.

2.2 Experimental Section

2.2.1 Materials

AgNWs were purchased from Zhejiang Kechuang Advanced Materials Co., LTD. Siliconized urethane acrylate oligomer (CN990), ethoxylated bisphenol A dimethacrylate (SR540), polyethylene glycol (200) diacrylate (SR259), methoxy polyethylene glycol (350) monomethacrylate (SR550), and ethoxylated trimethylolpropane triacrylate (SR499) were supplied by Sartomer. 2,2-Dimethoxy-2-phenylacetophenone (photoinitiator), (hydroxypropyl)methyl cellulose(average Mn ~ 10,000), propylene glycol, cesium fluoride (CsF), and aluminum pallets were obtained from Sigma-Aldrich. Semiconducting SWCNT (99%+) was obtained from Nanointegris Inc. Zonyl FS-300 was purchased from Fluka. Defoamer MO-2170 was requested from BASF. Fluorosurfactant FC-4430 was purchased from 3M. PEDOT:PSS (Clevios A14083) was purchased from Heraeus. N,N'-di(naphthalene-1-yl)-N,N'-diphenyl-benzidine (NPB) was purchased from Jim OLED Materials Tech. Iridium bis(4-phenylthieno[3,2-c]pyridinato-N,C2') acetylacetonate (PO-01) and Bis(2-(2-hydroxyphenyl)-pyridine) beryllium (BePP₂) were obtained from Lumtec.

2.2.2 Preparation of Screen-Printing AgNW Ink

An additive solution of distilled water, propylene glycol, (hydroxypropyl)methyl cellulose, Zonyl FS-300 and antifoaming agent were mixed at a weight ratio of 5 : 5 : 1 : 0.002 : 0.01 and sonicated for 2 h. The stock AgNW solution (1 wt% in isopropanol), distilled water, and the additive solution were then mixed at the weight ratio of 4 : 4 : 1 using a vortex mixer at 1,000 rpm for 1 h, followed by drying the dispersion completely via vacuum rotary evaporation. While all additives to AgNW solid ratio were kept constant for all the formula, three different weight percentage of distilled water were added back to the dried mixture to make three different inks with different AgNW solid contents: 6.0 wt% (AgNW Ink-L), 6.6 wt% (AgNW Ink-M), and 7.3 wt% (AgNW Ink-H). The mixtures were agitated aggressively using stir bars at 1,000 rpm for 1 h to obtain the final AgNW inks.

2.2.3 Screen Printing and Post Treatment

Screen printing were performed using a HMI Model MSP- 088 Bench Top Thick Film Screen Printer and a 12" × 12" precision stainless steel screen mesh (400 mesh count, 0.0007 inch wire diameter, 0.0018 inches mesh opening, standard mesh tension, 22 degrees mesh angel, 0.0008 in emulsion thickness, emulsion is safe with water) ordered from Sefar Inc.. A 6.5" Squeegee with ergonomic holder formed a ~ 45° angle with the screen mesh, and the printing speed was ~ 60 mm/s with printing force at ~ 32.2 N. The printed AgNW patterns were first annealing at 150 °C for 5 min, followed by washing with an ethanol and water mixture (1:20) for 5 min. Then, the AgNW pattern was heated to 150°C again for 5 min, followed by washing with water for 5 min. Finally, the coating was annealed at 150°C for 5 min to obtain the final conductive AgNW pattern.

2.2.4 Fabrication of Stretchable Composite Conductors

The above AgNW pattern printed on release substrate was then over-coated with a precursor solution containing 100 weight parts of CN990, 20 parts of SR540, and 1 part of the photoinitiator (2,2-Dimethoxy-2-phenylacetophenone).^[5,31] The coatings were cured under UV at 2.5 W/cm² intensity and peeled off of the release substrate. The screen-printed AgNW pattern was thus transferred as the conductive surface of the resulting stretchable composite conductor.

2.2.5 Fabrication of Fully Printed TFT Array

The TFT array fabrication started with screen printing 10 × 6 pairs of AgNW source/drain electrodes with channel length of 50 μm and channel width of 1,000 μm on glass substrate, followed by post-treatment to recover the conductivity and then transferred into the surface layer of PUA to make stretchable composite source/drain electrodes. 2 μl SWCNT ink, which was prepared by mixing 99%+ Semiconducting-SWCNT aqueous solutions, distilled water, propylene glycol and Fluorosurfactant FC-4430 at the ratio of 25:5:5:1, was uniformly drop-casted on each channel, followed by heating to 90 °C on a hot plate to dry the SWCNT network. The SWCNT/AgNW-PUA source/drain was rinsed with distilled water and isopropyl alcohol alternatively to remove the sodium dodecyl sulfate surfactant and Fluorosurfactant, followed by drying in vacuum for 1 h. Subsequently, the elastomeric dielectric precursor, which was prepared by mixing the components CN990, SR259, SR550 and photoinitiator in an weight ratio of 1 : 1 : 1 : 0.015, was over-coated on the SWCNT/AgNW-PUA source/drain substrate, spin-printed at 8,000 rpm for 1 min and then UV-cured in nitrogen gas. 3M transparent tape was used to define the openings for the source/drain electrode and peeled off after polymerizing the elastomeric dielectric. Finally, the resulting elastomeric dielectric/SWCNT/AgNW-PUA

source/drain structure was laminated with another $15 \Omega \text{ sq}^{-1}$ AgNW-PUA composite electrodes as gate on top of the dielectric layer to complete the device fabrication.

2.2.6 Fabrication of Screen Printed Metal Grid

The highly transparent flexible OLED substrate was fabricated by printing AgNW Ink-M with 1.5X the AgNW concentration using a laser patterned stainless steel stencil, ordered from PCB Stencils with openings consists of 8 parallel lines (50 μm line width, 15 mm line length, and $\sim 900 \mu\text{m}$ pitch), on top of a release glass substrate precoated with a thin layer of silver nanowires at $\sim 160 \text{ ohm/sq}$ sheet resistance. The post-treatment process consists of four wash steps, by soaking in acetone, 1:19 DI water/ethanol solution, 1:1 DI water/ethanol solution, and DI water for five minutes each with a 150°C annealing for 5 minutes in between each wash step. By using 90 μm taper spacers and a top release glass, the polymer precursor of 1:2 SR540/SR499 (Sartomer) with 0.5 wt% photoinitiator was cured under UV irradiation. The resulting AgNW composite was peeled from the release glass and washed with Acetone and IPA prior to OLED fabrication.

A PEDOT:PSS solution containing 5 vol% DMSO and 0.3 wt% Zonyl FS-300 fluorosurfactant was spin-coated on the freestanding electrodes at 4000 rpm and annealed at 130°C for 30 min. Using a vacuum evaporation chamber with base pressure of $\sim 1 \times 10^{-6}$ mbar, the subsequent layers were thermally evaporated at a rate of 0.1-0.3 nm s^{-1} for NPB and BePP₂, 0.01 nm s^{-1} for PO-01 and CsF, and 0.5 nm s^{-1} for aluminum. The CsF/Al contact was fabricated with a 0.13 cm^2 device area. The final device structure is substrate / anode / PEDOT:PSS (40nm) / TAPC (60nm) / PO-01 (0.5nm) / NPB (15nm) / BePP₂ (40nm) / CsF (1nm) / aluminum (80nm).

2.2.7 Characterization Methods

The stretching tests and cyclic strain tests were performed on a motorized linear stage with built-in controller (Zaber Technologies Inc.). A Keithley 2000 digital multimeter was used to monitor the resistance change. Strain and resistance data were recorded with a custom-made LabView code. Transistor electrical characterization was performed with two Keithley 2400 source meter. The measurement sequences were controlled by a custom-made LabView code. All the transistor measurements were tested under ambient atmospheric conditions. The thickness of the screen printed AgNW patterns was measured by a Dektak profilometer. Rheological behavior of the formulated inks was probed using an AR2000 rheometer (TA Instruments) with a 20 mm cone-plate system with 2° cone angle and 57 μm gap. All measurements were probed at room temperature (25 °C). A preconditioning step at a shear rate of 0.1 s^{-1} for 15s was applied before each test. The steady state flow step test was performed to measure the shear viscosity of the inks at shear rates of 0.1-1000 s^{-1} , and the peak hold step test was performed with constant shear rates in three intervals (0.1 s^{-1} shear rate for 30 s, 200 s^{-1} for 30 s, and 0.1 s^{-1} for 200 s.) to simulate the screen printing process. The stress sweep step test was performed with oscillation stress of 1-1000 Pa at a frequency of 1 Hz. Electrical measurements for the WOLED were carried out using a Keithley 2400 source meter and a calibrated silicon photodetector by sweeping the applied voltage from 0 to 6 V in a nitrogen-filled glovebox.

2.3 Results and Discussion

2.3.1 Rheological Behavior of the AgNW Screen-Printing Ink

Conductive screen printing inks generally contain three parts: conductive nano- or micro-particles, organic binder/additive, and solvent.^[57] Conductivity of the printed ink traces depends on the dispersion, specific surface area, and loading density of the conductive particles.^[57] The mixture of the organic binder/additive and solvent promotes wetting of the particles, dispersion stability, and film formation of the printed ink traces. It also allows for adjustment of the ink's rheological behavior suitable for screen printing. To formulate the AgNW conductive ink, AgNWs with a length-to-diameter aspect ratio of 500 were used as the conductive material in this work to form a percolation network at low loading density. Distilled water was selected as solvent due to its environmental friendliness and low cost. A mixture of (hydroxypropyl) methyl cellulose, fluorosurfactant (Zonyl FC-300), and an antifoaming agent (Defoamer MO-2170 from BASF) was employed as the organic binder/additives. (Hydroxypropyl) methyl cellulose, a water-soluble viscoelastic polymer widely used as an emulsifier, thickening and suspending agent, was chosen and used as a rheological agent to provide thixotropic behavior for the screen-printing inks. It also functioned as a dispersive agent to form a good dispersion of AgNW and provide dispersion stability: the hydroxy groups in (hydroxypropyl) methyl cellulose can form strong bonding with the surface of the AgNWs (**Figure 2.1a**). Zonyl FS-300, a nonionic and water-soluble fluorosurfactant, decreases the surface tension of the water-based ink and promotes substrate wettability during printing (Figure 2.1a). Defoamer MO-2170 provides efficient defoaming performance in aqueous printing inks and help prevent foam formation during mechanical agitation.^[57] In a typical formulation, distilled water, propylene glycol, (hydroxypropyl)methyl cellulose, fluorosurfactant and antifoaming agent were mixed at the

weight ratio of 5 : 5 : 1 : 0.002 : 0.01, and sonicated for 2 h to make the additive solution. Next, a AgNW solution (1 wt% in isopropanol), distilled water and the additive solution were mixed at the weight ratio of 4 : 4 : 1 using a vortex mixer at 1,000 rpm for 1h. Volatile solvents in the mixture were removed via vacuum rotary evaporation. A small amount of water was subsequently added back to the dried mixture to make the screen printing inks with the AgNW solid contents calculated to be 6.0wt% (AgNW Ink-L), 6.6 wt% (AgNW Ink-M), and 7.3 wt% (AgNW Ink-H). The inks were agitated strongly using a stir bar at 1,000 rpm for 1 h to obtain the final stable AgNW inks (see photograph in Figure 2.1a).

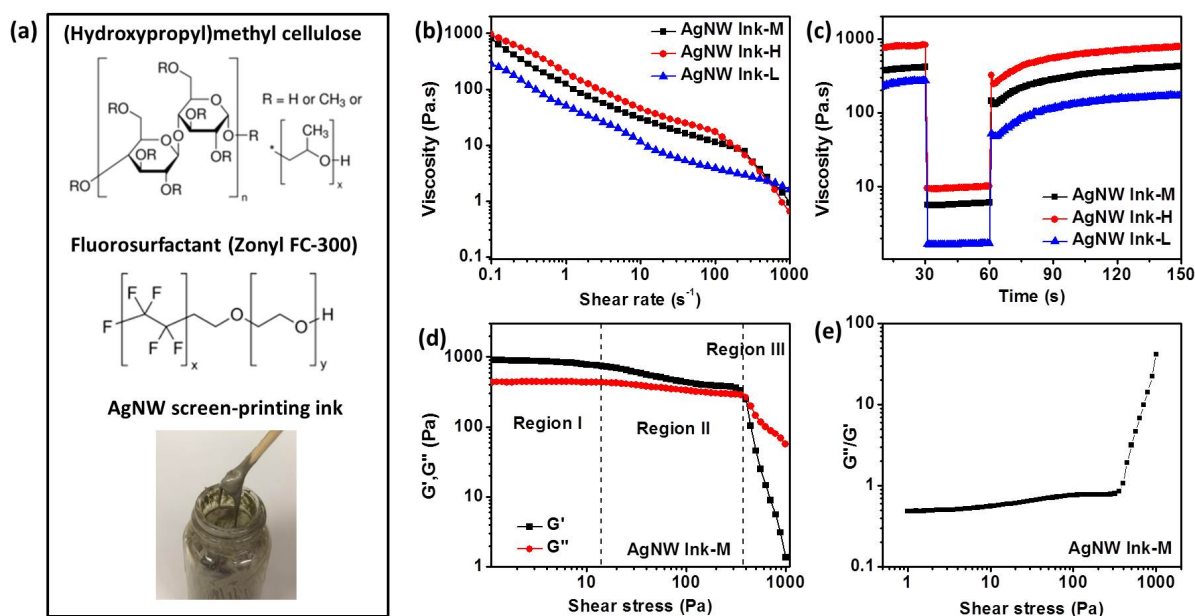


Figure 2.1. a) Molecular structures of (hydroxypropyl)methyl cellulose and Zonyl FC-300, and photograph of the as-prepared AgNW Ink-M. b) Viscosity as a function of shear rate for the AgNW inks. c) Rheological behavior of the inks during screen printing. d-e) Oscillatory rheological test for AgNW Ink-M: Variation of G' and G'' with shear stress, and G''/G' ratio as a function of shear stress.

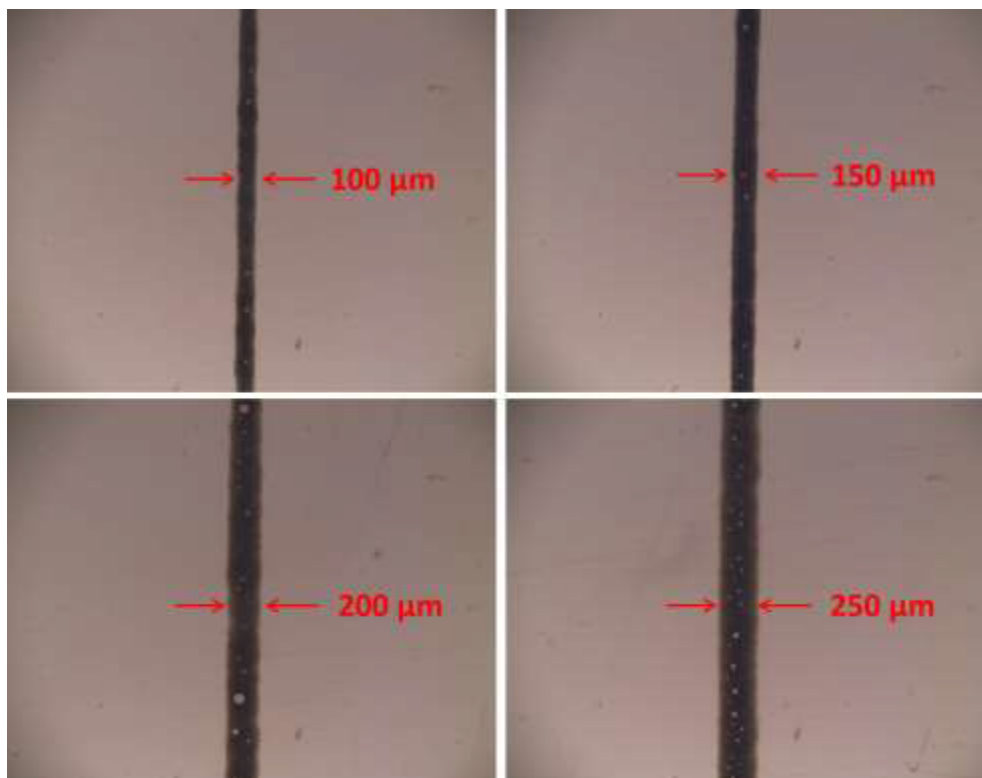


Figure 2.2. Various AgNW lines screen printed from AgNW Ink-H. Pores are clearly seen in the printed lines.

Table 2.1. Viscosity of various AgNW inks at different shear rates corresponding to different printing process steps.

	0.1 s ⁻¹ @ 20 s	200 s ⁻¹ @ 50 s	0.1 s ⁻¹ @ 80 s	Recovery @ 80 s	0.1 s ⁻¹ @ 110 s	Recovery @ 110 s
AgNW Ink-L (6.0 wt%)	262.3Pa.s	1.689 Pa.s	92.11 Pa.s	35.1%	144.9 Pa.s	55.2 %
AgNW Ink-M (6.6 wt%)	405.8Pa.s	5.925 Pa.s	241.6 Pa.s	59.4%	349.0 Pa.s	85.9%
AgNW Ink-H (7.3 wt%)	805.3Pa.s	9.814 Pa.s	471.4 Pa.s	58.5%	650.2 Pa.s	80.1%

The rheological behavior of the AgNW inks was first investigated using a cone-plate rheometer to determine how the AgNW solid content affects the ink properties. The measured viscosity at different shear rates from the steady state flow step (SSFS) test shown in **Figure 2.1b** shows that all three inks displayed a shear thinning thixotropic behavior: the viscosity of the inks decreased as the shear rate increased. Also, the AgNW inks with higher solid contents exhibited higher viscosity at the same shear rate. For example, the viscosities at shear rate of 1 s^{-1} for the AgNW Ink-L, AgNW Ink-M, and AgNW Ink-H are 50.73, 124.2, and 201.0 Pa, respectively. Next, the rheological behavior of the inks during screen printing was further studied from a peak hold step (PHS) test consisting of holding the sample at different shear rates in three intervals (data shown in **Figure 2.1c** and **Table 2.1**). The shear rate was kept at 0.1 s^{-1} for 30 seconds in the first interval, then increased to 200 s^{-1} and held for 30 seconds in the second interval to simulate the squeeze stroke, and finally decreased to 0.1 s^{-1} and held for an additional 200 seconds in the third interval to observe the viscosity recovery.

The AgNW Ink-L had the lowest viscosity of $262.3 \text{ Pa}\cdot\text{s}$ at 0.1 s^{-1} at the time of 20 s, and only 35.1% and 55.2 % of initial values were recovered in 10 s (at the time of 80 s) and 50 s (at the time of 110 s) after the shear rate reduced from 200 s^{-1} to 0.1 s^{-1} . When the squeegee stroke the ink, the viscosity would decrease considerably, leading the ink to flow through the stencil mesh. Nevertheless, low viscosity was inclined to enhance the line definition as indicated by previously published works.^[57] In contrast, the AgNW Ink-H was very viscous, and its viscosity decreased from $805.3 \text{ Pa}\cdot\text{s}$ to $9.814 \text{ Pa}\cdot\text{s}$ after shearing at 200 s^{-1} . Then, the viscosity recovered very quickly to as high as $471.4 \text{ Pa}\cdot\text{s}$ only in 10 s (at the time of 80 s) after reducing the shear rate in the third interval. In this case, the leveling of the ink after printing may not be completed, thus leading to formation of pores, which were clearly seen in the printed patterns using AgNW Ink-H

(**Figure 2.2**). Among all these three inks, the AgNW Ink-M exhibited the most appropriate viscosity and rheological behavior for screen printing. After the shear rate was reduced from 200 s^{-1} to 0.1 s^{-1} , the viscosity of AgNW Ink-M gradually recovered to 241.6 Pa·s and 349.0 Pa·s in 10 s (at the time of 80 s) and 50 s (at the time of 110 s). This recovery time and viscosity allow for leveling of the ink and uniform line formation. Moreover, the recovery of the viscosity for the AgNW Ink-M at the time of 110 s was higher than 80%, which is an indication of good elasticity of the ink.^[64] Generally, the viscosity for the typical inks based on silver particles/flakes, even when formulated with very high solid contents of > 60 wt%, can hardly exceed 70% recovery.^[57,64] In comparison, the AgNW Ink-M has a percentage of recovery over 80% even though the AgNW solid content is only 6.6 wt%. This difference in recovery in viscosity is believed to result from the much larger aspect ratio of AgNW compared to silver particles/flakes which allows for a higher weight percentage of the water-soluble viscoelastic polymer in the formulation.

Oscillatory rheological measurement was also carried out for the AgNW Ink-M to further characterize the visco-elastic effect of the ink in a stress sweep step (SSS) test. The curves of the variation of “storage modulus” G' (elastic component) and “loss modulus” G'' (viscous component) for AgNW Ink-M as a function of shear stress are presented in **Figure 1d** and are divided into three regions.^[57,64,65] **Figure 2.1e** illustrates the variation of $\tan \delta$ (G''/G') as a function of shear stress. Region I corresponds to the linear visco-elastic (LVE) region and is defined as the maximum deformation that can be applied to the ink without destroying its structure.^[65] In this region, the AgNWs contact with each other to form a dense network structure and can be recovered elastically to any applied stress or strain. Thus, the structure of the materials in the ink is not damaged and not dependent on shear stress in Region I.^[65] The ratio of

liquid-like to solid-like behavior (G''/G') within the LVE region is calculated to be ~ 0.49 (Figure 2.1e). Next, in Region II, G' and G'' decreased gradually with increasing shear stress, while the value of G' maintained higher than that of G'' . This region was related to the beginning of the weakening and gradual breakdown of the AgNW ink structure; although the ink still has an elastic-dominated behavior ($G' > G''$), the ink exhibited a more liquid-like behavior as shear stress increased.^[65] Region III starts at the shear stress when the storage modulus is equal to the loss modulus ($G'' = G'$), and extends to the higher shear stresses when G'' became higher than G' and the ink behavior crossed over from solid-like to liquid-like behavior.^[57,66] The cross-over point was reached for a modulus equal to ~ 398 Pa. This value of stress at $G' = G''$ is comparable with the silver flake-based ink which has much higher solid contents ($>60\%$).^[57,65,66] As described above, the larger aspect ratio and unique network structure of AgNWs play a critical role to contribute in the rheological behavior of the AgNW ink.

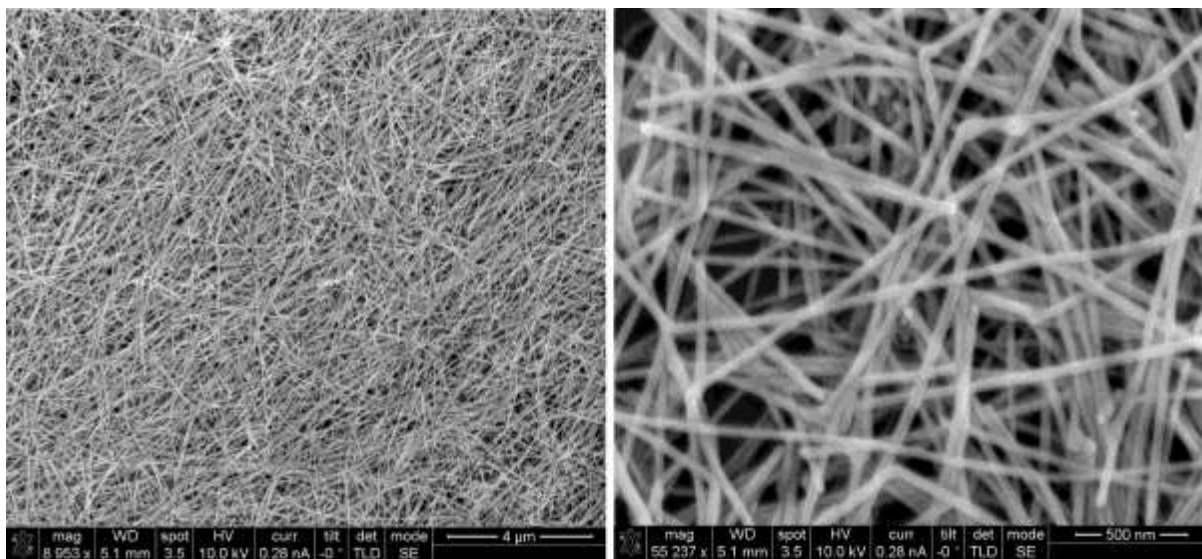


Figure 2.3. Top-view SEM images of screen-printed AgNW patterns.

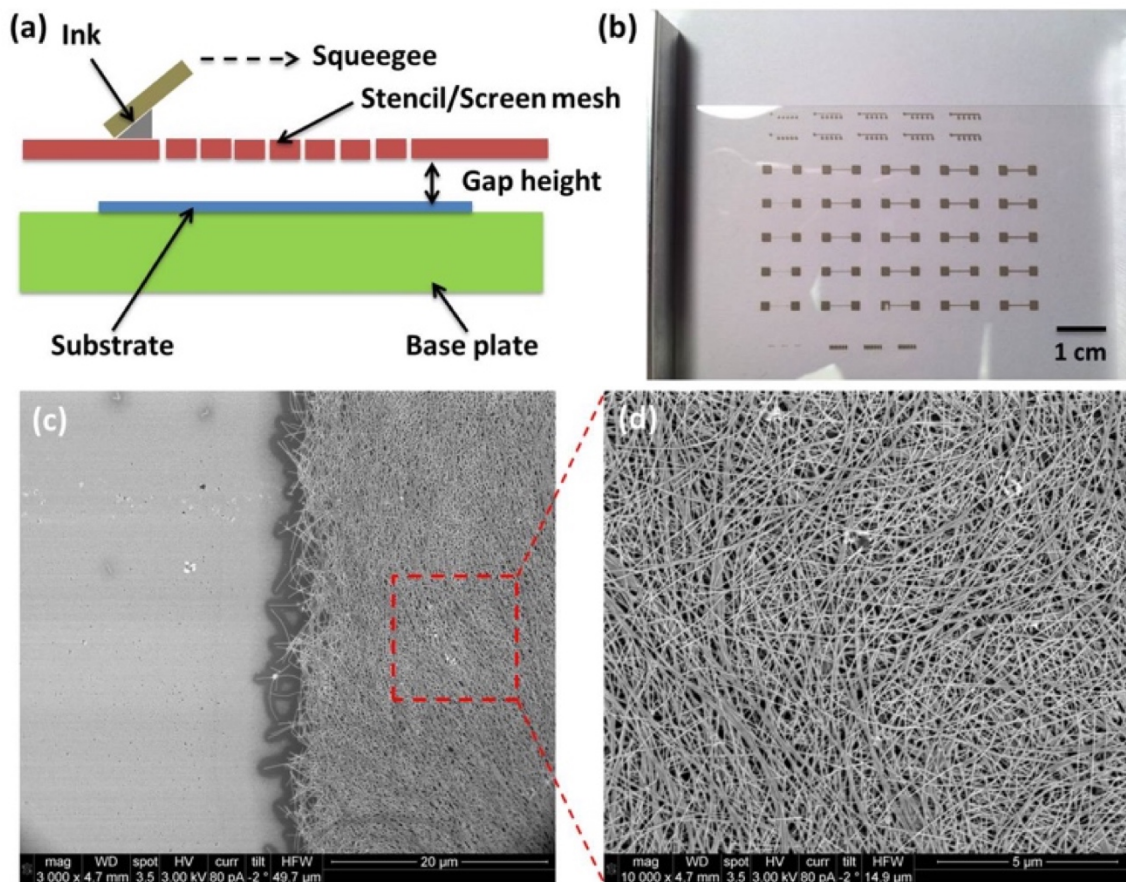


Figure 2.4. a) Cross-sectional illustration of screen printing process. b) Optical image of screen printed AgNW patterns on flexible PET substrate. c) SEM image of the edge of the screen-printed AgNW line after post-treatment. d) SEM image showing the dense AgNW network structure in the screen-printed AgNW line.

Figure 2.4a depicts a schematic diagram of the screen printing system and printing process. Sefar precision stainless steel screen mesh (400 mesh count, 0.0007 inch wire diameter, 0.0018 inches mesh opening, standard mesh tension, 22 degrees mesh angel, 0.0008 inch emulsion thickness, emulsion is safe with water) was used to screen print the AgNW inks. All the tests shown below were carried out with the AgNW Ink-M at room temperature. Since the

additives were used in large proportions in the ink, the as-prepared inks and the printed patterns were non-conductive. After screen printing, post treatments of the printed AgNW patterns, including water-washing and thermal annealing, are thus required to wash off the additives and fuse the AgNW junctions in order to recover the conductivity of AgNW networks (detailed in the Experimental Section). The relatively low thermal annealing temperature (150 °C) for the AgNW patterns allows the ink to be formed and post-treated on flexible PET substrate. **Figure 2.4b** shows a photograph of AgNW patterns printed on a flexible PET substrate. The inset scanning electron microscopy (SEM) image in **Figure 2.4c** shows that the edge of the screen-printed AgNW line is fairly smooth, which is essential to the reproducibility and stability of certain electronic devices, such as thin-film transistors (TFT). Moreover, different from the conventional dense and compact structure of screen-printed patterns from silver flake or particles, the screen-printed AgNW pattern exhibits a continuous and dense network/mesh structure (**Figure 2.4d**). The AgNW networks are mostly composed of randomly distributed individual AgNWs with very few bundles of AgNWs and aggregations, indicating a homogeneous dispersion of AgNW in the percolation network (**Figure 2.3** and **Figure 2.4d**).

Optical images and optical microscopic images are shown in **Figure 2.5a** further present printed AgNW lines on PET with various line widths of ~50, 100, 150, 200, and 250 μm , respectively, which were obtained from stencil having the same line openings. All the AgNW lines are printed with sharp edges, and have uniform and well-defined line widths. The printed lines were continuous with no voids, even for the narrowest one at 50 μm width. In addition, patterns of AgNW lines with various spacing were also printed on PET substrate. AgNW lines with different spacing (50, 80, 100, and 120 μm) were obtained using a stencil having the same gap between the openings as shown in **Figure 2.5b**. Very uniform spacing was obtained between

the lines. Thus, the printed resolution of line width and spacing between the lines can achieve as high as 50 μm , which is important for electronic applications. The thickness of the screen-printed AgNW lines as a function of line width is displayed in **Figure 2.5c**. It can be clearly seen that the thickness of the patterns are decreased as the line width decreased (**Figure 2.6**). This is mainly attributed to the structure of the screen mesh and the AgNWs. The parameter of the stencil mesh used in the present work is: 400 mesh count, 0.0007 in. wire diameter (17.78 μm), 0.0018 in. mesh opening (45.72 μm), and 0.0008 in. emulsion thickness (20.32 μm). When considering the wire diameter (17.78 μm) and emulsion thickness (20.32 μm), the actual size of the 50 μm wide mesh openings is much less than 45.72 μm . Some of the openings through the wire grid could even be less than 20 μm (the average length of the AgNWs used in the present work), preventing the AgNWs in the screen-printed inks from going through the stencil mesh to form 50 μm width line patterns on the substrate. As the width of the line patterns increases, the relative ratio of the restricted wire grid openings is reduced, and thus more AgNWs can go through the stencil, resulting in the increase of the printed thickness. The aspect ratio (thickness/width) of the printed lines fluctuated between around 0.003 and 0.004 at random, lacking a correlation between the line width and thickness (**Figure 2.5d**).

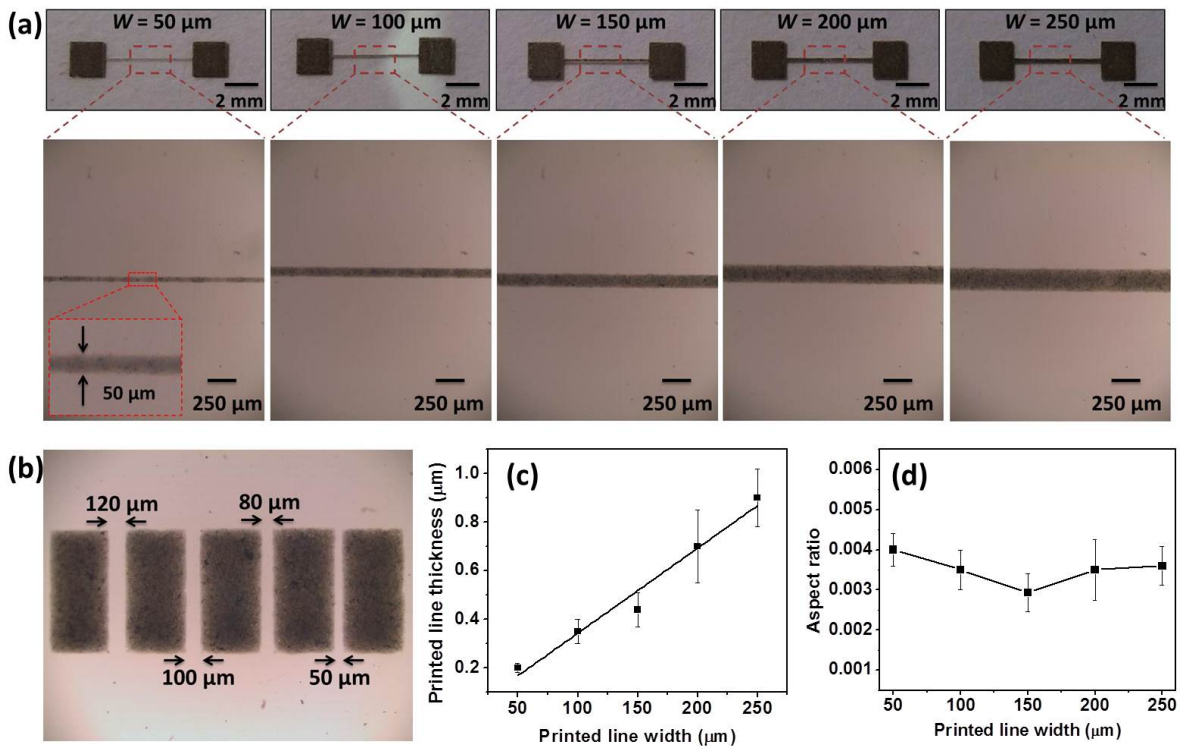


Figure 2.5. a) Optical images and optical microscopic images of AgNW lines printed on PET substrates with line widths of 50 μm , 100 μm , 150 μm , 200 μm , and 250 μm . b) Optical microscopic image of AgNW patterns with spacing of 50 μm , 80 μm , 100 μm , and 120 μm . c) Thickness of screen printed AgNW lines as a function of line width. d) Aspect ratio (thickness/width) of the screen-printed AgNW lines with various line widths. All the patterns are printed with AgNW Ink-M at room temperature.

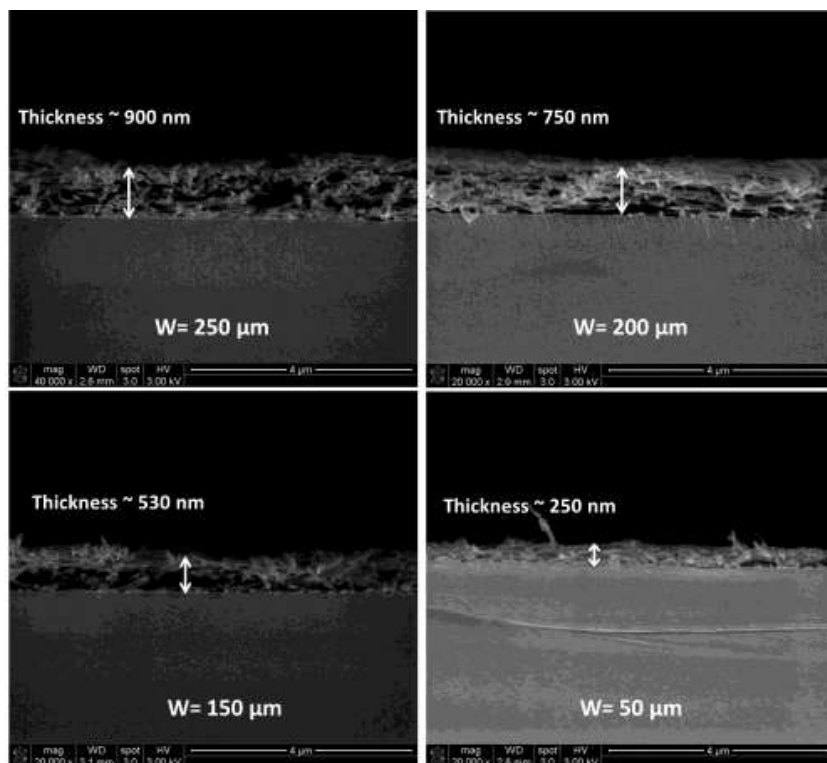


Figure 2.6. Cross-sectional SEM images of the screen-printed AgNW patterns with different widths.

2.3.2 Electrical Properties and Stretchability of the Screen-Printed AgNWs

The electrical properties of screen printed AgNW lines were measured from a screen-printed test pattern as shown in **Figure 2.7a**. The measured resistance of AgNW lines for different length and various line widths was displayed in **Figure 2.7b**. All straight lines showed a correlation factor of higher than 0.995, indicating very good uniformity of the printed lines at various line widths. The average sheet resistance of the AgNW lines was calculated to be 1.05 ± 0.083 , 0.86 ± 0.071 , 0.823 ± 0.043 , 0.77 ± 0.073 , and 0.68 ± 0.08 for line width of 50, 100, 150, 200, and 250 μm , respectively (**Figure 2.7c**). It can be found that the sheet resistance of the AgNW lines declined slightly as printed line width increased. The electrical conductivity was

further calculated following the equation: $\sigma=L/(RWt)$, where σ , L , R , W , and t are the conductivity, line length, measured resistance, line width and line thickness. Accordingly, the average conductivity achieved $4.67 \pm 0.60 \times 10^4$, $3.97 \pm 0.40 \times 10^4$, $2.96 \pm 0.56 \times 10^4$, $1.85 \pm 0.20 \times 10^4$, and $1.64 \pm 0.14 \times 10^4$ S cm⁻¹ for the printed line width of 50, 100, 150, 200, and 250 μm , respectively. It is interesting to note that the electrical conductivity decreased slightly as the printed line width increased (**Figure 2.7d**). It can be seen from Figure 2.6 (Supporting Information) that while the AgNW stacks compactly in the AgNW pattern with line width of 50 μm , some voids are observed in the AgNW patterns with larger line widths and is believed to be the main reason for the decrease in the electrical conductivity of the screen-printed patterns as the line width increases. This void issue is likely caused by the bubbles introduced during the screen-printing process and could be resolved by further optimizing the ratio or contents of the defoaming agent in the AgNW inks. **Table 2.2** compares the electrical conductivity of the screen-printed AgNW lines with a number of reported publications and commercial products concerning screen printing of conductive pastes based on silver particles/flakes post-treated at different conditions.^[42,57-62] It can be seen that the AgNW lines screen printed from AgNW Ink-M exhibit comparable or even higher conductivity than most of the reported or commercial silver inks, and have a relatively low post-annealing/sintering temperature (< 200 °C). It should be pointed out that the solid content of the AgNW Ink-M, ~6.6 wt%, is much lower than that of all the other silver inks based on silver particles/flakes (>60 wt%), indicating a potential for low cost of the AgNW-based ink. This low solid content of AgNW Ink-M but high conductivity of the printed AgNW lines mainly benefited from the large aspect ratio of AgNWs and the post-treatment process to remove the additives after printing. Although silver ink based on silver particles/flakes sintered at high temperature, i.e. > 600 °C, showed better electrical conductivity

than that of AgNW ink, such high sintering temperatures make them hard to be applied on flexible plastic or paper substrates.

Table 2.2. Comparison of electrical conductivity of the present work with various previous research and commercial product concerning screen printed inks.

Solid contents	Substrate	Annealing/Sintering Temperature	Annealing/Sintering Time	Electrical Conductivity (S cm ⁻¹)	Reference
Silver flake 70wt%	LTCC*	875 °C	60 min	3.33×10^5	[57]
Silver nanoparticle 80 wt%	Alumina	450 °C	15 min	2.5×10^5	[58]
Silver flake 70 wt%	Alumina	700 °C	15 min	1.67×10^5	[59]
Silver flake 70 wt%	Ferrite	850 °C	15 min	6.67×10^4	[60]
Silver flake 70 wt%	Paper	160 °C	50 min	5.26×10^4	[61]
Silver flake 60 wt%	Glass	200 °C	60 min	3.03×10^4	[62]
Silver 68wt%		130 °C	4 min	2×10^3	AG-959 Conductive Compounds Inc.
Silver 80 wt%		170 °C	30 min	2.22×10^4	9169 DuPont Inc.
Graphene 80 mg/mL	Polyimide	300 °C	30 min	1.86×10^2	[42]
AgNW6.6 wt%	PET/Glass	150 °C	15 min	4.67×10^4	Present work

*LTCC: Low Temperature Co-Fired Ceramic

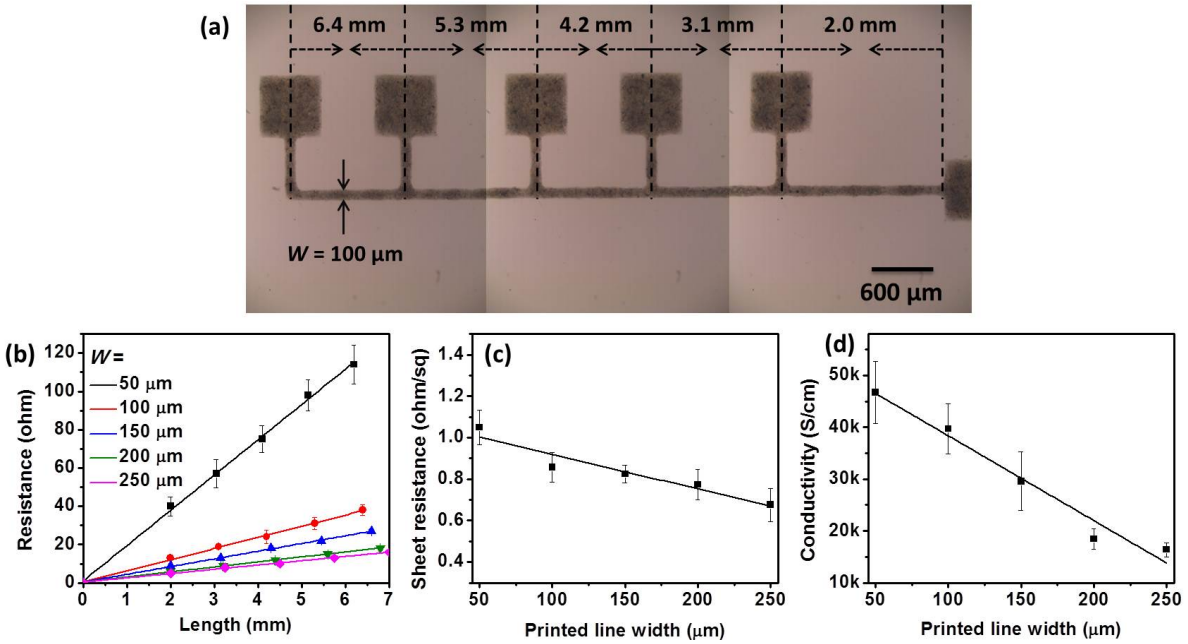


Figure 2.7. a) Optical microscopic image of screen-printed AgNW pattern to measure electrical properties. b) Measured resistance at various lengths and widths. c) Calculated sheet resistance. d) Calculated conductivity. At least 5 samples were tested for each line width.

To further characterize the mechanical compliance of the screen-printed AgNW patterns, an in-situ substrate polymerization and transfer technique, which we have previously reported,^[5,8,31] was employed to fabricate stretchable AgNW-based composite conductors. A urethane acrylate monomer was coated onto the AgNW patterns on a releasing PET/glass substrate. The monomer was cured, and the resulting PUA film was peeled off to transfer the screen-printed AgNW network into the surface layer of the PUA film. The average roughness (R_a) for the conductive surface of the AgNW/PUA composite conductors is lower than 2 nm (as can be seen from the AFM image of **Figure 2.8**). In order to test and study the stretchability of the screen-printed AgNW patterns, conductive patterns containing two contact pads at the end of lines with dimensions of 5 mm in length and various width (50, 100, 150, 200, and 250 μm) were

designed as shown in the inset image of **Figure 2.9a** and Figure 2.5(a). All AgNW/PUA composite conductors were mounted on a motorized linear stage, leaving the 5 mm length (gauge length) free to deform. All samples were stretched at 1 mm/s along the length direction, and the resistance was monitored in sync with linear deformation. Figure 2.9a exhibits the resistance change of all AgNW/PUA composite conductors as a function of uniaxial tensile strain up to 70%, which is high enough for most stretchable/wearable electronic applications. Most samples were ruptured at $\approx 80\%$ tensile strain due to the rupture of the PUA polymer matrix. The conductivity of conductors with different line widths all decreased moderately with the application of tensile strain, which is considered to be caused by the loss of interconnection between the AgNW under strain. The 70% strain resulted in a reduction of conductivity to 8002, 7478, 10864, 14234, and 10064 S cm⁻¹ for the AgNW/PUA composite conductors with line width of 250, 200, 150, 100, and 50 μm , respectively. However, not only the initial conductivity values, but also the conductivity values under the high strain were both higher than all other reported intrinsically stretchable conductors based on various conductive components,^[46–49,67,68] as shown in **Table 2.3**. This higher conductivity should be attributed to the large aspect ratio of AgNWs and the homogeneous dispersion of AgNWs in the percolation network.^[47]

Moreover, the difference in stretchability among the AgNW/PUA composite conductors with various line widths is also recorded in cyclic deformation. **Figure 2.9b-f** display the normalized resistance (R/R_0 , the ratio of the instantaneous resistance at a specific tensile strain to the initial resistance at zero strain) for screen-printed AgNW/PUA composite conductors with various line widths during 1,000 cycles of tensile stretching and releasing between 0 and 30% strains. The peak of resistance change (resistance value at 30% strain) for the AgNW/PUA composite conductors with line width of 50, 100, 150, 200, and 250 μm increases gradually from

about 7.1 to 28.2, 5.3 to 15.2, 4.5 to 13.8, 4.4 to 10.7, and 3.5 to 6.8 times its initial value, respectively. It can be seen that conductive lines with larger width value show smaller change of resistance after 1000 cycles of deformation.

Table 2.3. Comparison of electrical conductivity and stretchability of the present work with various previous research concerning intrinsically stretchable conductors.

Conductive components	Process	Conductivity at 0% strain (S cm ⁻¹)	Conductivity at 70% strain (S cm ⁻¹)	Reference
Silver flake Silver-CNThybrid	Printable	5,710	~800	[48]
Silver nanoparticle	Printable	5,450	~3,700	[49]
Silver flake	Printable	3,570	~1,200	[47]
Silver particle Silver-CNT hybrid	Wet spinning	~6,000	~260	[67]
Gold nanoparticle	Layer-by-layer deposition	11,000	~5,000	[68]
SWCNTs	Printable	9.7	9.7	[46]
Silver flake	Printable	738	~400	[50]
AgNWs	Printable	16,500*	8,002*	Present work
AgNWs	Printable	46,000**	10,064**	Present work

*Printed line width of 250 μm

**Printed line width of 50 μm

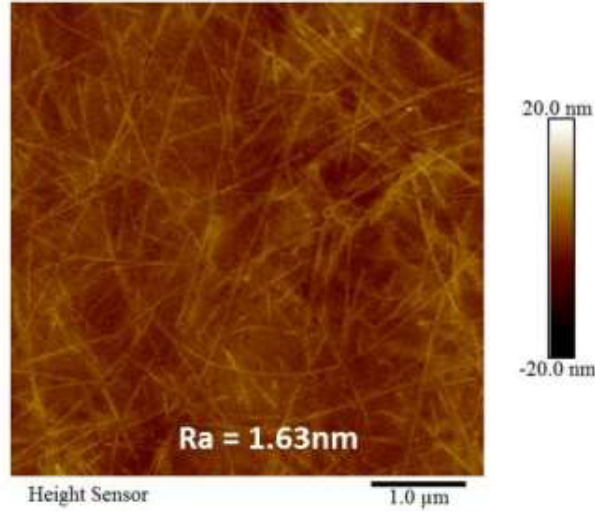


Figure 2.8. AFM image of the conductive surface of AgNW/PUA composite electrodes.

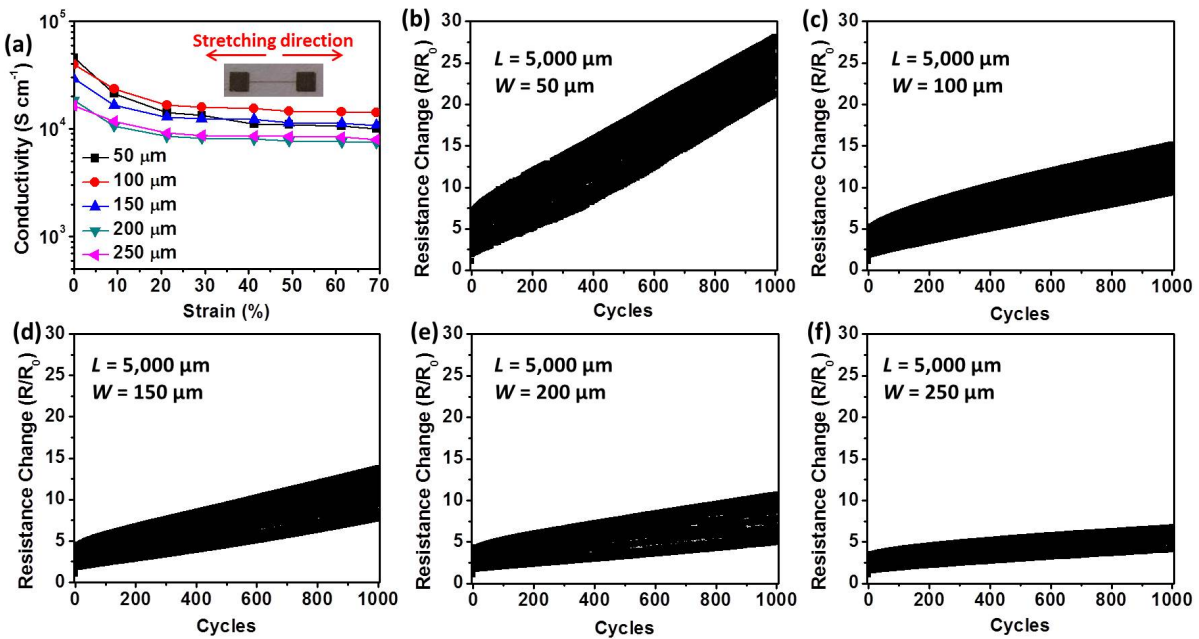


Figure 2.9. (a) Conductivity change of screen-printed AgNW/PUA composite as a function of tensile strain. Inset image shows a printed AgNW pattern. Normalized transient resistance of screen-printed AgNW/PUA composite conductors with line widths of (b) 50 μm , (c) 100 μm , (d) 150 μm , (e) 200 μm , and (f) 250 μm during 1,000 cycles of tensile stretching between 0 and 30% strains. All line lengths are 5 mm, strain rate is 1 mm/s, and stretching direction is along the length direction.

2.3.3: Device Performance of the Fully Printed TFT Array

To demonstrate the application potential of the screen-printed AgNW/PUA composite conductors for stretchable/wearable electronics, a fully-printed and stretchable/wearable TFT array was thus fabricated and evaluated. Stretchable/wearable TFT is the key component behind a variety of stretchable and wearable electronic devices. In addition, fully-printed fabrication process has been considered to be a viable solution to enable the large scale and low cost construction of stretchable/wearable electronics.^[35] TFT array was fabricated using screen-printed AgNW conductors as source/drain electrodes, which were then embedded into the surface layer of the PUA matrix as described above to make AgNW/PUA composite source/drain conductors. **Figure 2.10a** shows an optical microscopic image of a pair of screen-printed AgNW/PUA composite source/drain electrodes with channel length of 50 μm and channel width of 1,000 μm . Examination of the optical microscopic images of the 60 source/drain electrodes show that only one pair of screen-printed AgNW source/drain was failed due to overlap during the screen printing process, meaning a yield of 98.3%. The main steps for fabricating the fully printed 10×6 TFT array, as depicted in **Figure 2.11** and detailed in the Experimental section, followed the approach in our previously reported work.^[31] **Figure 2.10b** shows a schematic illustration of the configuration of a fully printed TFT, in which a pair of screen-printed AgNW electrodes was used as source/drain, semiconductive SWCNT was drop-printed as channel materials, a stretchable polyurethane-poly(ethylene oxide) copolymer was spin-printed as dielectric, and another AgNW/PUA composite electrode was laminated as top gate. **Figure 2.10c** shows a resulting fully printed 10×6 TFT array, which can be worn on a finger as wearable electronics (**Figure 2.10d**).

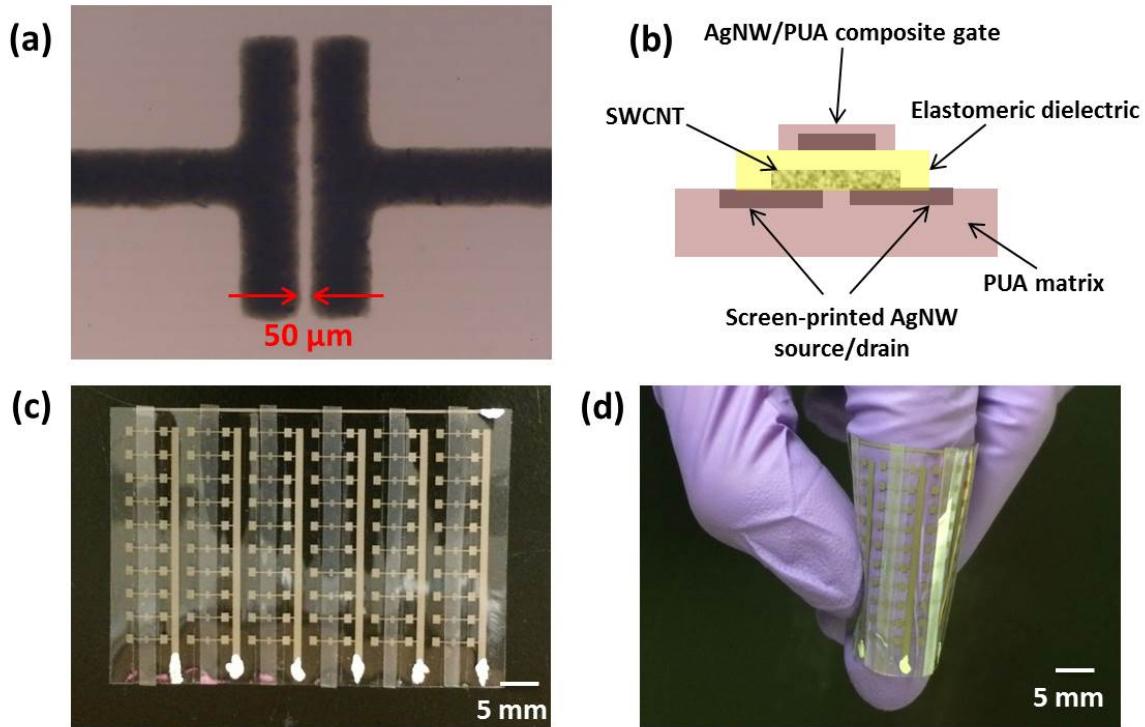


Figure 2.10. a) Optical microscopic image of screen-printed AgNW source/drain electrodes with channel length of 50 μm and channel width of 1,000 μm . b) Schematic illustration of the configuration of a fully printed TFT based on screen-printed AgNW source/drain electrodes. c) Picture of a fully-printed stretchable 10 \times 6TFT array. d) Picture of a fully-printed stretchable 10 \times 6TFT array contorted around a finger.

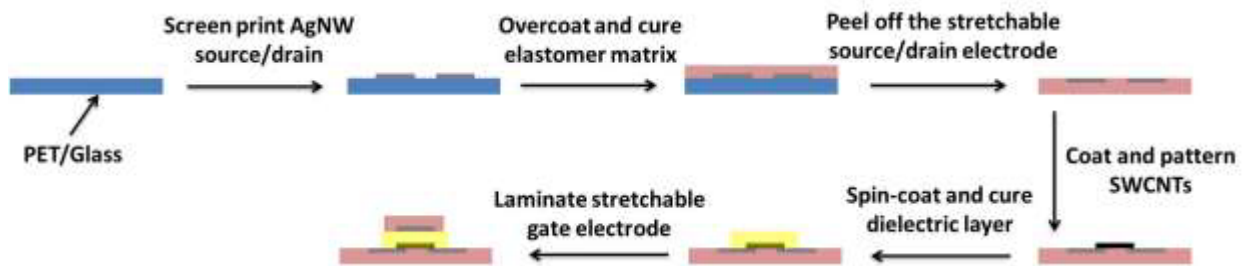


Figure 2.11. Schematic illustration of the fabrication process of the fully-printed and stretchable/wearable TFT array.

Electrical properties of one device in the fully-printed and stretchable/wearable TFT array are shown in **Figure 2.12a-b**. All devices were characterized in air at room temperature. A family of output curves appears to be linear at low applied drain voltages with gate voltage stepped from 0 to -5 V in 1 V step. Current saturation at high drain voltages due to pinch-off can also be clearly seen. From the transfer curves, a peak ON current (I_{ON}) value of $\sim 75 \mu\text{A}$ at $V_D = -2.0 \text{ V}$, corresponding to $75 \mu\text{A}/\text{mm}$ as normalized by the channel width, was obtained. Well-defined ON-state and OFF-state currents were observed with an $I_{ON/OFF}$ of $\sim 1,000$ at $V_D = -2.0 \text{ V}$. The relative low $I_{ON/OFF}$ is attributed to the high density of nanotubes ($\sim 30 \text{ tubes } \mu\text{m}^{-1}$) coated on the channel.^[31] Higher nanotube density is suggested to increase the probability of percolative transport through the metallic nanotubes, causing the decrease of $I_{ON/OFF}$.^[69,70] Furthermore, based on the parallel-plate capacitor model, the mobility of the device was calculated employing the following equation: $\mu = (dI_D/dV_G)(L/V_D C_i W)$, where μ is the device mobility, I_D the drain current, V_G gate voltage, L channel length, W channel width, and C_i specific capacitance of the elastomeric dielectric, which was measured from parallel plate test structures with an average value of $\sim 16.7 \text{ nF}/\text{cm}^2$ at 12 Hz with thickness being $\sim 1.1 \mu\text{m}$.^[31] The device mobility was extracted from the transfer curve to be $35.5 \text{ cm}^2 \text{ V}^{-1} \text{ s}^{-1}$.

The uniformity and yield of the fabricated TFT devices for the fully printed 10×6 TFT array was then investigated. 55 devices were functional from the 60 total devices fabricated in the array, giving a yield of 91.7%. Five devices were nonfunctional: one was failed due to the source/drain overlap happening during screen printing process, and the other four were short because of the gate leakage through pinholes/defects in the insulator which are introduced during the TFT array building process. It is believed that further optimizing the screen printing process and moving the TFT fabrication process in a cleanroom environment could improve the yield.

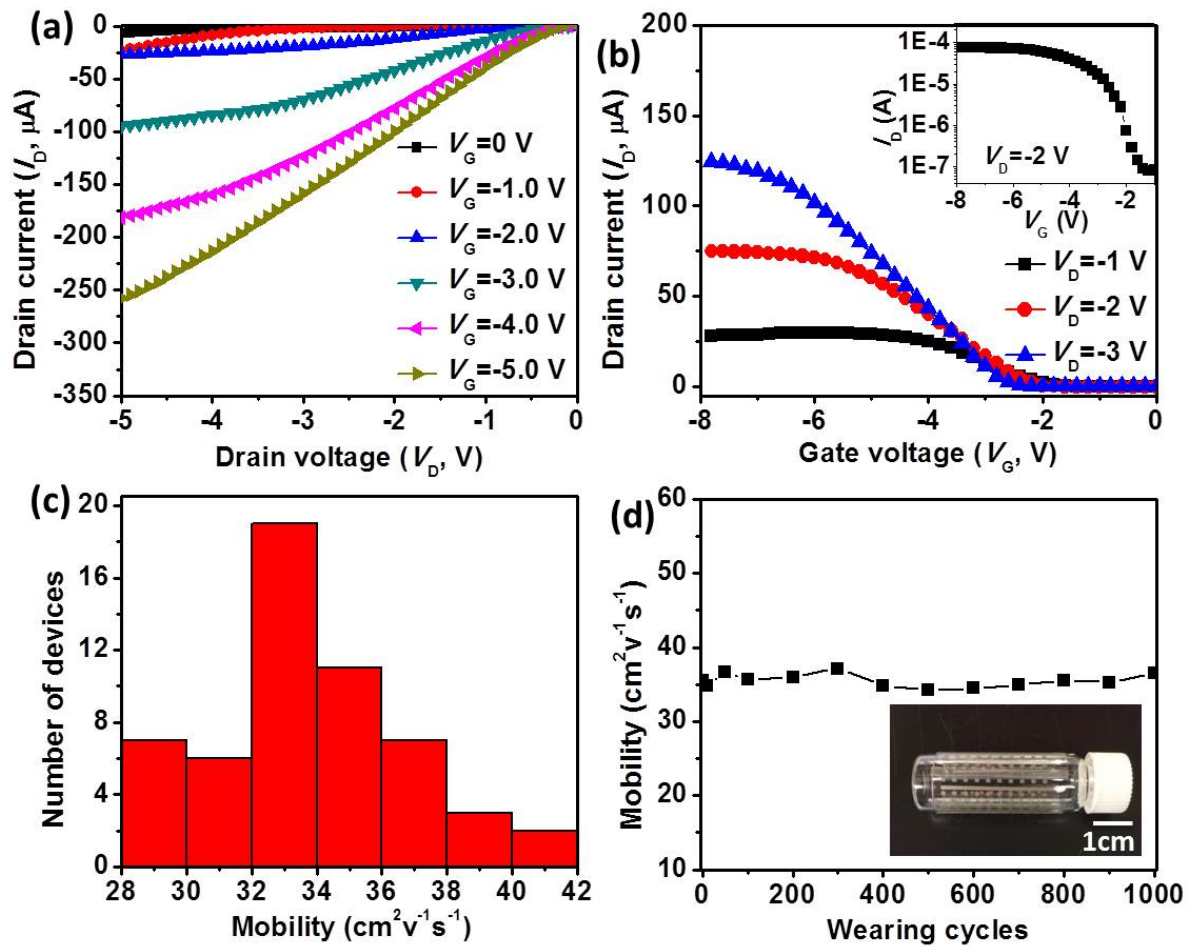


Figure 2.12. a) Output (I_D – V_D) characteristics of a typical TFT with V_G from 0 to -5V in 1.0 V step. b) Transfer(I_D – V_G) characteristics of the same device with V_D from -1.0 to -3.0 in 1.0 V step. Inset, I_D – V_G curve at V_D -2.0V on a logarithmic scale. c) Histograms of TFTs in the 10×6 array showing the statistical distribution of mobility. d) Mobility change of one TFT in the fully printed array during 1,000 repeated cycles of wearing on and peeling off a glass vial with radius of 5 mm.

Figures 2.12c presents the histograms of the statistical variations for these 55 devices in mobility, which are all extracted as described above at $V_D = -2.0$ V, and the average of mobility is $33.8 \pm 3.7 \text{ cm}^2 \text{ V}^{-1} \text{ s}^{-1}$. The variation, around 10%, is small compared to the previous works in

terms of printed transistor array,^[31,35,71] thanks to the good uniformity of channel length and width in the TFT array obtained from the screen-printed AgNW inks. To further investigate the electrical properties of the fully printed TFT array as wearable devices, the transfer characteristics were further measured by subjecting the TFT array to 1,000 cycles of continuous wearing on-peeling off a glass vial with radius of 5 mm (**Figure 2.12d**). The mobility of a random TFT in the array remained highly stable and did not show a clear declining trend during the deformation cycles, revealing good wearability of the fully printed TFT array.

2.3.4 Device Performance of OLEDs on a Highly Transparent Flexible Substrate

The innate physical properties of AgNW networks contains a trade-off between conductivity and transmittance as reported in our prior work.^[5] The transmittance of the silver nanowire networks with 25, 15, and 10 ohm sq⁻¹ sheet resistance are roughly 85, 82, and 78% respectively. Over the years, screen printing techniques have been investigated in solar cell technologies to fabricate low resistance current collecting grids to more efficiently conduct the current through large area solar cells.^[56,72-74] Comparatively, the overall sheet resistance of the silver nanowire based OLED substrates should also be reduced to eliminate reduce device performances for large area substrates caused by voltage drop. This work focuses on applying the AgNW based screen printing ink technology to print dense layers of silver nanowires in ≤ 50 μm wide lines (with dimensions that is hardly noticeable by the naked human eyes) to form flexible, highly transparent, low resistance conductive networks.

To achieve a lower resistance of the printed AgNW pattern, a different formulation of the screen printing paste was developed containing 1.5X the concentration of AgNWs and an additional 25 μL of 5 wt% PVP in IPA per 1 mL of AgNWs to help with AgNW dispersion

within the paste. As shown in **Figure 2.13a**, the printed pattern (after post-treatment) used to measure electrical properties is darker than the patterns shown in Figure 2.7(a) as a result of a denser, thicker layer of the printed silver nanowires. As explained previously, the Sefar stencil has the openings through the wire grid that might be less than 20 μm and prevents AgNWs from going through the stencil mesh to effectively print 50 μm line patterns. To overcome this limitation, a stainless steel stencil made with laser ablated full openings was used which allowed for the printing of lines with widths of 35, 40, 45, and 50 μm . The average thicknesses of the printed lines measured using a profilometer are 278, 303, 330, and 350 μm for lines with widths of 35, 40, 45, and 50 μm respectively.

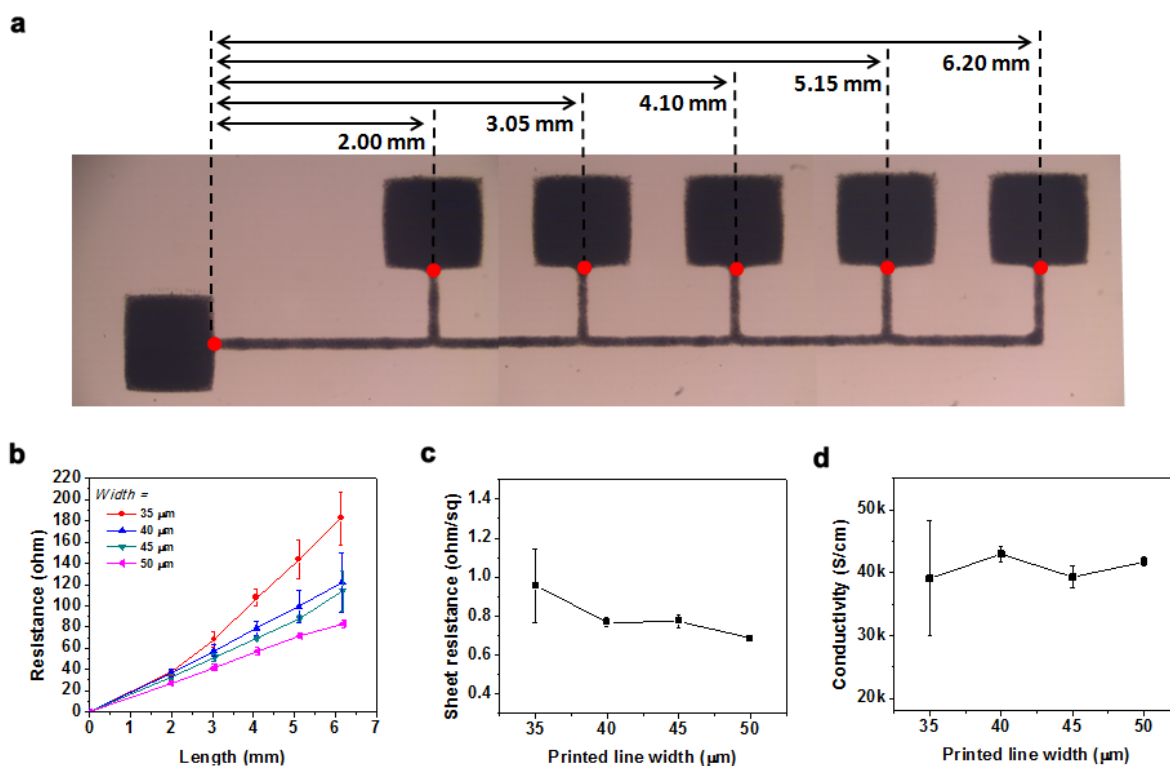


Figure 2.13. a) Optical image of screen-printed AgNW pattern to measure electrical properties with different line width. b) Measured resistance at various lengths and widths. c) Calculated sheet resistance. d) Calculated conductivity. At least 5 samples were tested for each line width.

The resistance, sheet resistance, and conductivity of the printed lines are shown in **Figure 2.13b-d**. In comparison with the lines with 50 μm width printed using the Sefar stencil, the resistance of the 50 μm width printed lines using the stainless steel stencil was reduced from 114 ohm to 82 ohm at 6.2 mm length, and the average sheet resistance was reduced from 1.05 ohm sq^{-1} to 0.68 ohm sq^{-1} . Note that although 1.5X the concentration of the silver nanowires has shown a positive trend in printing thicker silver nanowire patterns, patterns printed with an even higher concentration of silver nanowires showed diminutive behaviors as the rheological behavior of the paste changed dramatically and prevents the AgNWs from printing continuous lines with uniform and straight edges. The overall conductivity of these printed lines is comparable to the previous results at $\sim 40\text{-}42\text{ k S cm}^{-1}$, which indicates that the modified post-treatment could successfully remove the organic binder/additives without disturbing the AgNW networks although a thicker layer of the paste was printed. Also, note that the results from the printed patterns with 35 μm width contains a large variation in resistance/conductivity; this is believed to be caused by the limitation of printing the nanowires used in this study which has an average length between 20-30 μm , which causes inconsistent printing with 35 μm wide opening. As such, printing with stencil openings smaller than 35 μm was not studied.

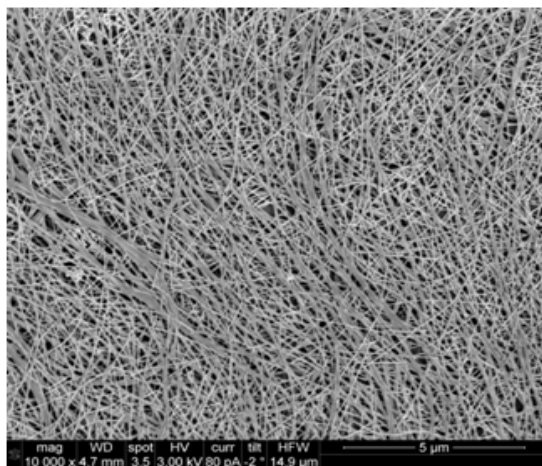


Figure 2.14. Top-view SEM images of screen-printed AgNWs.

To fabricate the OLED substrate, a release glass was precoated with a thin layer of silver nanowires that has a sheet resistance of 160 ohm sq^{-1} and $\geq 98\%$ transmittance. The purpose of this layer is to conduct charges horizontally between the printed gridlines. The screen printed pattern consists of 8 parallel lines ($50 \text{ }\mu\text{m}$ line width, 15 mm line length, and $\sim 900 \text{ }\mu\text{m}$ pitch). These dimensions were chosen because the $50 \text{ }\mu\text{m}$ line width has the lowest sheet resistance and the $\sim 900 \text{ }\mu\text{m}$ pitch between the lines can yield a theoretical transmittance of $\sim 90\%$ transmittance, assuming no light can pass through the areas containing the screen printed nanowires. The resulting total transmittance of these nanowire networks (thin layer + screen printed) is approximately 88-89% transmittance, and the resulting substrates have an average of $\sim 4.8 \text{ ohm sq}^{-1}$ sheet resistance, which is a significant improvement in comparison to a uniform layer of AgNW network with 10 ohm sq^{-1} sheet resistance at 78% transmittance.^[5] By transferring the AgNWs with the SR540+SR499 polymer, AgNWs are embedding within the polymer matrix, and the average surface roughness is 0.879 nm for areas with low density of AgNWs and 1.61 nm for areas with high density of AgNWs (**Figure 2.14** and **2.15**) and satisfies typical surface roughness values that are required for the fabrication of OLEDs by having a $R_a \leq 2.0 \text{ nm}$.

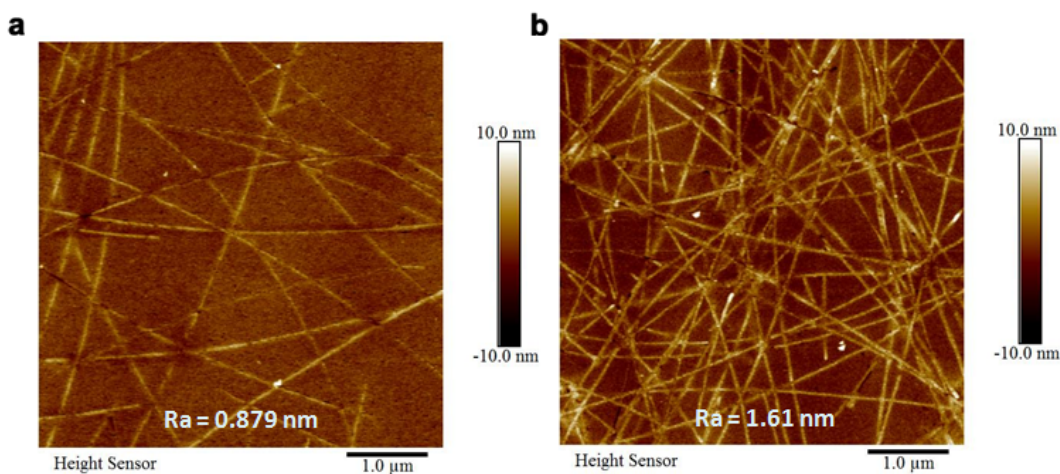


Figure 2.15. AFM image of the conductive surface of AgNW/SR540+SR499 composite electrodes: a) 160 ohm sq^{-1} AgNW area and b) screen printed AgNW area.

WOLEDs were fabricated atop the OLED substrates by overcoating the AgNW surface with a planarization PEDOT:PSS layer and thermally evaporating the subsequent OLED layers using thermal evaporation. As shown in **Figure 2.16a** of a device fabricated on the composite OLED substrate operating at 4V, the OLED substrate is highly transparent in the areas between the screen-printed lines, and the lower density nanowires between the screen-printed lines were able to sufficiently dissipate the charges for uniform light emission. Unlike traditional, brittle metal oxide-based (ITO-based) OLED substrates, a composite substrate made with a conductive film composed of AgNWs is flexible, and the OLEDs fabricated on such substrate can also be bent without causing detrimental damages to the device performance.

Figure 2.16b shows the Luminance-Voltage-Current density (L-V-J) characteristics of WOLED devices fabricated on the highly transparent composite substrates in comparison with ITO control devices. Though the devices fabricated on the composite substrates shows a slightly lower current density at < 4.5 V operating voltage, the luminance at the respective operating voltage is higher than the control devices fabricated on ITO/glass substrates. As a results, the current efficiency (CE), power efficacy (PE), and external quantum efficiency (EQE) show enhancement factors of approximately 1.66, 1.61, and 1.43 respectively, with a CE of 75.4 cd A^{-1} , PE of 74.2 lm W^{-1} , and an EQE of 29.1% for the composite substrate and a CE of 45.5 cd A^{-1} , a PE of 46.1 lm W^{-1} , and an EQE of 20.4% for the ITO/glass control at a luminance of 1000 cd m^{-2} (**Figure 2.16c**). The enhancement of the CE, PE, and EQE of the composite substrate is partly due to the use of AgNWs as an ITO replacement that enhances light outcoupling by removing the high refractive index layer of ITO ($n \approx 1.90$) which induces waveguided light within the device due to internal light reflection. More importantly, this method shows the application potential of integrating the low resistance, screen printed silver nanowire grid lines

with lower density, more transparent AgNW films to fabricate high transparent, efficient, and flexible OLED substrates.

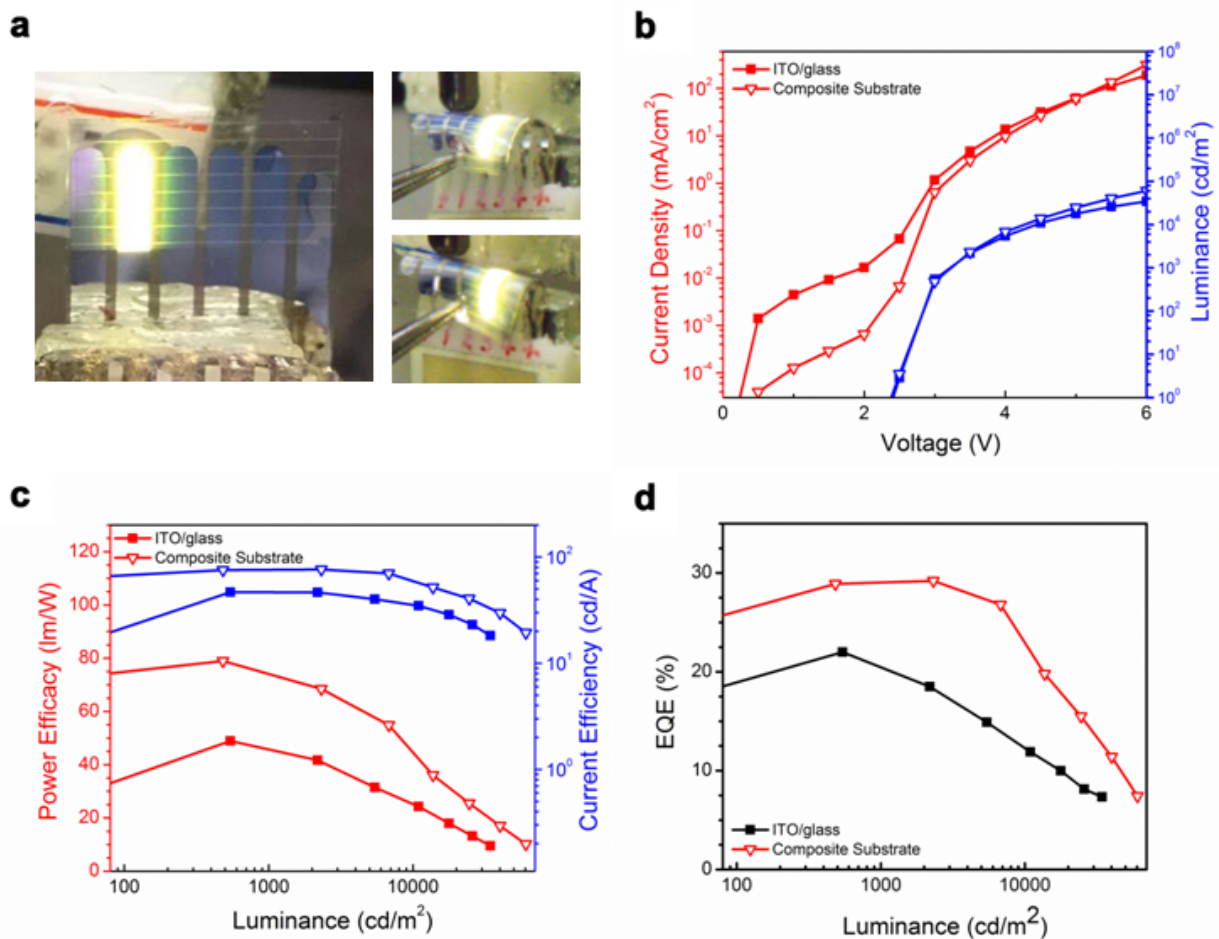


Figure 2.16. a) Photographs of device fabricated on a composite substrate operating at 4 V. Comparison of performance characteristics of WOLED devices with ITO and nanocomposite anodes: b) Current-Voltage-Luminance (J-V-L) characteristics, c) Power efficacy-Luminance-Current Efficiency (PE-L-CE) characteristics, and d) EQE vs Luminance.

2.4 Conclusions

In summary, water-based AgNW inks were developed and screen printed on flexible PET and rigid glass substrates. The AgNW ink, which contains a low solid content of 6.6wt%, had a viscosity as high as 405.8 Pa·s at 0.1 s⁻¹ shear rate and appropriate rheological behavior suitable for screen printing. Uniform and sharp-edged lines with resolution achieving 50 μm were obtained by screen printing the AgNW ink. Moreover, a low thermal annealing temperature of 150 °C was required to post-treat the printed patterns to recover the conductivity to as high as 4.67 × 10⁴ S cm⁻¹. When embedded in the surface layer of the elastomeric PUA, the screen printed AgNW/PUA composite conductor behaves like a rubbery conductor. The retention in conductivity of the composite conductor was up to ~14,000 S cm⁻¹ at 70% tensile strain. The composite conductors were successfully used as stretchable source/drain electrodes to demonstrate a fully-printed and wearable 10 × 6 TFT array that had a yield of 91.7%, an average mobility of 33.8 ± 3.7 cm²V⁻¹s⁻¹, and high stability during 1,000 cycles of wearing on-peeling off a glass tube with 5 mm diameter. These results present a promising approach to realizing stretchable/wearable electronics through a fully printing process.

Alternatively, the AgNW-based screen printing ink was modified to print low resistance gridlines for the fabrication of highly transparent OLED substrates. When combined with a thin layer of silver nanowires, the transmittance of the OLED substrates could be as high as 90% with a sheet resistance of approximately 5 ohm sq⁻¹. OLEDs fabricated atop the transferred nanowires have shown an enhancement factor of ~ 1.6X in comparison to rigid conventional ITO/glass substrates and were demonstrated to be physically bent without showing signs of device failure. Furthermore, this work also presents an encouraging potential for future adaptation of patterned silver nanowire patterns for the fabrication of large size (>30 inch) OLED substrates as it has

demonstrated that the implementation of the dense AgNW grid lines with 0.68 ohm sq^{-1} sheet resistance and a thin layer of AgNWs with 160 ohm sq^{-1} sheet resistance could drive an OLED similarly to a uniform layer of AgNWs with 15 ohm sq^{-1} sheet resistance.

Chapter 3

Efficient Light Extraction of OLEDs on a Fully Solution-Processed Flexible Substrate

3.1 Introduction

Since the advent of organic light-emitting diodes (OLEDs), significant effort has been put forth in developing materials with higher electrical and thermal stabilities,^[75–78] transport properties,^[79–81] and luminescence quantum yields.^[82–84] Improvements on these fronts, in conjunction with their unique properties of mechanical deformability, low-power consumption, low temperature fabrication, and excellent color quality, have propelled OLED technology to the forefront of the flat panel display and replacement lighting markets.^[85] As newer technologies surface, breakthroughs in device physics and interfacial properties have allowed OLEDs to reach internal quantum efficiencies close to the theoretical maximum of 100%.^[15,86] However, to date, the external (outcoupling) quantum efficiency (EQE) still lags behind, with typical values on the order of 20~30% (air mode). One significant contributor to this discrepancy is the difference in refractive indices between air ($n = 1$), glass substrates ($n \approx$

1.5), organic layers ($n \approx 1.7-1.8$), and indium tin oxide (ITO) ($n \approx 1.9$) which traps about 20~30% of the generated light in each the substrate (substrate mode) and the organic/ITO layers (waveguide mode).^[13,17,19,20]

To mitigate these substrate losses, external extraction structures such as pyramidal arrays,^[19] microlenses,^[23,87,88] and light scattering layers^[20,22,89-91] have been extensively studied, with consistent reports of these mechanisms enhancing the total outcoupled light by approximately 100%. For suppression of the waveguide mode, several groups have incorporated technologies such as photonic crystals,^[92-94] low-index grids,^[17] and high-refractive index substrates.^[95-98] Amongst these techniques, substrate structures utilizing an amalgamation of the aforementioned technologies have demonstrated the highest efficacies. Reineke *et al.* demonstrated an improved white OLED (WOLED) using a high refractive index glass substrate ($n = 1.78$) in conjunction with a periodic outcoupling structure which achieved a power efficiency of 90 lm W^{-1} (34% EQE) at $1,000 \text{ cd m}^{-2}$.^[95] Wang *et al.* reported a flexible green OLED with performance metrics of $\sim 186 \text{ lm W}^{-1}$ ($\sim 60\%$ EQE) at $1,000 \text{ cd m}^{-2}$ achieved by using a multifunctional anode stack comprising a high-index Ta_2O_5 layer, a thin gold layer, a hole-injection MoO_3 layer, and a lens-based external structure.^[99]

Though OLED research has garnered progressively increasing attention in recent years, a comprehensive solution for the simultaneous mitigation of the substrate and waveguide mode has not yet surfaced. This comprehensive solution would synergistically consider effects of the conductor, light scattering, and index matching while adopting a fiscally feasible fabrication approach that can be translated to high volume production at low cost. This chapter focuses on the development of an integrated strategy for the fabrication of a flexible OLED substrate with high optical enhancement. The feasibility of this nanocomposite structure by utilizing silver

nanowires (AgNWs) embedded within a composite light scattering layer comprising an acrylate admixed with high index barium strontium titanate (BST) nanoparticles was investigated. The use of AgNWs as the conductive medium in replacement of ITO eliminates the mismatch of refractive indices between the organic layers and the substrate, thus enabling the inclusion of a high index polymer ($n \sim 1.7$) to index match with the organic layers ($n \sim 1.7-1.8$). Individual parameters, including the concentration of the light-scattering BST nanoparticles and the thickness of the high index polymer relevant to the microcavity tuning have been systematically investigated to maximize the light outcoupling efficiency. With the optimized substrate, resulting WOLED devices are shown to yield a power efficacy (PE) of 107 lm W^{-1} and an EQE of 49% at $1,000 \text{ cd m}^{-2}$.

3.2. Experimental Section

3.2.1 Materials

AgNWs (AW030LP) were purchased from Zhejiang Kechuang Advanced Materials Co., LTD. Poly(trimellitic anhydride chloride-co-4,4'-methylenedianiline) (PAI), 2,2-dimethoxy-2-phenylacetophenone (photoinitiator), 2-propanol (IPA), methanol, acetone, N-methyl-2-pyrrolidone (NMP), dimethyl sulfoxide (DMSO), Zonyl FS-300 fluorosurfactant, cesium fluoride (CsF), and aluminum were purchased from Sigma-Aldrich. Ethoxylated bisphenol-A dimethacrylate (SR540) and ethoxylated trimethylolpropane triacrylate (SR499) were obtained from Sartomer USA. BST nanoparticles (NanOxide HBS-2000) and surfactant (NanoSpense 484) were purchased from TPL, Incorporated. PEDOT:PSS (Clevios A14083) was purchased from Heraeus. N,N'-di(naphthalene-1-yl)-N,N'-diphenyl-benzidine (NPB) was purchased from Jim

OLED Materials Tech. Iridium bis(4-phenylthieno[3,2-c]pyridinato-N,C2') acetylacetonate (PO-01) and Bis(2-(2-hydroxyphenyl)-pyridine) beryllium (BePP₂) were obtained from Lumtec.

3.2.2 Nanocomposite Substrate Fabrication

The purchased AgNWs were diluted in a solvent mixture of methanol/IPA (1:2, volume ratio) at 0.5wt%. The AgNW solution was coated following the procedure previously reported.^[100] PAI was dispersed in NMP by vigorously stirring for 2 hrs, spin-coated on top of the AgNWs at 4000 rpm for 1 min, and annealed at 115°C for 20 min for imidization. The precursor of the light scattering layer was prepared by mixing the BST nanoparticles in a 2:1 SR499/SR540 solution containing 0.5 wt% 2,2-dimethoxy-2-phenylacetophenone and 9×10^{-4} wt% NanoSpere 484. The sandwich method was used to coat the light scattering layer on top of the PAI by using 90 μ m tape spacers and a cover glass. The light scattering layer was cured using a Dymax ultraviolet curing conveyor equipped with a 2.5 W cm⁻² Fusion 300S type 'H' ultraviolet curing blub, at a speed of 0.9 feet per minute for one pass. The resulting nanocomposite substrate was peeled off of the glass substrates.

3.2.3 Fabrication of WOLED

The standard device structure is substrate / anode / PEDOT:PSS (40nm) / TAPC (60nm) / PO-01 (0.5nm) / NPB (15nm) / BePP₂ (40nm) / CsF (1nm) / aluminum (80nm). The freestanding electrodes (nanocomposite substrates and ITO/glass substrates) were cleaned in an ultrasonic bath with detergent and DI water for 30 min, acetone for 20 min, and IPA for 20min. A PEDOT:PSS solution containing 5 vol% DMSO and 0.3 wt% Zonyl FS-300 fluorosurfactant was spin-coated on the freestanding electrodes at 4000 rpm and annealed at 130°C for 30 min. Next,

the substrates were brought into a vacuum evaporation chamber (base pressure of $\sim 1 \times 10^{-6}$ mbar) for thermal evaporation of the subsequent layers at a rate of 0.1-0.3 nm s⁻¹ for NPB and BePP₂, 0.01 nm s⁻¹ for PO-01 and CsF, and 0.5 nm s⁻¹ for aluminum. The CsF/Al contact was fabricated with a 0.13 cm² device area.

3.2.4 Characterization Methods

Scanning electron microscopy (SEM) was performed on a JOEL JSM-6701F scanning electron microscope. Surface topography was carried out on a Bruker Dimension Fastscan Scanning Probe Microscope (SPM). Transmittance spectra were obtained with a Shimadzu UV-3101PC with an integrating sphere setup. Film thicknesses were measured with a Dektak 6 Surface Profilometer. Electrical measurements for the WOLED were carried out using a homemade system consisting of a Keithley 2400 source meter and a calibrated silicon photodetector by sweeping the applied voltage from 0 to 6 V in a nitrogen-filled glovebox. EQE was calculated assuming the emission profile of the devices to be Lambertian emission, and the electroluminescence (EL) spectrum was measured using a Photoresearch SpectraScan Spectroradiometer PR-655. All characterization tests were carried out at room temperature.

3.3 Results and Discussion

3.3.1 Mechanism of Light Extraction

Figure 3.1a illustrates the layered structures of the composite substrate and possible outcoupling paths of photons in an OLED device by means of a high index polymer (HIP) layer and a light scattering layer. Angular emissions from the organic emitting compounds in most conventional OLEDs are isotropic, and photons that travel at a lower angle (at angles close to

being perpendicular to the substrate surface) are emitted from the OLED without effects of light extraction structures as depicted in Ray A. For photons emitted at high angle modes, the light extraction structures of the nanocomposite substrate can redirect the photons towards the substrate/air interface for enhanced light outcoupling through refraction and/or reflection (Ray B and Ray C).^[22] Photons that enter the light scattering layer may be scattered back into the OLED stack where it may be absorbed or reflected back into the scattering layer depending on the effective absorbance of the OLED (Ray D). Additionally, AgNWs may also redirect photons that are reflected at the interface of the HIP layer/light scattering layer since the refractive index difference of the HIP layer to the light scattering layer is from $n \sim 1.70$ to $n \sim 1.53$, where total internal reflection is likely to occur (Ray E). In real devices, a combination of the aforementioned paths occur. Photons may be lost at low nanoparticle concentrations when back-reflection towards the substrate/air interface (as depicted by Ray C) is insufficient or at high concentrations when back scattering towards the OLED stack (as depicted by Ray D) is excessive. The first part of this paper focuses on the optimization of the light scattering layer in favor of the optimal nanoparticle concentration. In the second part of the discussion, the microcavity effect was investigated at length by correlating theoretical simulation to empirical results. Specifically, the dipole emission model and the transfer matrix method were used for simulating the microcavity effect of HIP thickness on the light outcoupling efficiency of the OLED device. Respective OLED devices with varying thicknesses of the HIP layer were fabricated and tested experimentally to validate the theoretical simulation. With this approach, outcoupling enhancement can be achieved without alteration of the organic layers, which would otherwise affect the electrical characteristics of the device.

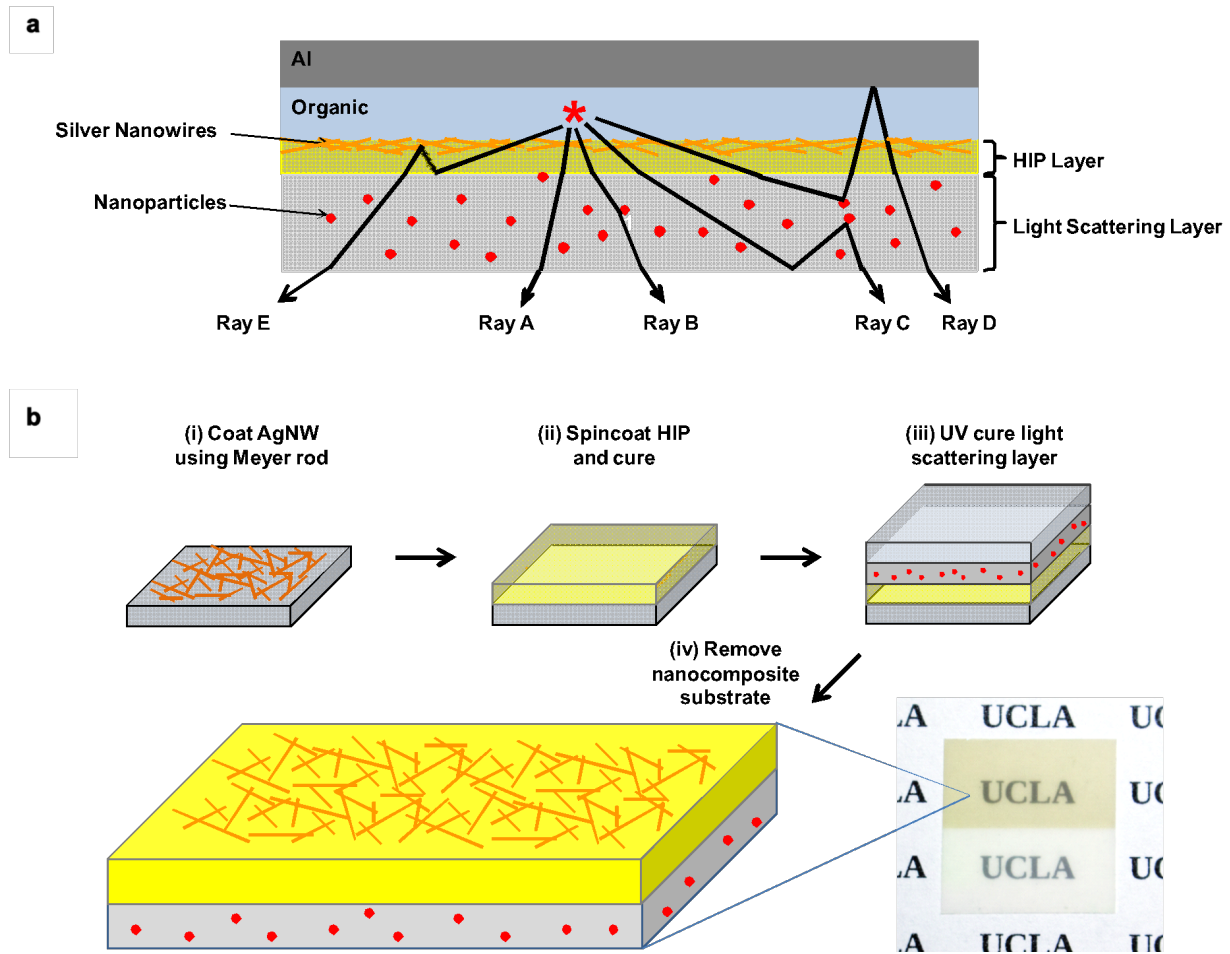


Figure 3.1. a) Schematic diagram of an OLED device with nanocomposite substrate and the optical mechanism leading to out-coupling of the substrate and waveguide modes. b) Fabrication process for a freestanding nanocomposite substrate containing silver nanowires embedded in the HIP layer and BST nanoparticles embedded in the light scattering layer. The inset shows an optical image of the nanocomposite substrate. (Diagrams are not to scale.)

3.3.2 Fabrication Process and Characterization of OLED Nanocomposite Substrate

The fabrication process of the nanocomposite substrate can be summarized in four steps: (i) coating a layer of AgNWs atop a glass substrate; (ii) spin-coating a layer of high index

polymer (HIP) on top of the AgNW layer; (iii) transferring the resulting films with a light scattering layer by a sandwich transfer method; and (iv) releasing the nanocomposite substrate from glass. **Figure 3.1b** illustrates the step-by-step preparation. The sandwich transfer method consists of coating a monomer precursor solution between two glass slides separated by 90 μm tape spacers, followed by UV curing and removal from the release glass substrates to obtain freestanding nanocomposite electrodes. More in depth details can be found in previous reported works.^[5,8,100] The resulting composite electrode exhibits a sheet resistance of $15 \Omega \square^{-1}$ at $\geq 91\%$ linear transmittance, comparable to AgNW electrodes with high aspect ratio (average length 95.1 μm) AgNWs.^[101] The AFM image in **Figure 3.2** reveals that the nanocomposite substrate has a root mean square roughness (R_q) of 1.53 nm and a maximum roughness depth (R_{MAX}) of 26.0 nm, which are comparable to the surface roughness of ITO coated on glass with surface resistivity of 8-12 Ωsq^{-1} at 84% transmittance.^[102,103]

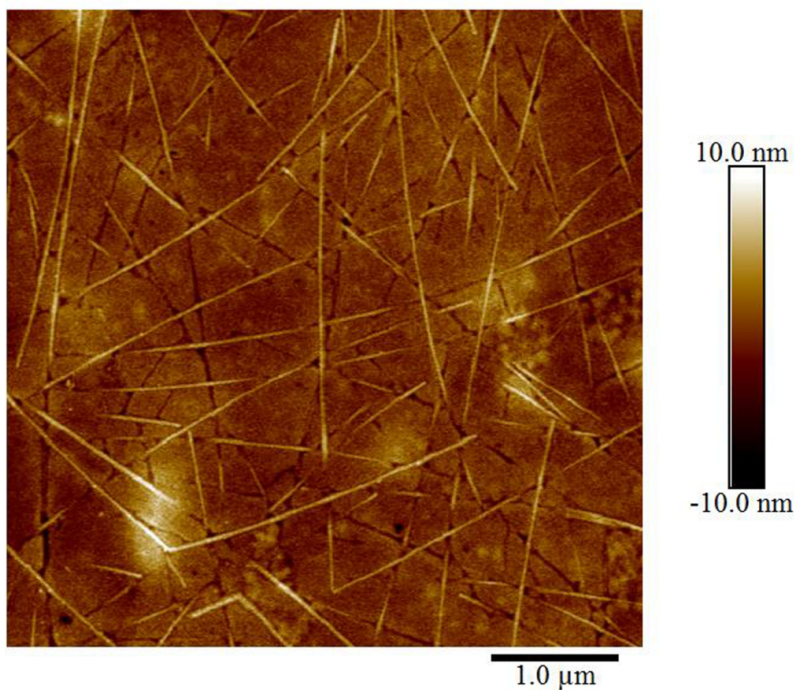


Figure 3.2. AFM image of the conductive surface of the nanocomposite substrate.

3.3.3 WOLED Performance with Different Light Scattering Particle Concentration

For simplicity of OLED fabrication, a two color-complementary hybrid WOLED device structure was adopted to evaluate the composite electrodes. The WOLED structure consists of a PEDOT:PSS hole injection layer, a TAPC (4,4'-Cyclohexylidenebis[N,N-bis(4-methylphenyl)benzenamine] hole transport layer, an NPB (N,N'-di(naphthalene-1-yl)-N,N'-diphenyl-benzidine) blue fluorescent emitting layer that is doped with PO-01 (Iridium bis(4-phenylthieno[3,2-c]pyridinato-N,C2') acetylacetonate) yellow phosphorescent material, a BePP₂ (Bis(2-(2-hydroxyphenyl)-pyridine) beryllium) electron transport layer, a CsF (cesium fluoride) electron injection layer, and an aluminum cathode (**Figure 3.3a**). The inspiration for this device structure was drawn from a WOLED architecture reported by Forrest and Thompson et al. that uses a fluorescent emitting dopant to harness high energy singlet excitons for blue emission and phosphorescent dopants to harvest the lower-energy triplet excitons to achieve a power efficiency of $\sim 37.6 \text{ lm W}^{-1}$, which is comparable to fully phosphorescent devices.^[104–107] By utilizing a hole transport layer (HTL) and an electron transport layer (ETL) with resonant injection into the phosphor triplet state, the loss in energy from intersystem crossing into the emissive triplet state can be minimized to yield high power efficiency.^[104] The HOMO and LUMO energy levels of the OLED materials used in this study with resonant energy transfer (ΔE_T) of $< 0.3 \text{ eV}$ are shown in Figure 3.3, and the triplet energy level of NPB and PO-01 are 2.3 eV and 2.2 eV, respectively.^[16,108]

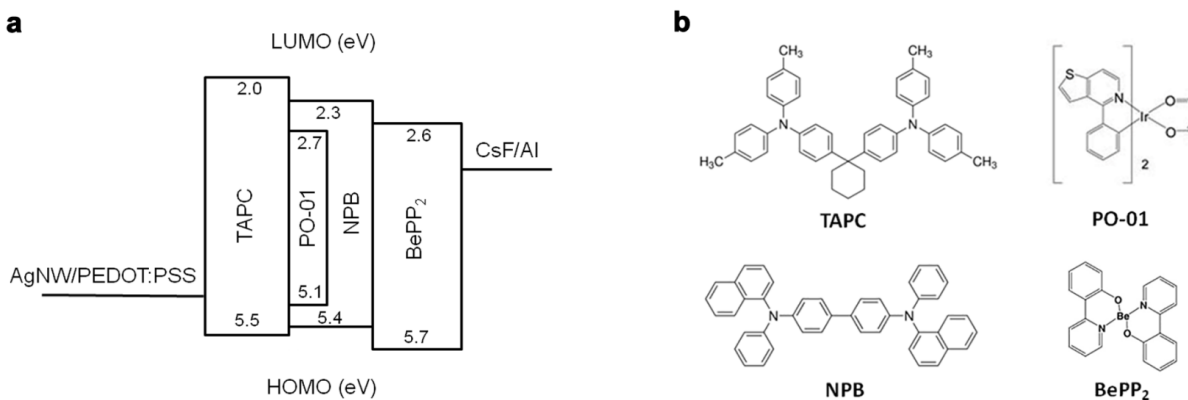


Figure 3.3. a) Schematic energy-level diagram of the two color-complementary hybrid WOLED device. b) Molecular structures of the relevant materials used in the fabrication of the WOLED.

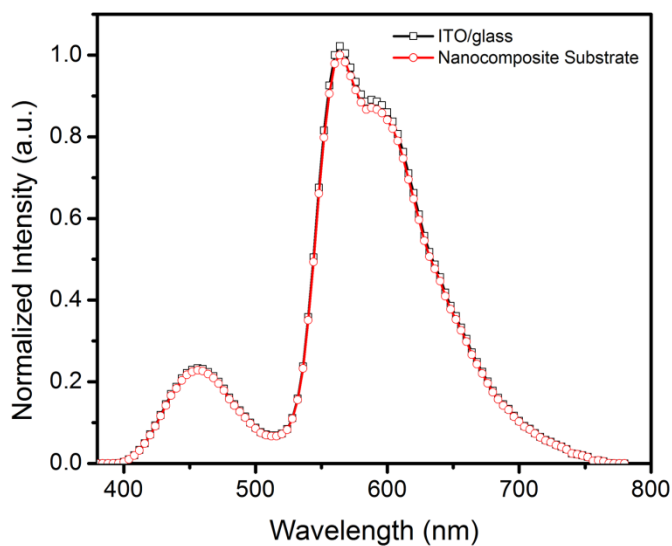


Figure 3.4. Normalized electroluminescence spectra of WOLED with ITO and nanocomposite anodes.

The resulting WOLED exhibits a power efficacy of 47.17 lm W⁻¹ for ITO/glass substrates and an EQE of 17.6% at 1,000 cd m⁻² with CIE coordinates of (0.45,0.41) and CRI of 51. AgNW electrodes have been well reported to exhibit comparable electrical conductivity and

transparency in comparison to ITO.^[24,25,51] WOLED fabricated on top of electrodes made of only AgNWs embedded in an acrylic matrix shows an approximate enhancement of $\sim 1.33x$, with an average power efficacy of 62.89 lm W^{-1} and an average EQE of 23.5% at $1,000 \text{ cd m}^{-2}$. Similar enhancements using only silver nanowire electrodes have also been previously reported.^[26,109] This enhancement was achieved without the use of any additional outcoupling structures (no high refractive index polymer or light scattering particles) and is believed to be influenced by the replacement of ITO with AgNWs which reduces light reflection between the anode/substrate interface and suppresses a portion of the waveguide mode in the device.

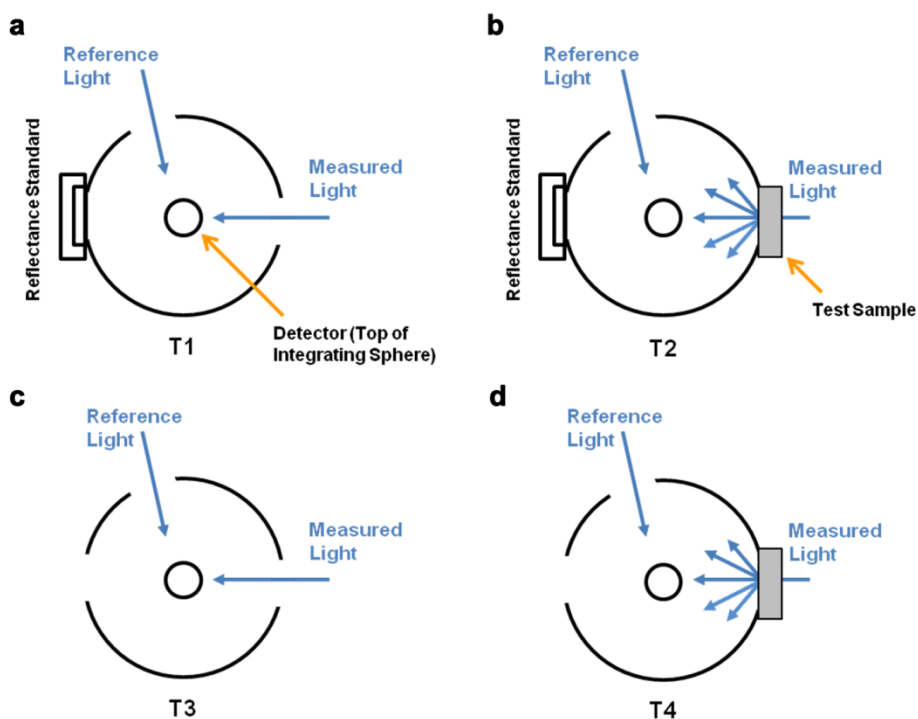


Figure 3.5. Shimadzu integrating sphere setup for measuring a) incident light (T1), b) total light transmitted by specimen (T2), c) light scattered by instrument (T3), and d) light scattered by instrument and specimen (T4).

A light scattering layer is an effective approach for light extraction from OLEDs in general lighting applications as it offers light outcoupling enhancement in addition to other innate advantages such as constant spectral curves (color) over all observation angles and symmetric, uniform illumination with Lambertian distribution due to its diffuse scattering effect.^[110] A standard design of the light scattering layer consists of high index scattering particles embedded within a lower index matrix material.^[111,112] The light scattering layer used in this study was fabricated by UV curing a monomer solution consists of BST nanoparticles with a refractive index of 2.6 that are dispersed within an acrylic matrix with a refractive index of 1.53.^[26] **Figure 3.6a** and **3.6b** show the measured total transmittance and diffuse transmittance of the light scattering layers at 1, 2, 3, 4, and 5wt% BST concentrations, and the resulting haze values are shown in **Figure 3.6c** (see **Figure 3.5** for haze measurement and calculation). The light scattering layer consists of BST nanoparticles with 200 nm average diameter, and the inset image in **Figure 3.6a** shows the optical images of the light scattering films at 90 μm thickness. Results from **Figure 3.6a-b** suggest that the light scattering films increase in haziness and decrease in transparency with increasing nanoparticle concentration, which correlates to the increasing scattering effect of the film. Although it has been proven that the scattering effect can enhance light outcoupling,^[20,22,89] excessive light scattering can also decrease the enhancement factor of the WOLED devices as light traveling through the light scattering layer could be scattered in both forward and backward directions. The optimal condition in light scattering film is for photons reflected from the substrate/air interface to be redirected to the interface at an angle within the escape cone to increase total light extraction probability and thus OLED efficiency. A higher scattering may increase the probability of light backscattering before the light even reaches the substrate/air interface, which reduces the total transmittance of the light

scattering layer. An optimum is therefore expected between maximizing haze and total transmittance of the light scattering film.^[22]

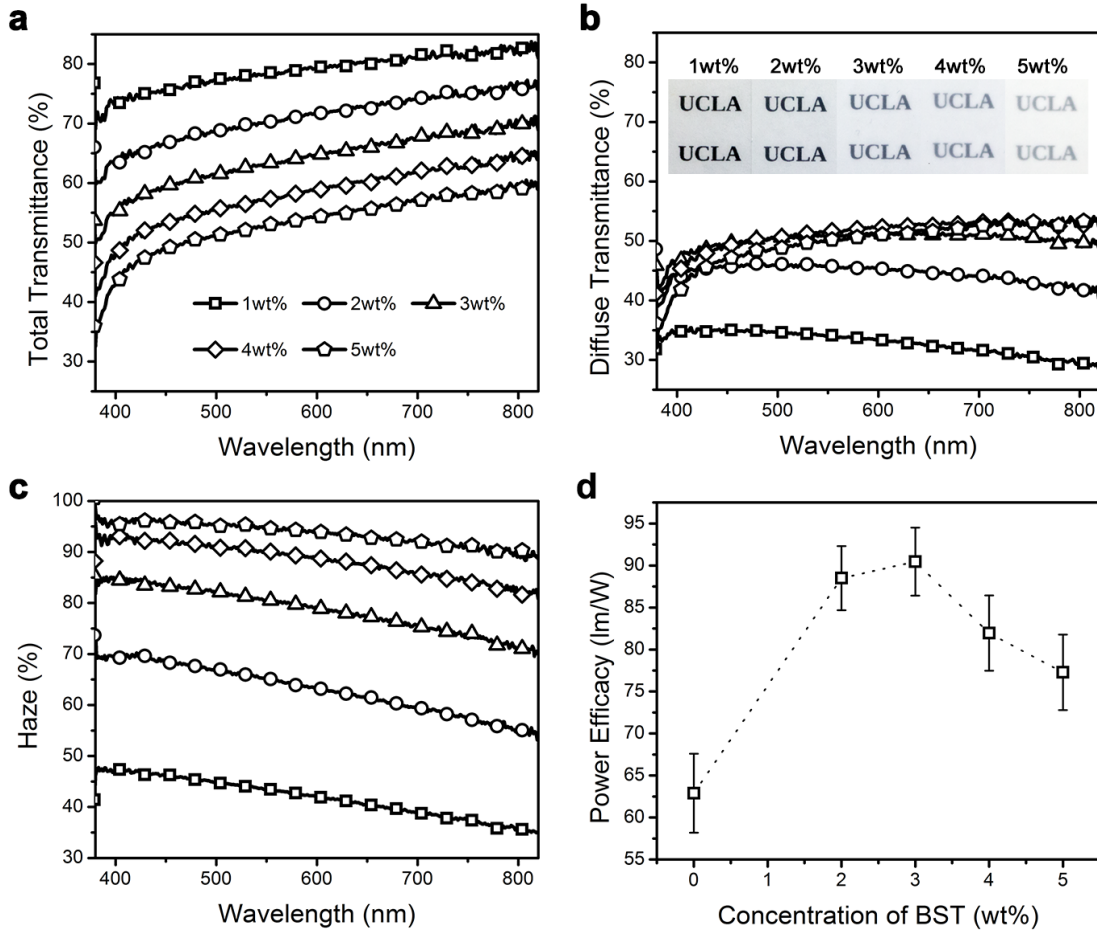


Figure 3.6. a) Measured total transmittances (inset is a photograph of the corresponding light scattering layers), b) measured diffuse transmittances, and c) calculated haze of the light scattering layer as functions of BST concentration. d) A correlation between device power efficacy versus BST concentration showing an optimum between total transmittance and haze.

The total transmittance of the films decreases from 70.1% (2wt%) to 52.7% (5wt%) at 550nm while the diffuse transmittance increases from 45.7% to 50.9% at 550nm, respectively,

but remains at approximately 51% for concentrations greater than 3 wt%. This correlation indicates that light outcoupling efficiency saturates at a BST concentration around 3 wt%. However, the total transmittance through the films is reduced beyond 3 wt% of BST due to loss in linear transmission. **Figure 3.6d** shows the power efficacy of WOLED fabricated on the composite electrodes with various BST concentrations. The highest power efficacy was observed from the devices fabricated on the substrates containing 3wt% BST nanoparticles, achieving a power efficacy of $\sim 90.5 \text{ lm W}^{-1}$. This experimental result correlates to an enhancement ratio of ~ 1.92 over ITO and ~ 1.44 over substrates containing only AgNWs, which indicates sufficient substrate mode being extracted using light scattering mechanism. A BST concentration at 3 wt% shows the optimal condition between optical haze and total transmittance and is used for the remainder of this study.

3.3.4 Microcavity Effect of the High Refractive Index Polymer Layer

With the established optimal light scattering mechanism, a high refractive index polymer, polyamide-imide (PAI), was introduced to further improve the light outcoupling by tuning the microcavity effect across the optical layers without affecting the electrical characteristics of the device. The PAI film has a refractive index of 1.7 after thermal annealing, is optically transparent in the visible region, and is mechanically flexible.^[89] The outcoupling enhancement of the device structure was simulated based on the dipole emission model and the transfer matrix method^[113,114] using the Setfos software. **Figure 3.7b** shows the enhancement ratio based on the luminance of the outcoupled light as a function of the thicknesses of the PAI films. Peak enhancement is found at PAI thicknesses of 70, 230, 400, and 560nm, which corresponds to a potential enhancement of 15.6, 12.5, 9.6, and 7.6%, respectively. The corresponding PAI

thickness at the enhancement peaks can be determined by calculation based on optical thickness using the equation

$$\frac{m}{2} \lambda = \sum_i n_i d_i \quad (1)$$

where m is an integer, λ is the peak wavelength of the emitted light, and n and d are the refractive index and the thickness of the materials, respectively.^[115] The optical thicknesses of the OLED stack from the PO-01 emitters and the PEDOT:PSS can be estimated by multiplying 60 nm by 1.7 and 40 nm by 1.53, respectively, and the optical thickness of a PAI layer with a thickness of 70 nm can be calculated by multiplying 70 nm by 1.7. A summation of the optical thicknesses gives an optical thickness of ~ 282.2 nm, which corresponds to an m of 1 with a λ of 560 nm. A similar calculation of the other PAI thicknesses of 230, 400, and 560 nm results in m of 2, 3, and 4, respectively.

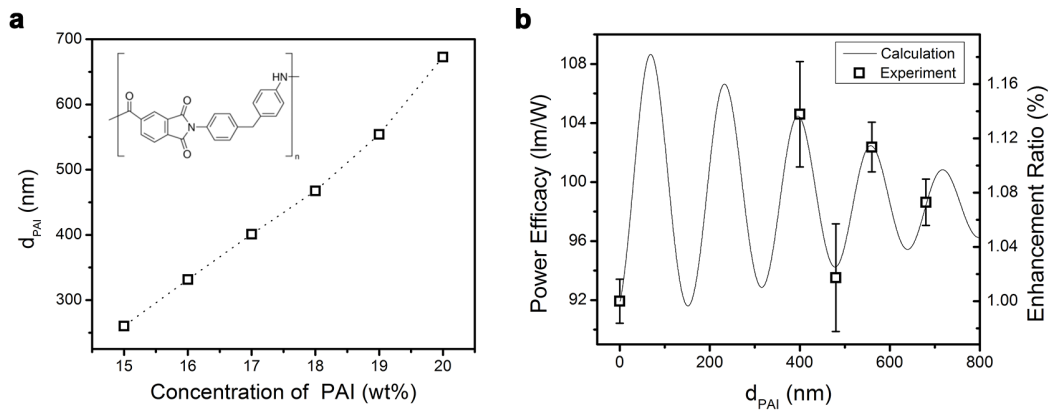


Figure 3.7. a) Measured thickness of the PAI layer as a function of PAI concentration in NMP solutions. The inset shows the molecular structure of PAI. b) Comparison of calculated and experimental values of power efficacy versus PAI thickness showing outcoupling enhancement at PAI thickness correlating to microcavity tuning. Enhancement ratios are based on theoretical results obtained from the Setfos simulation software.

The simulated enhancement ratios were obtained and compared to empirical results. Composite electrodes were fabricated by introducing a thin PAI layer in addition to the pre-determined light scattering film.^[89] The thickness of the PAI layer can be controlled by spin-coating a solution of PAI in n-methyl-2-pyrrolidone (NMP) with various concentrations (**Figure 3.7a**), with all thicknesses verified using a surface profilometer. The power efficacy of WOLEDs fabricated on nanocomposite substrates with the AgNW / PAI / light scattering layer structure are plotted in Figure 3.7b. The reference WOLED device without PAI layer shows an average power efficacy of $\sim 91.8 \text{ lm W}^{-1}$. In contrast, WOLED devices fabricated on nanocomposites with PAI thicknesses of 400, 480, 560, and 680 nm show power efficacies of 104.6, 93.51, 102.4, and 95.2 lm W^{-1} , respectively. Note that although PAI film thicknesses of 70 and 230 nm show even higher enhancement factors in the theoretical model, PAI layer with thickness below 400 nm, the thickness of the AgNW layer, cannot be obtained experimentally due to the rough surface of the AgNWs. Nevertheless, results obtained with PAI thicknesses beyond 400 nm are in good agreement with the simulated values, providing valuable means to further improve the performance of such optical films.

Figure 3.8a shows the Luminance-Voltage-Current density (L-V-J) characteristics of WOLED devices fabricated on optimized nanocomposite substrates in comparison with ITO control devices. The parameters of an optimized nanocomposite substrate show sheet resistance of $\sim 15 \Omega \square^{-1}$, with 400 nm of PAI layer and 90 μm of light scattering layer containing 3wt% BST nanoparticles. Though devices fabricated on the nanocomposite substrates show a lower current density in comparison with ITO, current efficiency (CE) and power efficacy (PE) show enhancement factors of nearly 2.75 and 2.27, respectively, with a CE of 126.7 cd A^{-1} and PE of

107.16 lm W⁻¹ for the nanocomposite substrate and a CE of 45.9 cd A⁻¹ and a PE of 47.17 lm W⁻¹ for the ITO/glass control at a luminance of 1000 cd m⁻² (**Figure 3.8b**). Similarly, WOLED fabricated with the nanocomposite substrate achieved an EQE of 48.6%, corresponding to an enhancement factor of ~2.76 in comparison to the 17.6% EQE of the ITO/glass control device (**Figure 3.8c**). The enhancement in CE, PE, and EQE of the nanocomposite substrate is attributed to the combined effects of the refractive index matching of the substrate to the organics, the microcavity tuning to further enhance outcoupling of light into the substrate, and the light scattering by the nanoparticles to extract light from the substrate mode.

Based on this study, a new strategy for a cost effective fully solution fabrication process of a flexible OLED substrate with high optical enhancement has been developed. A nanocomposite substrate fabricated using polymer based materials provides the benefits of adaptable form factors and low material and fabrication costs. Additionally, the fabrication process can be readily adopted in roll-to-roll technologies for mass production. The replacement of the ITO electrode with AgNWs provides additional advantages in light outcoupling as described above, and light scattering particles can potentially achieve extraction enhancement of the substrate mode in comparison to half sphere microlens. This fabrication strategy of the nanocomposite substrates has been shown to have comparable or better light enhancement factor in comparison to other outcoupling techniques based on substrate architectures. The current strategy has shown a more than doubled performance enhancement relative to commercial ITO by carefully modulating the respective parameters of the multilayered structure. It is worth noting that an additional performance improvement may be revealed by coupling with optimization of the OLED device structure and processing conditions, which will be the focus of future work related to this topic.

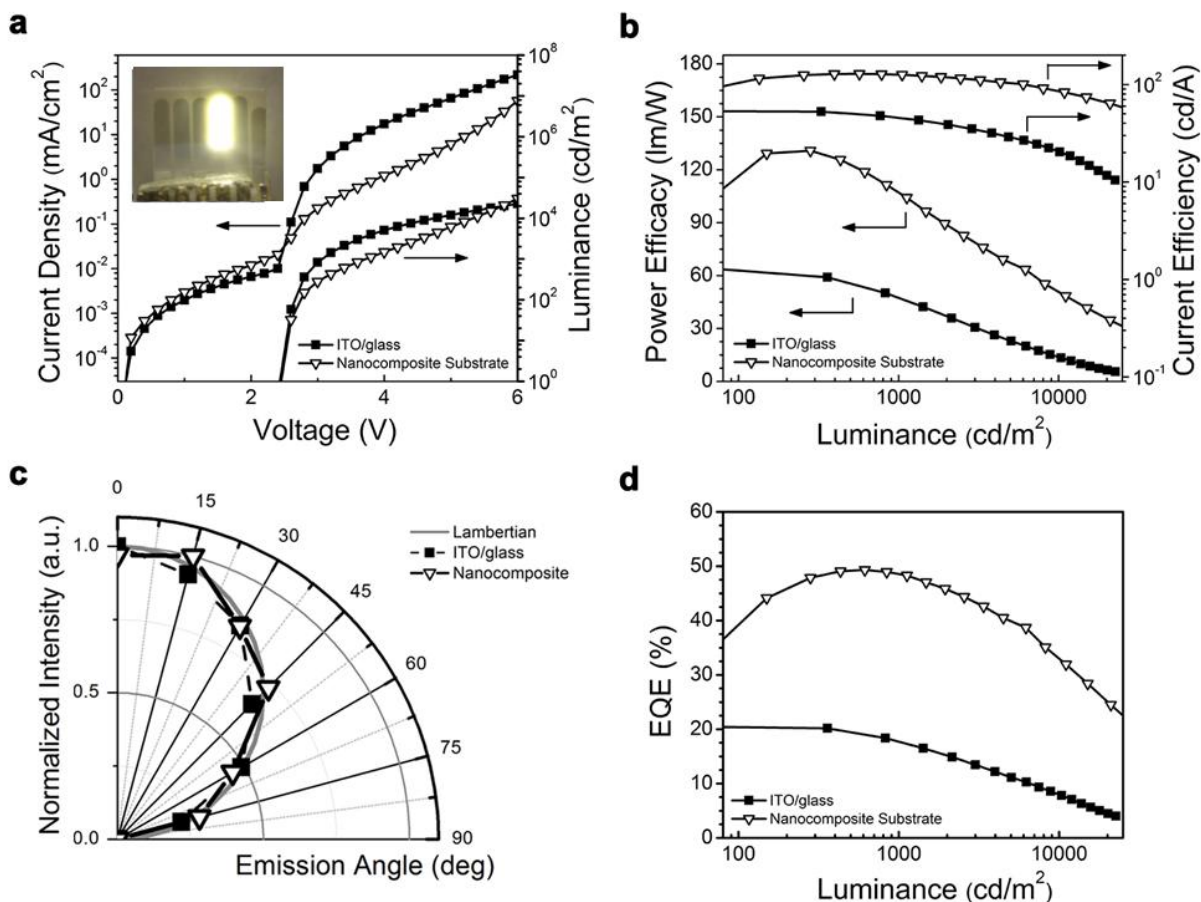


Figure 3.8. Comparison of performance characteristics of WOLED devices with ITO and nanocomposite anodes. a) Current-Voltage-Luminance (J-V-L) characteristics. The inset shows a device fabricated on a nanocomposite substrate operating at 4 V. b) Power efficacy-Luminance-Current Efficiency (PE-L-CE) characteristics. c) Angular dependence of electroluminescence intensity. d) EQE vs Luminance. (ITO/glass and nanocomposite substrate represents WOLEDs with the device structure of substrate / anode / PEDOT / TAPC / PO-01 / NPB / BePP₂ / CsF / Aluminum.)

3.4 Conclusion

A fully solution processed, flexible, transparent conductive nanocomposite substrate was fabricated to investigate its applicability in efficiently outcoupling light from WOLEDs. These WOLEDs were fabricated using a two color-complementary hybrid structure that allows for efficient harvesting of the singlet and triplet states of the fluorophor and phosphor emitters by minimizing energy losses during the energy transfer and exciton interaction processes. The enhanced WOLED device performance of the nanocomposite substrates was realized through the optimization of the microcavity of the device/substrate structure and the light scattering modes to maximize light outcoupling. With these tandem components, performance metrics of 126.7 cd A⁻¹ CE, 107.16 lm W⁻¹ PE, and 48.6% EQE were obtained. This nanocomposite substrate architecture can be an effective outcoupling enhancement strategy for integration in a variety of applications, especially in future lighting applications.

Chapter 4

Color Rendering of WOLED through Dopants within the OLED Substrate

4.1 Introduction

Interest in the application of white OLED (WOLED) technology for general solid-state lighting applications and flat panel display backlights has been steadily increasing, especially with the increase in published work in this area with improvements of the power efficiency that has attained a level that is widely deemed acceptable for the lighting market.^[15,86,95,99] Besides high efficiency, the color characteristics of the emitted white light are often regarded as another essential factor in rating the quality of the illuminated white-light. There is in general a tradeoff in WOLEDs between efficiency and color as the most efficient device architectures have to be modified with the addition of less efficient true-blue phosphors, such as FIrpic in the three or more component phosphorescent WOLEDs that can yield a warm white emission with CRI >80.^[116,117]

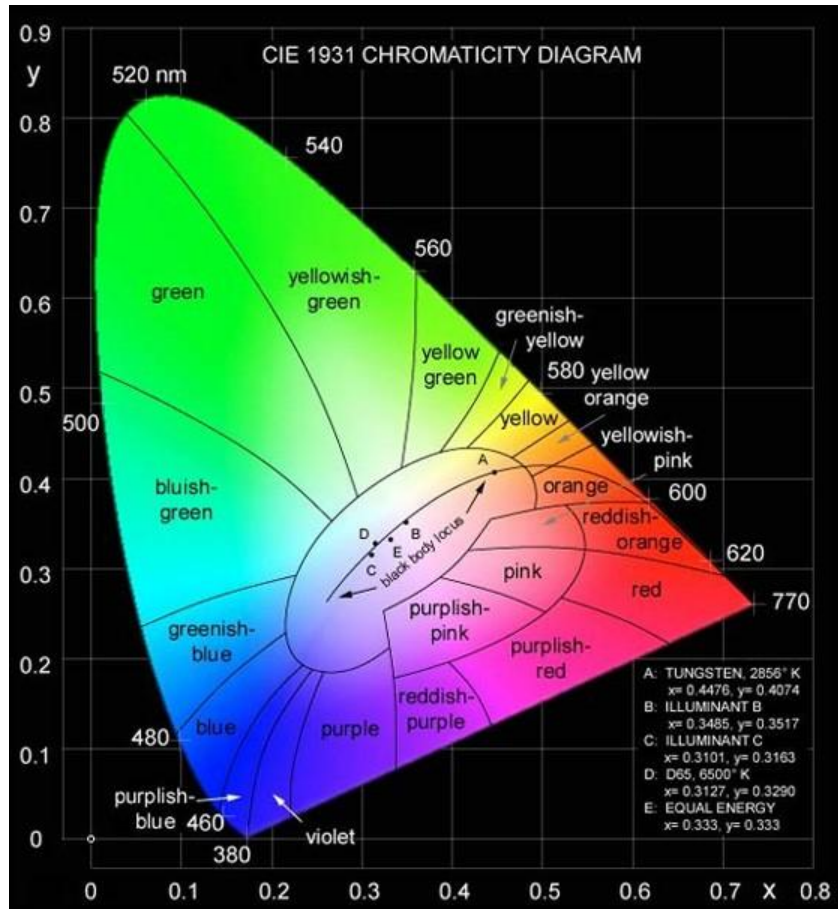


Figure 4.1. CIE 1931 Chromaticity Diagram. The outer curved boundary is the spectral (monochromatic) locus with wavelengths shown in nanometers. The solid curve through the middle is the black body locus, with the dots on in representing the black body temperatures shown in the inset box.

There are numerous ways to measure the color appearance of the light source. The International Lighting Commission established a colorimetry system for color matching that is referred to as CIE (Commission Internationale de l'Eclairage) based on the human eyes' three cone photoreceptors, and two numbers (x and y) are used to describe a light source color mathematically based on its chromaticity coordinates, or simply its chromaticity (**Figure 4.1**). For the ease of comparison, correlated color temperature (CCT) and coloring rendering index

(CRI) are often used in the scientific and industrial communities. CCT is a measurement of the light source color appearance defined by the proximity of the light source's chromaticity coordinates to the blackbody locus and is represented by a single number with the lower values being an indicator of "warm" light, reminiscent of the yellowish candlelight, and higher values for "cooler" light with a bluish hue. In contrast, CRI does not indicate the apparent color of the light source but is a measurement of the light source's ability to show object colors compared to a reference source (incandescent light or daylight) and is determined by the light source's spectrum. High-quality white-light illumination is often characterized based on the requirement for CIE_{x,y} coordinates similar to those of black-body radiation with a correlated color temperature (CCT) between 2500K and 6500K and a color rendering index (CRI) above 80.^[14,117]

Although highly efficient white light can be produced simply through emission based on two complementary colors, the CRI of the two-component devices is usually mediocre at best (as demonstrated in the previous chapter with the high-efficiency WOLED with a mere CRI of 51). Several groups have reported improvements in the CRI of the WOLEDs in the In 2002, D'Andrade et al. first demonstrated that the CRI of phosphorescent WOLEDs could be greatly enhanced from 50 to 83 by using three (red, green, and greenish-blue) phosphorescent dopants instead of two complementary (red and greenish-blue) dopants.^[118] In order to obtain a deeper blue emission, D'Andrade et al. and Schwartz et al. have shown CRI improved to 85-86 by fabricating hybrid three-color WOLEDs using blue fluorophors and red/green phosphors.^[104,119] As shown in **Figure 4.2** of the power efficiency and CRI performances of the WOLED in this study, compared with values from previously reported publications, the majority of the WOLEDs with CRI > 80 has a power efficiency below 40 lm W⁻¹ and implicates the difficulty in achieving WOLEDs with both high CRI and power efficiency simultaneously.

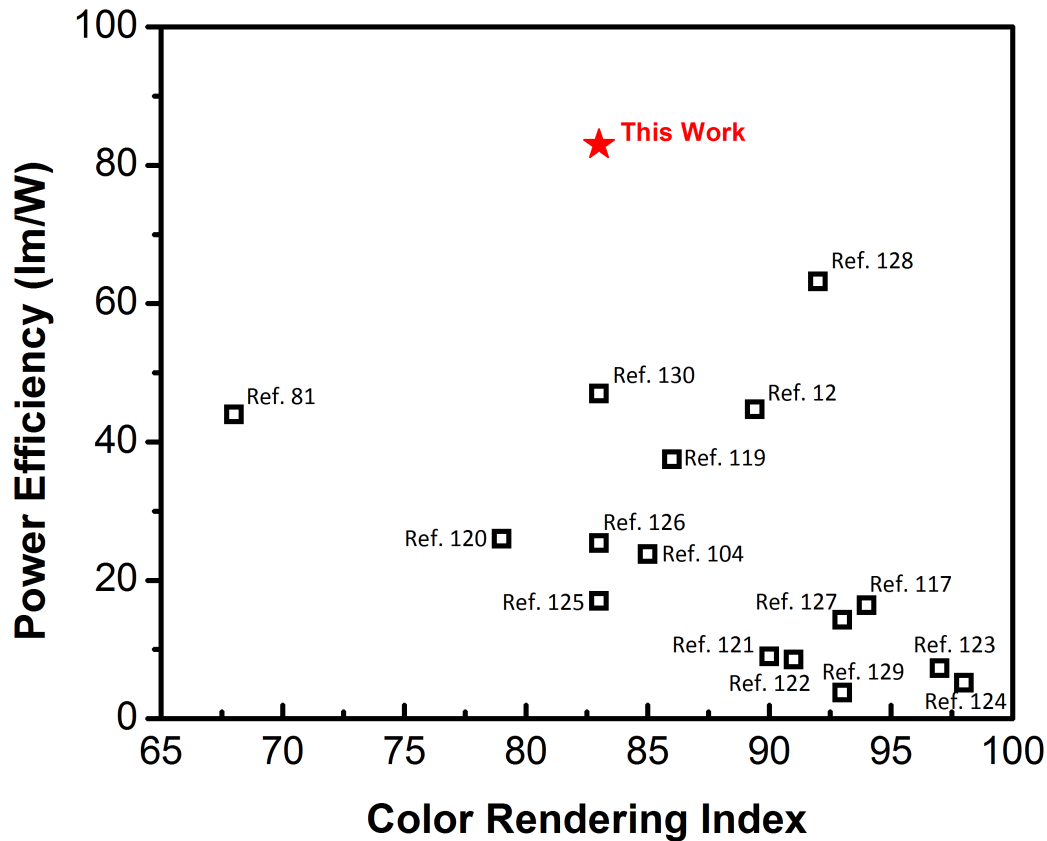


Figure 4.2. Power efficiency and CRI performances of the WOLED in this study, compared with values from previously reported publications.

Recent publications have shown an improvement in power efficiency for WOLEDs with high CRI through the fabrication of complex OLED devices architectures. Coburn et al. demonstrated three, four, and five cell device (up to 48 individually deposited OLED layers) to obtain devices with power efficiency of 40.6, 47.2, and 44.7 lm W^{-1} with CRI of 81.2, 85.2, and 89.4 respectively.^[12] Zhuang et al. has shown WOLEDs with two host-dopant emitting systems, consists of blue host-orange dopant and green host-red dopant, with well-aligned energy levels to achieve a CRI of 92 with power efficiency of 63.2 lm W^{-1} .^[128] Even though improvements in

power efficiency have been shown in these two WOLED architectures with CRI > 80, the overall power efficiency of these devices remains significantly lower than the maximum efficiency (>100 lm W⁻¹) achievable with WOLEDs with lower CRI.^[131,132]

An alternative approach is to generate white light by combining an organic light emitting diode that emits blue light and a color conversion layer (CCL). In this approach, some photons originating from the blue emitters are absorbed in the CCL and are down-converted to longer wavelength photons, thus allowing for an additional parameter for color tuning to obtain devices with higher CRI. The down conversion approach has been popular and successful in white inorganic LEDs due to its simplicity (without a major redesign of the device architecture) and was first introduced by Duggal et al. using a blue polymer OLED with a CCL of inorganic phosphors and organic dyes.^[129] Due to the limited efficiency of the blue polymer OLED, the power efficiency of the down-converted WOLED was not significantly high at 3.76 lm W⁻¹ at 1080 cd m⁻²; however, the resulting device featured an impressive CRI of 93. Krummacher and his group were the first to demonstrate down-conversion WOLEDs using blue phosphorescent emitters, and a maximum power efficiency of 25 lm/W was achieved.^[133] A few years later, Lee et al. reported a WOLED with microcavity-tuned highly efficient (>20% EQE) FIrpic-based OLED, down conversion phosphors, and microlens and obtained device performance up to 47 lm W⁻¹ at 1000 cd m² with a CRI of 83.^[130]

In this study, the CRI of a three-color WOLED is color tuned using a color conversion layer below the plastic light scattering substrate. The three-color fluoro blue-phosphorescent orange-red WOLED emits blue photons from the fluorescent NPB/BePP₂, yellow photons from the PO-01 phosphor, and red photons from the Ir(piq)₃ phosphor. By partially down converting the blue photons using a 4,7-bis{2'-9',9'-bis[(2''-ethylhexyl)fluorenyl]}-2,1,3-benzothiadiazole

(FBtF) dye, a higher distribution of photons near 520-550 nm wavelength was obtained to increase the CRI of the device up to 83. Using the light extraction mechanism discussed in the previous chapter, a light scattering layer was also implemented in this study to enhance the light outcoupling of the substrate mode. With the optimized substrate, resulting WOLED devices are shown to yield a power efficiency of 81 lm W⁻¹ and an EQE of 48.6% at 1000 cd m².

4.2. Experimental Section

4.2.1 Materials

AgNWs (AW030LP) were purchased from Zhejiang Kechuang Advanced Materials Co., LTD. All reactants for the synthesis of FBtF, 2,2-dimethoxy-2-phenylacetophenone (photoinitiator), 2-propanol (IPA), methanol, acetone, N-methyl-2-pyrrolidone (NMP), dimethyl sulfoxide (DMSO), Zonyl FS-300 fluorosurfactant, cesium fluoride (CsF), and aluminum were purchased from Sigma-Aldrich. Ethoxylated bisphenol-A dimethacrylate (SR540) and ethoxylated trimethylolpropane triacrylate (SR499) were obtained from Sartomer USA. BST nanoparticles (NanOxide HBS-2000) and surfactant (NanoSperser 484) were purchased from TPL, Incorporated. PEDOT:PSS (Clevios A14083) was purchased from Heraeus. N,N'-di(naphthalene-1-yl)-N,N'-diphenyl-benzidine (NPB) was purchased from Jim OLED Materials Tech. Iridium bis(4-phenylthieno[3,2-c]pyridinato-N,C2') acetylacetonate (PO-01) and Bis(2-(2-hydroxyphenyl)-pyridine) beryllium (BePP₂) were obtained from Lumtec.

4.2.2 Synthesis of FBtF

In a round bottom flask, 55.9 mmol (13.71 g) of 2-bromofluorene and 0.45 (0.144g) mmol of tetra-n-butylammonium bromide were dissolved in 100 mL of dimethyl sulfoxide with

23.15 mL of 50% wt/v potassium hydroxide and 29.84 mL of 2-ethylhexyl bromide was added to the mixture while stirring. After two days of stirring at room temperature, the mixture was quenched in water with a 50 mL 2M HCl solution, extracted with diethyl ether, dried over magnesium sulfate, filtered, and concentrated using a rotary evaporator. Excess 2-ethylhexyl bromide was removed via vacuum distillation at 1.3-1.5 torr. After distillation, the crude product was purified via flash column chromatography with hexane as the eluent to collect 2-bromo-9,9-di(2-ethylhexyl)-fluorene.

In another round bottom flask, 46.0 mmol (22.01g) of 2-bromo-9,9-di(2-ethylhexyl)-fluorene was dissolved in 115 mL of dry tetrahydrofuran under Argon. The solution was cooled to -78°C in a dry ice/acetone bath. 58.6 mmol of 2.5 M n-butyllithium in hexane was added dropwise. After stirring for 2 h at -78°C , 131.3 mmol of 2-isopropoxy-4,4,5,5-tetramethyl-1,3,2-dioxaborolane was added and stirred overnight while allowing the mixture to slowly warm to room temperature. The reaction mixture was then quenched in water with 75 mL of 2N HCl, extracted with diethyl ether, dried over magnesium sulfate, filtered, and concentrated using a rotary evaporator. The product was adsorbed on celite powder and purified via a silica gel dry vacuum column with a 1:0 to 6:1 hexane:ethyl acetate to collect 2-[9,9-bis(2-ethylhexyl)-fluoren-2-yl]-4,4,5,5-tetramethyl-1,3,2-dioxaborolane.

In a three-neck round bottom flask, 4.8 mmol of 4,7-Dibromobenzo[c]-1,2,5-thiadiazole and 10.6 mmol of 2-[9,9-di(2'-ethylhexyl)-fluoren-2-yl]-4,4,5,5-tetramethyl-1,3,2-dioxaborolane were dissolved in tetrahydrofuran under Argon. The mixture was added 5.6 g of potassium carbonate in a 2M aqueous solution and 0.05 mmol of $\text{Pd}(\text{PPh}_3)_4$ catalyst, degassed via freeze-pump-thaw and refluxed for 24 h. The product was extracted with diethyl ether, dried over magnesium sulfate, filtered, concentrated using a rotary evaporator, and purified via a column in

a 2:1 hexane:dichloromethane eluent to collect 4,7-bis{2'-9',9'-bis[(2''-ethylhexyl)fluorenyl]}-2,1,3-benzothiadiazole (FBtF).

4.2.3 Nanocomposite Substrate Fabrication

The precursor of the FBtF layer was prepared by mixing 0.3 wt% FBtF in 2:1 SR499/SR540 containing 0.5 wt% 2,2-dimethoxy-2-phenylacetophenone in methyl ethyl ketone (MEK) solvent via sonication for 30 min and dried using the rotary evaporator. The sandwich method was used to fabricate the color conversion layer by coating a FBtF-polymer film using two pieces of release glass by polymerization of the precursors using a Dymax ultraviolet curing conveyor equipped with a 2.5 W cm⁻² Fusion 300S type 'H' ultraviolet curing blub, at a speed of 0.9 feet per minute for one pass. On a separate piece of release glass, a AgNW solution, prepared by diluting the stock AgNW solution in a solvent mixture of methanol/IPA (1:2, volume ratio) at 0.5 wt%, was coated following the procedure previously reported.^[100]

The precursor of the light scattering layer was prepared by mixing 3 wt% BST nanoparticles in a 2:1 SR499/SR540 solution containing 0.5 wt% 2,2-dimethoxy-2-phenylacetophenone and 9×10^{-4} wt% NanoSpurse 484 in MEK via sonication for 3 h, filtered, and dried using a rotary evaporator. The sandwich method was used to fabricate the WOLED substrate/anode layer by coating the light scattering layer using 90 μ m tape spacers between the previously prepared color conversion layer (FBtF polymer film) and the previously prepared release glass coated with AgNWs. The light scattering layer was cured using the Dymax UV conveyor at a speed of 0.9 feet per minute for one pass. The resulting nanocomposite substrate was peeled off of the glass substrates.

4.2.4 Fabrication of WOLED

The WOLED device structure is substrate (FBtF layer + light scattering layer) / anode / PEDOT:PSS (40 nm) / TAPC (60 nm) / PO-01 (0.5 nm) / Ir(piq)₃ (0.5 nm) / NPB (15 nm) / BePP₂ (40 nm) / CsF (1 nm) / aluminum (80 nm). The freestanding electrodes (nanocomposite substrates and ITO/glass substrates) were cleaned in an ultrasonic bath with detergent and DI water for 30 min, acetone for 20 min, and IPA for 20min. A PEDOT:PSS solution containing 5 vol% DMSO and 0.3 wt% Zonyl FS-300 fluorosurfactant was spin-coated on the freestanding electrodes at 4000 rpm and annealed at 130°C for 30 min. Next, the substrates were brought into a vacuum evaporation chamber (base pressure of $\sim 1 \times 10^{-6}$ mbar) for thermal evaporation of the subsequent layers at a rate of 0.1-0.3 nm s⁻¹ for NPB and BePP₂, 0.01 nm s⁻¹ for PO-01, Ir(piq)₃, and CsF, and 0.5 nm s⁻¹ for aluminum. The CsF/Al contact was fabricated with a 0.13 cm² device area.

4.2.4 Characterization Methods

The photoluminescence spectra of FBtF were measured using a PTI QuantaMaster Spectrofluorometer. Transmittance spectra were obtained with a Shimadzu UV-3101PC with an integrating sphere setup. Electrical measurements for the WOLED were carried out using a homemade system consisting of a Keithley 2400 source meter and a calibrated silicon photodetector by sweeping the applied voltage from 0 to 6 V in a nitrogen-filled glovebox. EQE was calculated assuming the emission profile of the devices to be Lambertian emission, and the electroluminescence (EL) spectrum was measured using a Photoresearch SpectraScan Spectroradiometer PR-655. All characterization tests were carried out at room temperature.

4.3 Results and Discussion

4.3.1 Mechanism of the Color Conversion Layer

Figure 4.3a shows a simplified schematic of the three-color high-efficiency fluorescent/phosphorescent hybrid WOLED with the nanocomposite substrate containing the silver nanowire anode, the light scattering layer, and the color conversion layer. OLEDs generate a photon when the coulombic attraction between an electron in the LUMO and a hole at the HOMO recombine forming an exciton. Since electrons and holes are both fermions with half integer spin states; statistically, there is a 25% probability of forming a singlet state and 75% probability of forming a triplet state. The emitting layer is consisted of the hole transporting blue fluorescent material (NPB) as the matrix, locally doped with yellow phosphorescent material (PO-01) and red phosphorescent material ($\text{Ir}(\text{piq})_3$) at predefined locations to spatially allocate emission of the singlets and triplets excitons based on the respective diffusion lengths of 5.1 nm and 11.8 nm.^[134–136] **Figure 4.3b** illustrates the favorable energy transfer and triplet confinement due to the energy of the triplets from NPB (2.3 eV) to PO-01 (2.2 eV) and $\text{Ir}(\text{piq})_3$ (2.0 eV).^[108,136–138] Also, note that the triplet energy of NPB (at 2.3 eV) cannot generate green photons using phosphorescent materials since the required triplet energy would be too high.

Instead of generating green photons in the emissive layer, a fluorophore that absorbs blue light and emits green light was used in the color conversion layer. The chosen fluorophore for this study is FBtF, which has benzothiadiazole moiety as an electron-accepting heterocycle and controlled conjugation length of the polyfluorene moiety to yield electronic properties, such as bandgap, absorption coefficient, and emission quantum yield, suitable for this application (**Figure 4.4a**).^[139] FBtF has an excitation peak at 417 nm and an emission peak at 532 nm, which correlates to the absorption of the blue photons emitted from the fluorescent NPB and the

emission of green photons for improvement of the CRI (**Figure 4.4b**). Furthermore, FBtF has an excellent photoluminescence quantum yield (PLQY) of 0.98, which limits energy lost during the color conversion process and could allow the WOLED to maintain a high power efficiency.

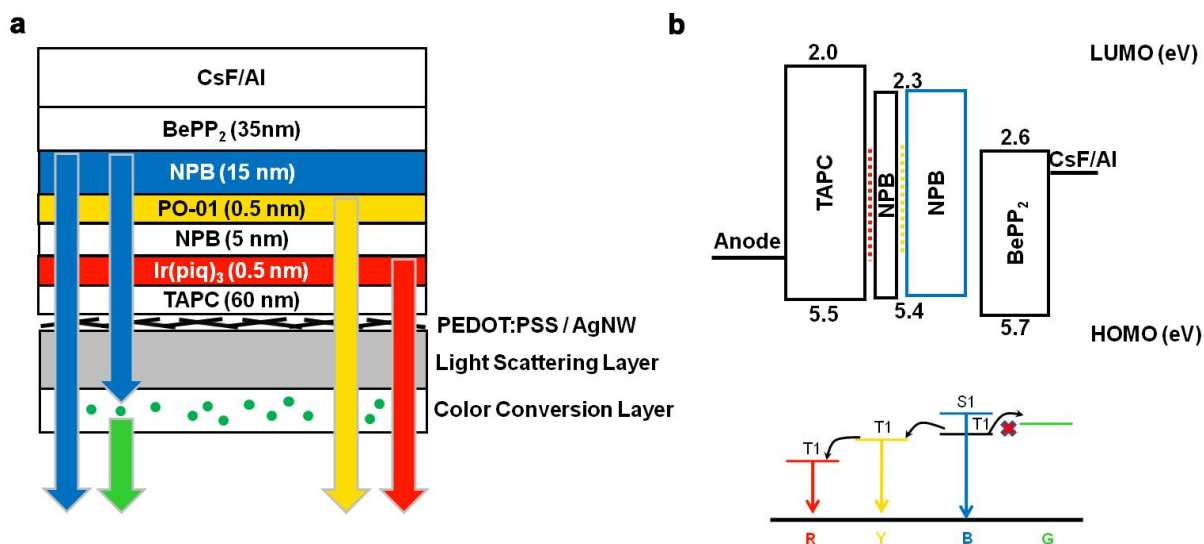


Figure 4.3. a) Schematic diagram illustrating the WOLED device structure with the color conversion layer. b) Schematic energy-level diagram of the three color-complementary hybrid WOLED device.

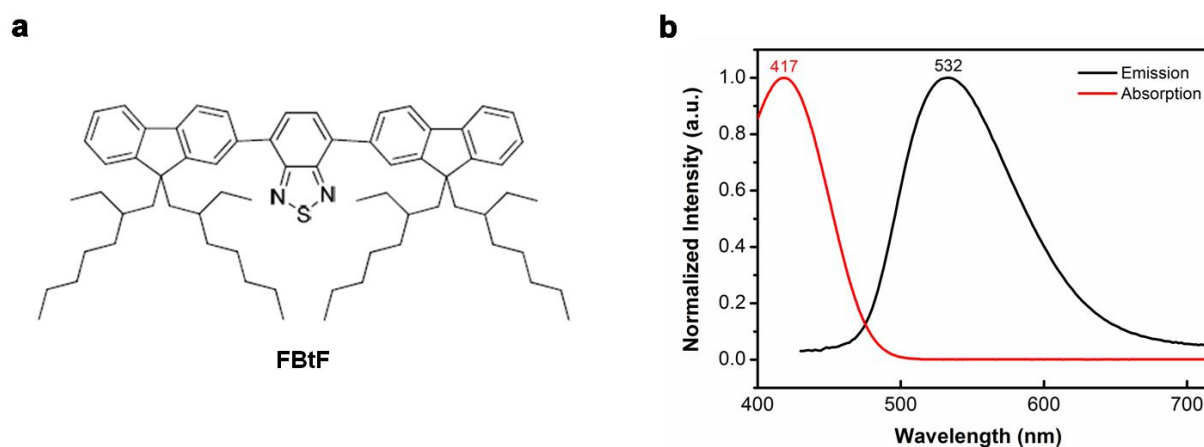


Figure 4.4. a) Molecular structures of FBtF. b) Photoluminescence spectrum of FBtF in isopropanol.

4.3.2 Fabrication Process and Characterization of Substrate

Figure 4.5 shows the spectral power distribution of an incandescent bulb (black line) with CRI of 100 and the three color fluorescent/phosphorescent hybrid WOLED fabricated on ITO/glass substrate. Based on the spectral power distribution of the hybrid WOLED on ITO/glass substrate, it is evident that the peak at around 445 nm has to be decreased and the valley at around 530 nm has to be increased, as indicated by the red and green arrows, in order to closely fit the distribution curve of the incandescent bulb for a higher CRI. When comparing to the photoluminescence spectra of the absorption and emission peaks of FBtF, the cutoff of absorption and the onset of emission coincide closely with the portions of the power distribution of the hybrid WOLED that requires tuning, allowing FBtF to be an ideal candidate to achieve efficient color conversion of the blue photons into longer wavelength photons for CRI enhancement.

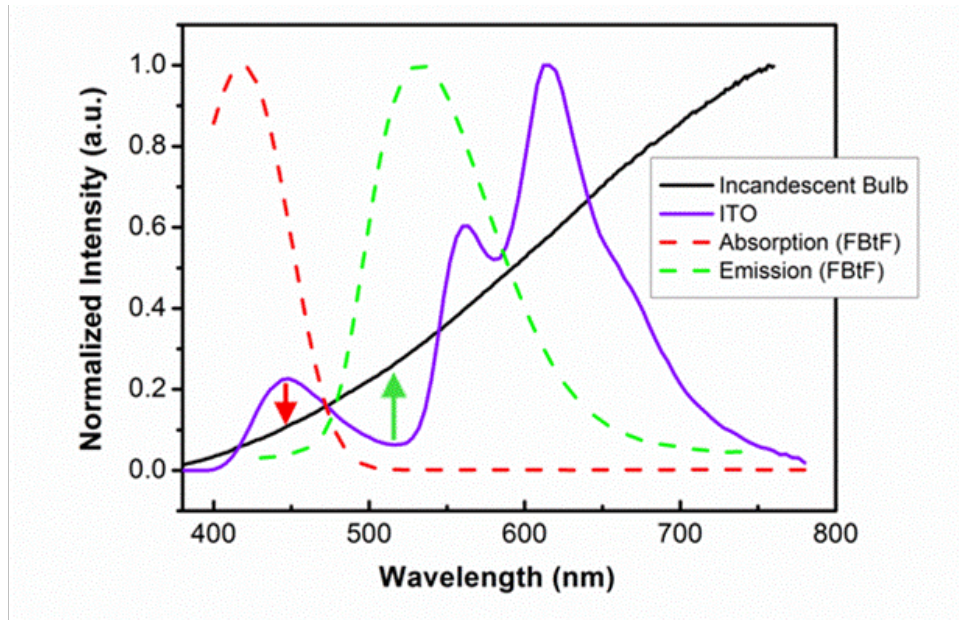


Figure 4.5. The spectral power distribution of an incandescent bulb (CRI 100) and three-color FL/Ph. hybrid WOLED fabricated on ITO/glass, and photoluminescence spectra of the absorption and emission of FBtF.

Figure 4.6 illustrates the layered structure and the fabrication process for the freestanding nanocomposite substrate. Silver nanowire nanocomposites with two different architectures were studied. Both architectures consists of silver nanowires with sheet resistance of $\sim 8 \text{ ohms sq}^{-1}$ embedded in a light scattering layer made of 3 wt% BST in SR540/SR499 polymer solution with 90 μm thickness and a color conversion layer made of 0.3 wt% FBtF in SR540/SR499 polymer solution. The sheet resistance of the AgNW networks were fabricate to match the sheet resistance of the reference control substrates (ITO/glass), and the 3wt% BST light scattering layer with 90 μm thickness was chosen based on the results in the previous chapter. The difference of the two architectures is in the thickness of the color conversion layer (AgNW + FBtF 1 with 40 μm thickness and AgNW + FBtF 2 with 90 μm thickness).

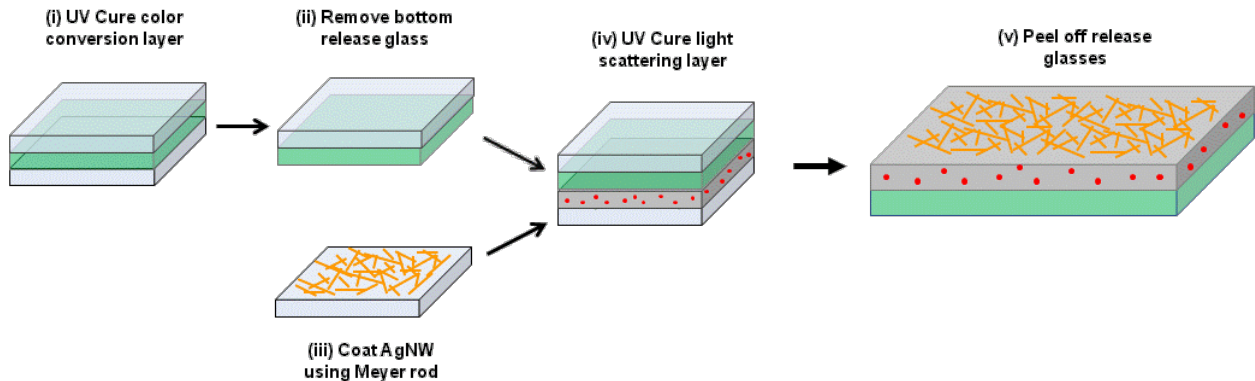


Figure 4.6. The fabrication process for a freestanding nanocomposite substrate containing silver nanowires embedded in the BST nanoparticles light scattering layer coated atop the FBtF color conversion layer.

4.3.3 Device Performance of WOLED with Color Conversion Layer

As indicated in the spectral power distribution curves of the hybrid WOLEDs fabricated on the nanocomposite substrates in **Figure 4.7a**, the FBtF color conversion layer decreases the

blue peak at ~ 445 nm and increases the green peak at ~ 530 nm, yielding a CRI of 83 for the WOLEDs fabricated on the AgNW + FBtF 1. In comparison, the CRI of the WOLEDs fabricated on ITO/glass (which is similar to the CRI of WOLEDs fabricated on AgNW nanocomposites without CCL as demonstrated in the previous chapter) is 74. Also note that when comparing between the two architectures, AgNW + FBtF 2 nanocomposite substrate significantly decreases the ratio of the blue photons but did not further increase the green peak, and the color of the resulting WOLED operating at 4 V for the AgNW + FBtF 2 appears visually yellow (**Figure 4.7b**). This indicates that further increase in color conversion would result in detrimental effect in color tuning, resulting in lowering of the CRI.

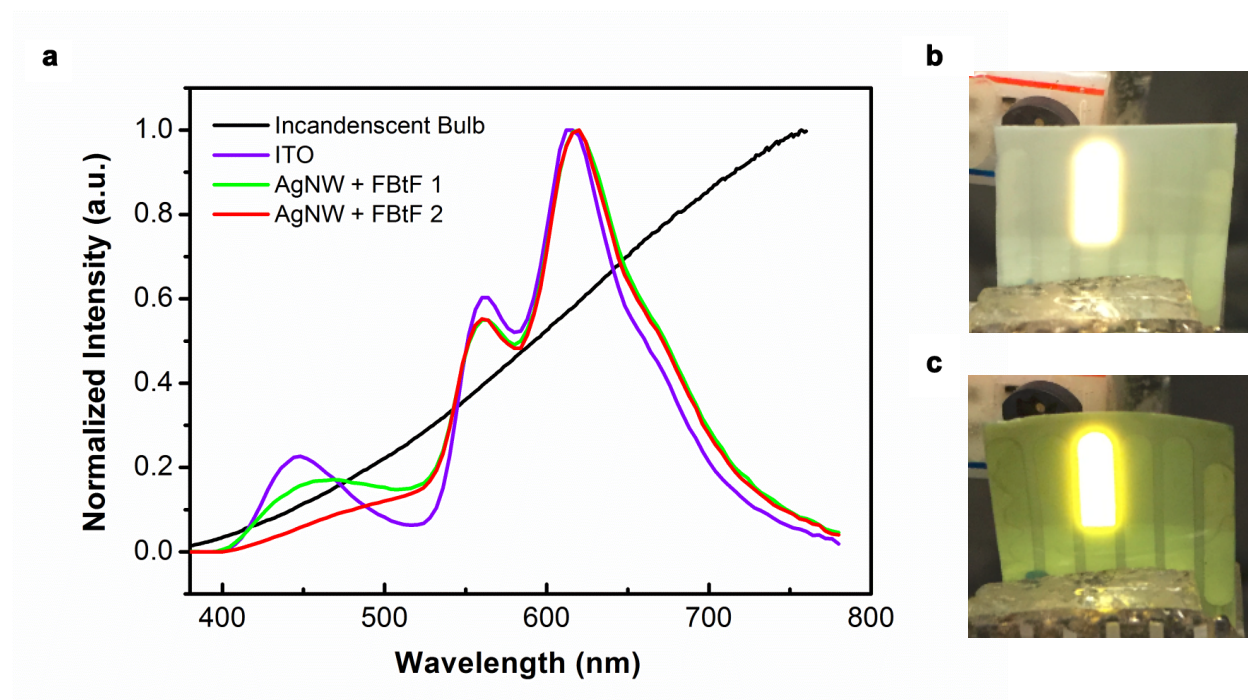


Figure 4.7. a) The spectral power distribution of an incandescent bulb (CRI 100), three color FL/Ph. hybrid WOLED fabricated on ITO/glass, AgNW + FBtF 1 and AgNW + FBtF 2 nanocomposite substrates. b) WOLED fabricated on AgNW + FBtF 1 operating at 4V. (c) WOLED fabricated on AgNW + FBtF 2 operating at 4V.

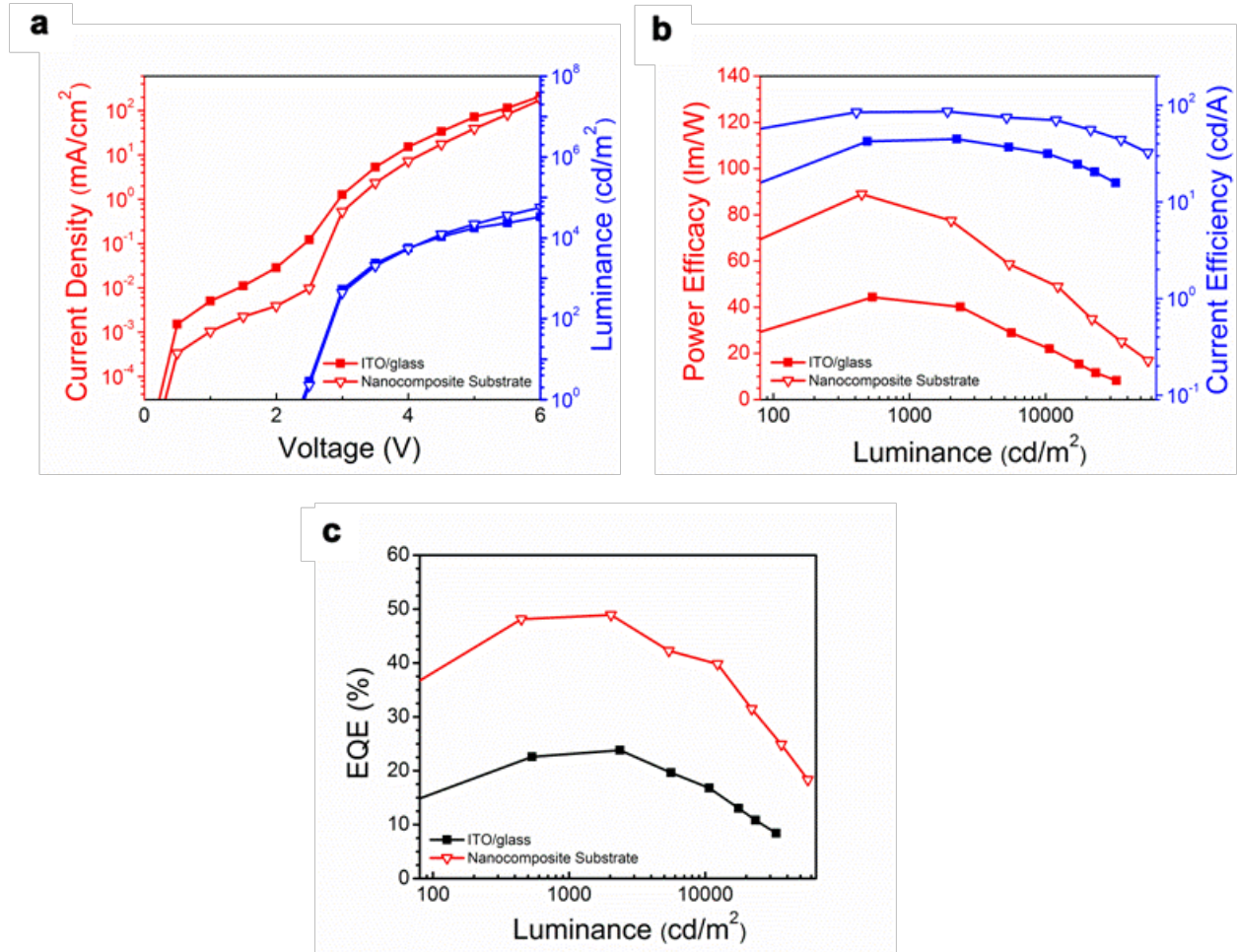


Figure 4.8. a) Comparison of performance characteristics of WOLED devices with ITO and nanocomposite anodes. a) Current-Voltage-Luminance (J-V-L) characteristics. b) Power efficacy-Luminance-Current Efficiency (PE-L-CE) characteristics. c) EQE vs Luminance. (ITO/glass and nanocomposite substrate represents WOLEDs with the device structure of substrate / anode / PEDOT / TAPC / Ir(piq)₃ / NPB / PO-01 / NPB / BePP₂ / CsF / Aluminum.)

Figure 4.8 shows the Luminance-Voltage-Current density (L-V-J) characteristics of WOLED devices fabricated on optimized nanocomposite substrates in comparison with ITO control devices. The optimized nanocomposite substrate is AgNW + FBtF 1 with parameters of

~8 ohm sq⁻¹ sheet resistance, 90 μm of light scattering layer containing 3wt% BST nanoparticles, and 40 nm of color conversion layer containing 0.3 wt% FBtF. Similarly to the silver nanowire-based devices shown in the previous chapters, WOLEDs fabricated on the nanocomposite substrates show a lower current density in comparison with ITO while the current efficiency (CE) and power efficacy (PE) show enhancement factors largely due to the elimination of the high refractive index ITO to lessen the waveguide mode and the light scattering layer to extract light from the substrate mode. Enhancement factors of nearly 1.97 for CE and 1.95 for PE, with a CE of 85.83 cd A⁻¹ and PE of 82.96 lm W⁻¹ for the nanocomposite substrate and a CE of 43.59 cd A⁻¹ and a PE of 42.59 lm W⁻¹ for the ITO/glass control at a luminance of 1000 cd m⁻² (**Figure 4.8b**) were achieved. Similarly, WOLED fabricated with the nanocomposite substrate achieved an EQE of 48.6%, corresponding to an enhancement factor of ~2.09 in comparison to the 23.3% EQE of the ITO/glass control device (**Figure 4.8c**).

4.4 Conclusion

Based on this study, a cost-effective, fully solution fabrication process of a flexible, color rendering OLED substrate with high optical performance has been developed. The transparent, conductive nanocomposite substrates, containing FBtF to down-convert blue photons generated in the NPB emissive layer to green photons, were investigated to determine its applicability to improve the coloring rendering index of the WOLEDs. These WOLEDs were fabricated using a three color-complementary hybrid structure that allows for efficient harvesting of the singlet and triplet states of the fluorophore and phosphor emitters to emit light with three spectral peaks at 445 nm (blue), 560 nm (yellow), and 615 nm (red). The CRI of the color-converted WOLEDs using 0.3 wt% of FBtF increased from 74 (ITO on glass references) to 83 while maintaining

performance metrics of 85.83 cd A⁻¹ CE, 82.96 lm W⁻¹ PE, and 48.6% EQE. This nanocomposite substrate has been shown to exhibit a light outcoupling enhancement factor of ~2 in comparison to ITO on glass references while simultaneously tuned to emit yield a warm white emission with CRI >80.

Chapter 5

Summary and Outlook

5.1 Concluding Remarks

The development of integrated strategies for low-cost approaches to fabricate flexible AgNW composites to achieve higher performance in light outcoupling and color quality are important steps in the development of next-generation OLEDs. The previous chapters in this dissertation have detailed the work done in the process development of AgNW electrodes and integrated composites for lighting applications. In addition to their marketable value, the AgNW composites fabricated using these new processing methods have achieved unprecedented performances through the synergetic effects of the materials and substrate architectures and have further highlighted the versatility of AgNW electrodes that are embedded in different polymer systems.

In Chapter 2, the development of silver nanowire paste for screen printing was first presented as a technique to pattern electrodes for flexible thin film transistors and flexible highly

transparent conductive electrodes. Prior to this publication, no fully solution processed method existed for patterning AgNWs down to a resolution of 50 μm . As of the writing of this dissertation, the most conductivity stretchable electrodes that can withstand up to 70% strain are fabricated with the screen printed AgNW electrodes reported in this work, achieving up to 46.7 kS cm^{-1} initial conductivity and 10.1 kS cm^{-1} conductivity at 70% strain.^[140] After 1000 cycles of deformation at 30% strain, the peak of resistance change (resistance value at 30% strain) of the AgNW/PUA composites with line width of 50, 100, 150, 200 and 250 μm increased gradually from approximately 7.1 to 28.2, 5.3 to 15.2, 4.5 to 13.8, 4.4 to 10.7, and 3.5 to 6.8 times its initial value, respectively.

Furthermore, the application potential of the screen-printed AgNW/PUA composites was demonstrated through the fabrication of fully solution-processed, stretchable/flexible TFTs and highly transparent TCEs. The 10 x 6 array of TFTs with a channel length of 50 μm and channel width of 1000 μm using semiconducting SWCNT achieved an average mobility of $33.8 \pm 3.7 \text{ cm}^2 \text{ V}^{-1} \text{ S}^{-1}$, with only a 10% variation which depicts good uniformity of the channel length and width from the printing process. OLEDs fabricated with the screen-printed AgNW TCEs with an average sheet resistance of 4.8 ohm sq^{-1} at 88-89% transmittance were demonstrated to show an enhancement factor of $\sim 1.6 \text{ X}$ in efficiency when compared OLEDs fabricated on the commercial, rigid ITO/glass substrates. The low solid content of 6.6 wt% of AgNWs and the minimalistic equipment requirement in this method present a promising approach to realize low-cost stretchable/wearable electrodes through a fully solution-based printing process.

Chapter 3 presents an integrated substrate that utilizes the combined synergetic effects of conductor, light scattering, and index matching while adopting a fiscally feasible fabrication approach that can be translated to high volume production at low cost. AgNWs were embedded

in a high refractive index polyamide-imide ($n \sim 1.7$) with thickness controlled to maximize the microcavity tuning effect. The AgNW electrode induces light scattering and reduces the refractive index match between the anode and substrate in comparison with ITO electrodes, which contributes to the extraction of the internal waveguide mode. Below the high refractive index polymer layer, a methacrylate-based polymer layer ($n \sim 1.53$) containing high refractive index barium strontium ($n \sim 2.6$) with an optimized concentration that can achieve extraction enhancement comparable to half sphere microlens was implemented to extract light in the substrate mode. The combined effects resulted in WOLED devices that yielded a current efficiency of 126.7 cd A^{-1} , a power efficacy of 107.2 lm W^{-1} and an EQE of 48.6% at $1,000 \text{ cd m}^{-2}$ with an enhancement factor of approximately 2.76 in comparison to the WOLED device fabricated on the control ITO/glass substrates with the same OLED architecture. To the best of our knowledge, these performance matrices are the highest among flexible WOLEDs. This work has demonstrated a cost-effective, fully solution-processed fabrication method of an integrated, flexible OLED substrate with effective outcoupling enhancement and the benefits of adaptable form factors and low material and fabrication costs that can be readily adopted in roll-to-roll technologies for mass production.

Using a similar fabrication process, a flexible, color rendering OLED substrate with high optical performance was shown to down-convert blue photons generated in the NPB emissive layer to green photons by using a FBtF dye that has an excellent photoluminescence quantum yield of 0.98 in the polymer substrate as discussed in Chapter 4. The absorption and emission peaks of the FBtF dye in this study overlap closely to the areas of the spectral power distribution of the three-color fluorescent/phosphorescent hybrid WOLED that requires color tuning to closely fit the distribution curve of the incandescent bulb in order to obtain a higher color

rendering index (CRI). The WOLED fabricated on the color rendering OLED substrate achieved a current efficiency of 85.83 cd A^{-1} , power efficacy of 82.96 lm W^{-1} , an EQE of 48.6%, and a CRI of 83. In comparison, the same WOLED was fabricated on an ITO/glass control substrate, resulting in a current efficiency of 43.59 cd A^{-1} , power efficacy of 42.59 lm W^{-1} , an EQE of 23.3%, and a CRI of 74. Beside performance enhancement in efficiency and color, this work has demonstrated the ease of fabrication of a AgNW composite system with color tuning and light extraction capabilities through a one-step polymerization of the polymer precursor containing color converting dyes and light scattering nanoparticle at suitable concentrations. Instead of fabricating the anode, substrate, light extraction, and color tuning layers separately as otherwise required in traditional fabrication processes involving ITO electrodes, the cost and time required for the anode/substrate fabrication can significantly be reduced.

5.2 Future Outlook

The development of high-performing, mechanically compliant TCEs will propel the development of flexible, stretchable OLEDs in the upcoming years. As demonstrated in this dissertation, AgNW-polymer composites can be tailored to achieve significant performance enhancement in OLED applications through appropriate material and structural designs using low-cost, solution-processed fabrication methods. Besides the core technology development of the next generation TCEs, developments in large-scale manufacturing, substantial barrier substrates for encapsulation against oxygen and moisture, and OLED device structure for improved lifetime and efficiency are all vital aspects for the advancement for OLED lighting. As research and development in all these aspects are continuously making progress, bright and brilliant innovations in lighting emitting devices will light up homes in unprecedented ways.

Though significant strides have been made in the patterned AgNW electrodes using the developed AgNW paste for screen printing, further improvements can still be made. The wash step required to remove the cellulose and the propylene glycol in the post-treatment process is time-consuming and impractical for mass production in roll to roll processes and can be eliminated by using the organic binders consists of polymer nanowires to provide rheological properties while still permitting the transfer of the nanowires through the infiltration of the matrix polymer precursors through the pores.^[141] The organic binders could also be replaced with conductive polymer gels such as the one recently published by Wang et al. to enhance the conductivity of the electrode.^[2] Furthermore, materials such as graphene oxides as demonstrated by Liang et al. and nitrile butadiene rubber as demonstrated by Ma et al. are noteworthy options to strengthen the nanowire-nanowire junctions which can enhance the overall stretchability of the electrodes.^[8,67]

Future development of materials and device structures in flexible, stretchable TCEs has the potential to realize cost-efficient, high-performing devices, especially in the advancement of OLED lighting. Light extraction can be further improved by implementing a polymer with higher refractive index than the PAI to minimize internal light refraction from the organic to the substrate. High index polyimides with refractive index exceeding 1.70 have been developed but require high-temperature annealing for the imidization of the films.^[142,143] A thin layer of metal oxide could be coated on the AgNW surface using ALD deposition of ZnO or sol-gel TiO₂ coating to enhance the thermal stability of the nanowires to withstand the imidization process.^[8,20] Alternatively, high index nanoparticles can be added to the high index polymer layer to increase its overall refractive index and to induce light scattering for enhanced

outcoupling from this layer. Another aspect of the polymer substrate that warrants attention is the barrier capability to diffusion of oxygen and moisture.

Though the work in this dissertation primarily focuses on the integration of AgNW electrodes with polymer substrates using materials or structures to enhance the performance of OLEDs, future continuation of this work can far extend towards next-generation electronics. Beyond OLED lighting, flexible, stretchable electronics are projected to have significant impacts in medicine, military, and consumer electronics. The integrated strategies in fabrication demonstrated in the previous few chapters provide insights into methods of implementing AgNW electrodes to develop complex integrated systems with unique functionalities tailored to maximize the performance of the devices. Similar strategies could be used to adopt silver nanowires for the innovation of a vast number of new systems stretching towards conceptual ideas that were once only imaginable and materializing them into functional devices that goes otherworldly beyond lighting up a brighter future.

References

- [1] C. W. Tang, S. A. Vanslyke, *Appl. Phys. Lett.* 1987, 51, 913.
- [2] Y. Wang, C. Zhu, R. Pfattner, H. Yan, L. Jin, S. Chen, F. Molina-Lopez, F. Lissel, J. Liu, N. I. Rabiah, Z. Chen, J. W. Chung, C. Linder, M. F. Toney, B. Murmann, Z. Bao, *Sci. Adv.* 2017, 3, 1.
- [3] A. Kumar, C. Zhou, *ACS Nano* 2010, 4, 11.
- [4] J. Li, J. Liang, L. Li, F. Ren, W. Hu, J. Li, S. Qi, Q. Pei, *ACS Nano* 2014, 8, 12874.
- [5] J. Liang, L. Li, X. Niu, Z. Yu, Q. Pei, *Nat. Photonics* 2013, 7, 817.
- [6] Z. Yu, Q. Zhang, L. Li, Q. Chen, X. Niu, J. Liu, Q. Pei, *Adv. Mater.* 2011, 23, 664.
- [7] J. Liang, K. Tong, Q. Pei, *Adv. Mater.* 2016, 28, 5986.
- [8] J. Liang, L. Li, K. Tong, Z. Ren, W. Hu, X. Niu, Y. Chen, Q. Pei, *ACS Nano* 2014, 8, 1590.
- [9] S. Liu, J. Li, X. Shi, E. Gao, Z. Xu, H. Tang, K. Tong, Q. Pei, J. Liang, Y. Chen, *Adv. Electron. Mater.* 2017, 3, 1.
- [10] S. Yun, X. Niu, Z. Yu, W. Hu, P. Brochu, Q. Pei, *Adv. Mater.* 2012, 24, 1321.
- [11] W. Hu, X. Niu, R. Zhao, Q. Pei, *Appl. Phys. Lett.* 2013, 102, DOI 10.1063/1.4794143.
- [12] C. Coburn, C. Jeong, S. R. Forrest, *ACS Photonics* 2017, 5.

- [13] W. Youn, J. Lee, M. Xu, R. Singh, F. So, *ACS Appl. Mater. Interfaces* 2015, 7, 8974.
- [14] B. W. D'Andrade, S. R. Forrest, *Adv. Mater.* 2004, 16, 1585.
- [15] C. Adachi, M. A. Baldo, M. E. Thompson, S. R. Forrest, *J. Appl. Phys.* 2001, 90, 5048.
- [16] S. O. Jeon, K. S. Yook, C. W. Joo, J. Y. Lee, K. Y. Ko, J. Y. Park, Y. G. Baek, *Appl. Phys. Lett.* 2008, 93, 63306.
- [17] Y. Sun, S. R. Forrest, *Nat. Photonics* 2008, 2, 483.
- [18] F. Zhao, Y. Wei, H. Xu, D. Chen, T. Ahamad, S. Alshehri, Q. Pei, D. Ma, *Mater. Horiz.* 2017, 4, 641.
- [19] M. L. Chen, A. C. Wei, H. P. D. Shieh, *Japanese J. Appl. Physics, Part 1 Regul. Pap. Short Notes Rev. Pap.* 2007, 46, 1521.
- [20] T. W. Koh, J. A. Spechler, K. M. Lee, C. B. Arnold, B. P. Rand, *ACS Photonics* 2015, 2, 1366.
- [21] V. Gohri, S. Hofmann, S. Reineke, T. Rosenow, M. Thomschke, M. Levichkova, B. Lüssem, K. Leo, *Org. Electron. physics, Mater. Appl.* 2011, 12, 2126.
- [22] R. Bathelt, D. Buchhauser, C. Gärditz, R. Paetzold, P. Wellmann, *Org. Electron. physics, Mater. Appl.* 2007, 8, 293.
- [23] S. Möller, S. R. Forrest, *J. Appl. Phys.* 2002, 91, 3324.
- [24] W. Gaynor, S. Hofmann, M. G. Christoforo, C. Sachse, S. Mehra, A. Salleo, M. D. McGehee, M. C. Gather, B. Lüssem, L. Müller-Meskamp, P. Peumans, K. Leo, *Adv. Mater.* 2013, 25, 4006.
- [25] L. Hu, H. S. Kim, J. Lee, P. Peumans, Y. Cui, *ACS Nano* 2010, 4, 2955.
- [26] L. Li, J. Liang, S.-Y. Chou, X. Zhu, X. Niu, ZhibinYu, Q. Pei, *Sci. Rep.* 2014, 4, 4307.
- [27] L. Li, Z. Yu, C. Chang, W. Hu, X. Niu, Q. Chen, Q. Pei, *Phys. Chem. Chem. Phys.* 2012,

- 14, 14249.
- [28] Z. Yu, L. Hu, Z. Liu, M. Sun, M. Wang, G. Grüner, Q. Pei, *Appl. Phys. Lett.* 2009, 95, DOI 10.1063/1.3266869.
- [29] G. Gu, Z. Shen, P. E. Burrows, S. R. Forrest, *Adv. Mater.* 1997, 9, 725.
- [30] J. Liang, L. Li, X. Niu, Z. Yu, Q. Pei, *J. Phys. Chem. C* 2013, 117, 16632.
- [31] J. Liang, L. Li, D. Chen, T. Hajagos, Z. Ren, S. Y. Chou, W. Hu, Q. Pei, *Nat. Commun.* 2015, 6, 7647.
- [32] C. J. M. Emmott, A. Urbina, J. Nelson, *Sol. Energy Mater. Sol. Cells* 2012, 97, 14.
- [33] X. Cao, H. Chen, X. Gu, B. Liu, W. Wang, Y. Cao, F. Wu, C. Zhou, *ACS Nano* 2014, 8, 12769.
- [34] P. Chen, Y. Fu, R. Aminirad, C. Wang, J. Zhang, K. Wang, K. Galatsis, C. Zhou, *Nano Lett.* 2011, 11, 5301.
- [35] P. H. Lau, K. Takei, C. Wang, Y. Ju, J. Kim, Z. Yu, T. Takahashi, G. Cho, A. Javey, *Nano Lett.* 2013, 13, 3864.
- [36] K. Fukuda, Y. Takeda, Y. Yoshimura, R. Shiwaku, L. T. Tran, T. Sekine, M. Mizukami, D. Kumaki, S. Tokito, *Nat. Commun.* 2014, 5, 4147.
- [37] M. Singh, H. M. Haverinen, P. Dhagat, G. E. Jabbour, *Adv. Mater.* 2010, 22, 673.
- [38] P. Andersson, R. Forchheimer, P. Tehrani, M. Berggren, *Adv. Funct. Mater.* 2007, 17, 3074.
- [39] F. Torrisi, T. Hasan, W. Wu, Z. Sun, A. Lombardo, T. S. Kulmala, G. W. Hsieh, S. Jung, F. Bonaccorso, P. J. Paul, D. Chu, A. C. Ferrari, *ACS Nano* 2012, 6, 2992.
- [40] H. Minemawari, T. Yamada, H. Matsui, J. Y. Tsutsumi, S. Haas, R. Chiba, R. Kumai, T. Hasegawa, *Nature* 2011, 475, 364.

- [41] J. Birnstock, J. Blässing, A. Hunze, M. Scheffel, M. Stöbel, K. Heuser, G. Wittmann, J. Wörle, A. Winnacker, *Appl. Phys. Lett.* 2001, 78, 3905.
- [42] W. J. Hyun, E. B. Secor, M. C. Hersam, C. D. Frisbie, L. F. Francis, *Adv. Mater.* 2015, 27, 109.
- [43] D. A. Pardo, G. E. Jabbour, N. Peyghambarian, *Adv. Mater.* 2000, 12, 1249.
- [44] W. J. Lee, W. T. Park, S. Park, S. Sung, Y. Y. Noh, M. H. Yoon, *Adv. Mater.* 2015, 27, 5043.
- [45] B. Y. Ahn, E. B. Duoss, M. J. Motala, X. Guo, S. Il Park, Y. Xiong, J. Yoon, R. G. Nuzzo, J. A. Rogers, J. A. Lewis, *Science (80-.)*. 2009, 323, 1590.
- [46] T. Sekitani, H. Nakajima, H. Maeda, T. Fukushima, T. Aida, K. Hata, T. Someya, *Nat. Mater.* 2009, 8, 494.
- [47] T. Araki, M. Nogi, K. Suganuma, M. Kogure, O. Kirihara, *IEEE Electron Device Lett.* 2011, 32, 1424.
- [48] K. Y. Chun, Y. Oh, J. Rho, J. H. Ahn, Y. J. Kim, H. R. Choi, S. Baik, *Nat. Nanotechnol.* 2010, 5, 853.
- [49] M. Park, J. Im, M. Shin, Y. Min, J. Park, H. Cho, S. Park, M. B. Shim, S. Jeon, D. Y. Chung, J. Bae, J. Park, U. Jeong, K. Kim, *Nat. Nanotechnol.* 2012, 7, 803.
- [50] N. Matsuhisa, M. Kaltenbrunner, T. Yokota, H. Jinno, K. Kuribara, T. Sekitani, T. Someya, *Nat. Commun.* 2015, 6, 7461.
- [51] S. De, T. M. Higgins, P. E. Lyons, E. M. Doherty, P. N. Nirmalraj, W. J. Blau, J. J. Boland, J. N. Coleman, *ACS Nano* 2009, 3, 1767.
- [52] J. Y. Lee, S. T. Connor, Y. Cui, P. Peumans, *Nano Lett.* 2008, 8, 689.
- [53] P. Lee, J. Lee, H. Lee, J. Yeo, S. Hong, K. H. Nam, D. Lee, S. S. Lee, S. H. Ko, *Adv.*

- Mater. 2012, 24, 3326.
- [54] Y. Sun, B. Gates, B. Mayers, Y. Xia, Nano Lett. 2002, 2, 165.
- [55] J. Lee, I. Lee, T. S. Kim, J. Y. Lee, Small 2013, 9, 2887.
- [56] F. C. Krebs, M. Jørgensen, K. Norrman, O. Hagemann, J. Alstrup, T. D. Nielsen, J. Fyenbo, K. Larsen, J. Kristensen, Sol. Energy Mater. Sol. Cells 2009, 93, 422.
- [57] R. Faddoul, N. Reverdy-Bruas, A. Blayo, Mater. Sci. Eng. B Solid-State Mater. Adv. Technol. 2012, 177, 1053.
- [58] K. Park, D. Seo, J. Lee, Colloids Surfaces A Physicochem. Eng. Asp. 2008, 313, 351.
- [59] R. Faddoul, N. Reverdy-Bruas, J. Bourel, J. Mater. Sci. Mater. Electron. 2012, 23, 1415.
- [60] S. Wu, J. Mater. Sci. Mater. Electron. 2007, 18, 447.
- [61] S. Merilampi, T. Laine-Ma, P. Ruuskanen, Microelectron. Reliab. 2009, 49, 782.
- [62] W. Yin, D. H. Lee, J. Choi, C. Park, S. M. Cho, Korean J. Chem. Eng. 2008, 25, 1358.
- [63] S. Hemmati, D. P. Barkey, N. Gupta, R. Banfield, ECS J. Solid State Sci. Technol. 2015, 4, 3075.
- [64] R. Rudež, J. Pavlič, S. Bernik, J. Eur. Ceram. Soc. 2015, 35, 3013.
- [65] R. Durairaj, S. Ramesh, S. Mallik, A. Seman, N. Ekere, Mater. Des. 2009, 30, 3812.
- [66] R. Durairaj, S. Mallik, A. Seman, A. Marks, N. N. Ekere, J. Mater. Process. Technol. 2009, 209, 3923.
- [67] R. Ma, J. Lee, D. Choi, H. Moon, S. Baik, Nano Lett. 2014, 14, 1944.
- [68] Y. Kim, J. Zhu, B. Yeom, M. Di Prima, X. Su, J. G. Kim, S. J. Yoo, C. Uher, N. A. Kotov, Nature 2013, 500, 59.
- [69] C. Wang, J. Zhang, K. Ryu, A. Badmaev, L. G. De Arco, C. Zhou, Nano Lett. 2009, 9, 4285.

- [70] S. Park, M. Vosguerichian, Z. Bao, *Nanoscale* 2013, 5, 1727.
- [71] J. Shi, C. X. Guo, M. B. Chan-Park, C. M. Li, *Adv. Mater.* 2012, 24, 358.
- [72] J. Woerle, H. Rost, *MRS Bull.* 2011, 36, 789.
- [73] Y. Galagan, J. E. J.m. Rubingh, R. Andriessen, C. C. Fan, P. W.m. Blom, S. C. Veenstra, J. M. Kroon, *Sol. Energy Mater. Sol. Cells* 2011, 95, 1339.
- [74] D. Erath, A. Filipović, M. Retzlaff, A. K. Goetz, F. Clement, D. Biro, R. Preu, *Sol. Energy Mater. Sol. Cells* 2010, 94, 57.
- [75] Y. Tao, Q. Wang, C. Yang, Q. Wang, Z. Zhang, T. Zou, J. Qin, D. Ma, *Angew. Chemie - Int. Ed.* 2008, 47, 8104.
- [76] N. C. Giebink, B. W. D'Andrade, M. S. Weaver, P. B. MacKenzie, J. J. Brown, M. E. Thompson, S. R. Forrest, *J. Appl. Phys.* 2008, 103, 44509.
- [77] K. T. Wong, Y. Y. Chien, R. T. Chen, C. F. Wang, Y. T. Lin, H. H. Chiang, P. Y. Hsieh, C. C. Wu, C. H. Chou, Y. O. Su, G. H. Lee, S. M. Peng, *J. Am. Chem. Soc.* 2002, 124, 11576.
- [78] M. Kim, S. K. Jeon, S. H. Hwang, J. Y. Lee, *Adv. Mater.* 2015, 27, 2515.
- [79] S. L. Tao, Z. K. Peng, X. H. Zhang, P. F. Wang, C.-S. Lee, S.-T. Lee, *Adv. Funct. Mater.* 2005, 15, 1716.
- [80] H. Y. Oh, C. Lee, S. Lee, *Org. Electron. physics, Mater. Appl.* 2009, 10, 163.
- [81] S. J. Su, E. Gonmori, H. Sasabe, J. Kido, *Adv. Mater.* 2008, 20, 4189.
- [82] T. D. Schmidt, D. S. Setz, M. Flämmich, J. Frischeisen, D. Michaelis, B. C. Krummacher, N. Danz, W. Brütting, *Appl. Phys. Lett.* 2011, 99, 163302.
- [83] S. Y. Kim, W. I. Jeong, C. Mayr, Y. S. Park, K. H. Kim, J. H. Lee, C. K. Moon, W. Brütting, J. J. Kim, *Adv. Funct. Mater.* 2013, 23, 3896.

- [84] H. Sasabe, N. Toyota, H. Nakanishi, T. Ishizaka, Y. J. Pu, J. Kido, *Adv. Mater.* 2012, 24, 3212.
- [85] H. Sasabe, J. Kido, *J. Mater. Chem. C* 2013, 1, 1699.
- [86] Y. Kawamura, K. Goushi, J. Brooks, J. J. Brown, H. Sasabe, C. Adachi, *Appl. Phys. Lett.* 2005, 86, 71104.
- [87] C. F. Madigan, M.-H. Lu, J. C. Sturm), *Appl. Phys. Lett.* 2000, 76, 1650.
- [88] M.-K. Wei, I.-L. Su, *Opt. Express* 2004, 12, 5777.
- [89] E. Kim, H. Cho, K. Kim, T. W. Koh, J. Chung, J. Lee, Y. K. Park, S. Yoo, *Adv. Mater.* 2015, 27, 1624.
- [90] T. Yamasaki, K. Sumioka, T. Tsutsui, *Appl. Phys. Lett.* 2000, 76, 1243.
- [91] H.-W. Chang, J. Lee, S. Hofmann, Y. H. Kim, L. Müller-Meskamp, B. Lüssem, C.-C. Wu, K. Leo, M. C. Gather, *J. Appl. Phys.* 2013, 113, 204502.
- [92] Y. J. Lee, S. H. Kim, J. Huh, G. H. Kim, Y. H. Lee, S. H. Cho, Y. C. Kim, Y. R. Do, *Appl. Phys. Lett.* 2003, 82, 3779.
- [93] K. Ishihara, M. Fujita, I. Matsubara, T. Asano, S. Noda, H. Ohata, A. Hirasawa, H. Nakada, N. Shimoji, *Appl. Phys. Lett.* 2007, 90, 111114.
- [94] Y. R. Do, Y. C. Kim, Y.-W. Song, C.-O. Cho, H. Jeon, Y.-J. Lee, S.-H. Kim, Y.-H. Lee, *Adv. Mater.* 2003, 15, 1214.
- [95] S. Reineke, F. Lindner, G. Schwartz, N. Seidler, K. Walzer, B. Lüssem, K. Leo, *Nature* 2009, 459, 234.
- [96] S. Mladenovski, K. Neyts, D. Pavicic, A. Werner, C. Rothe, *Opt. Express* 2009, 17, 7562.
- [97] A. Mikami, T. Koyanagi, *Sid* 2009, 60, 907.
- [98] A. Mikami, *Phys. Status Solidi* 2011, 8, 2899.

- [99] Z. B. Wang, M. G. Helander, J. Qiu, D. P. Puzzo, M. T. Greiner, Z. M. Hudson, S. Wang, Z. W. Liu, Z. H. Lu, *Nat. Photonics* 2011, 5, 753.
- [100] D. Chen, J. Liang, C. Liu, G. Saldanha, F. Zhao, K. Tong, J. Liu, Q. Pei, *Adv. Funct. Mater.* 2015, 25, 7512.
- [101] J. Lee, P. Lee, H. Lee, D. Lee, S. S. Lee, S. H. Ko, *Nanoscale* 2012, 4, 6408.
- [102] G. Kavei, A. M. Gheidari, *J. Mater. Process. Technol.* 2008, 208, 514.
- [103] D. Raoufi, A. Kiasatpour, H. R. Fallah, A. S. H. Rozatian, *Appl. Surf. Sci.* 2007, 253, 9085.
- [104] Y. Sun, N. C. Giebink, H. Kanno, B. Ma, M. E. Thompson, S. R. Forrest, *Nature* 2006, 440, 908.
- [105] V. Adamovich, J. Brooks, A. Tamayo, A. M. Alexander, P. I. Djurovich, B. W. D'Andrade, C. Adachi, S. R. Forrest, M. E. Thompson, *New J. Chem.* 2002, 26, 1171.
- [106] B. W. D'Andrade, R. J. Holmes, S. R. Forrest, *Adv. Mater.* 2004, 16, 624.
- [107] S. Tokito, T. Iijima, T. Tsuzuki, F. Sato, *Appl. Phys. Lett.* 2003, 83, 2459.
- [108] D. Zhang, M. Cai, Y. Zhang, D. Zhang, L. Duan, *ACS Appl. Mater. Interfaces* 2015, 7, 28693.
- [109] S. Liu, S. Ho, F. So, *ACS Appl. Mater. Interfaces* 2016, 8, 9268.
- [110] K. Saxena, V. K. Jain, D. S. Mehta, *Opt. Mater. (Amst.)* 2009, 32, 221.
- [111] J. J. Shiang, A. R. Duggal, *J. Appl. Phys.* 2004, 95, 2880.
- [112] T. Tsutsui, M. Yahiro, H. Yokogawa, K. Kawano, M. Yokoyama, *Adv. Mater* 2001, 1149.
- [113] H. Benisty, R. Stanley, M. Mayer, *J. Opt. Soc. Am. A* 1998, 15, 1192.
- [114] M. Furno, R. Meerheim, S. Hofmann, B. Lüssem, K. Leo, *Phys. Rev. B - Condens. Matter Mater. Phys.* 2012, 85, 115205.

- [115] S. Tokito, T. Tsutsui, Y. Taga, *J. Appl. Phys.* 1999, 86, 2407.
- [116] C. H. Chang, Y. J. Lu, C. C. Liu, Y. H. Yeh, C. C. Wu, *IEEE/OSA J. Disp. Technol.* 2007, 3, 193.
- [117] C. H. Chang, K. C. Tien, C. C. Chen, M. S. Lin, H. C. Cheng, S. H. Liu, C. C. Wu, J. Y. Hung, Y. C. Chiu, Y. Chi, *Org. Electron. physics, Mater. Appl.* 2010, 11, 412.
- [118] B. W. . D'Andrade, M. E. . Thompson, S. R. Forrest, *Adv. Mater.* 2002, 147.
- [119] G. Schwartz, M. Pfeiffer, S. Reineke, K. Walzer, K. Leo, *Adv. Mater.* 2007, 19, 3672.
- [120] S. H. Eom, Y. Zheng, E. Wrzesniewski, J. Lee, N. Chopra, F. So, J. Xue, *Appl. Phys. Lett.* 2009, 94, DOI 10.1063/1.3120276.
- [121] J. Kalinowski, M. Cocchi, D. Virgili, V. Fattori, J. A. G. Williams, *Adv. Mater.* 2007, 19, 4000.
- [122] H. Yang, Y. Shi, Y. Zhao, Y. Meng, W. Hu, J. Hou, S. Liu, *Displays* 2008, 29, 327.
- [123] G. Zhou, Q. Wang, C.-L. Ho, W.-Y. Wong, D. Ma, L. Wang, *Chem. Commun.* 2009, 2, 3574.
- [124] J. H. Jou, S. M. Shen, C. R. Lin, Y. S. Wang, Y. C. Chou, S. Z. Chen, Y. C. Jou, *Org. Electron. physics, Mater. Appl.* 2011, 12, 865.
- [125] H. Kanno, N. C. Giebink, Y. Sun, S. R. Forrest, *Appl. Phys. Lett.* 2006, 89, 2004.
- [126] G. Schwartz, S. Reineke, K. Walzer, K. Leo, *Appl. Phys. Lett.* 2008, 92, 2006.
- [127] J.-H. Jou, Y.-C. Chou, S.-M. Shen, M.-H. Wu, P.-S. Wu, C.-R. Lin, R.-Z. Wu, S.-H. Chen, M.-K. Wei, C.-W. Wang, *J. Mater. Chem.* 2011, 21, 18523.
- [128] X. Zhuang, H. Zhang, K. Ye, Y. Liu, Y. Wang, *ACS Appl. Mater. Interfaces* 2016, 8, 11221.
- [129] A. R. Duggal, J. J. Shiang, C. M. Heller, D. F. Foust, *Appl. Phys. Lett.* 2002, 80, 3470.

- [130] J. Lee, N. Chopra, D. Bera, S. Maslov, S. H. Eom, Y. Zheng, P. Holloway, J. Xue, F. So, *Adv. Energy Mater.* 2011, 1, 174.
- [131] K. Tong, X. Liu, F. Zhao, D. Chen, Q. Pei, *Adv. Opt. Mater.* 2017, 5, 1.
- [132] “World Record White OLED Performance Exceeds 100 lm/W,” can be found under <https://www.energy.gov/eere/ssl/world-record-white-oled-performance-exceeds-100-lmw>, n.d.
- [133] B. C. Krummacher, V.-E. Choong, M. K. Mathai, S. A. Choulis, F. So, F. Jermann, T. Fiedler, M. Zachau, *Appl. Phys. Lett.* 2006, 88, 113506.
- [134] W. A. Luhman, R. J. Holmes, *Appl. Phys. Lett.* 2009, 94, 1.
- [135] R. R. Lunt, N. C. Giebink, A. A. Belak, J. B. Benziger, S. R. Forrest, *J. Appl. Phys.* 2009, 105, DOI 10.1063/1.3079797.
- [136] F. Zhao, Y. Wei, H. Xu, D. Chen, T. Ahamad, S. Alshehri, Q. Pei, D. Ma, *Mater. Horiz.* 2017, 4, 641.
- [137] S. W. Liu, Y. Divayana, A. P. Abiyasa, S. T. Tan, H. V. Demir, X. W. Sun, *Appl. Phys. Lett.* 2012, 101, DOI 10.1063/1.4749278.
- [138] D. Zhang, L. Duan, Y. Zhang, M. Cai, D. Zhang, Y. Qiu, *Light Sci. Appl.* 2015, 4, e232.
- [139] Q. Chen, Thesis, Univ. California, Los Angeles 2012.
- [140] N. Matsuhisa, D. Inoue, P. Zalar, H. Jin, Y. Matsuba, A. Itoh, T. Yokota, D. Hashizume, T. Someya, *Nat. Mater.* 2017, 16, 834.
- [141] T. Saito, S. Kimura, Y. Nishiyama, A. Isogai, *Biomacromolecules* 2007, 8, 2485.
- [142] C. L. Tsai, H. J. Yen, G. S. Liou, *React. Funct. Polym.* 2016, 108, 2.
- [143] J. Liu, M. Ueda, *J. Mater. Chem.* 2009, 19, 8907.